博士学位論文

Bearing Fault Diagnosis Method by Multilevel Spectral Segmentation Theory and Signal Fusion

（マルチレベルスペクトルセグメンテーション理論と信号融合による軸受故障診断法）

三重大学大学院 生物資源学研究科

共生環境学専攻 環境・生産科学講座

環境情報システム工学教育研究分野

張 坤

Abstract

Effectively identifying the health status of rolling bearings can reduce the maintenance costs of rotating mechanical components. With the development and improvement of various signal processing theories, the mode of extracting fault information from the frequency domain has gradually replaced the mode from the time domain. In this paper, by optimizing the single-level spectral segmentation methods such as analytical mode decomposition, frequency slice wavelet transform, empirical wavelet transform, and quaternion, the corresponding multi-level spectral segmentation method and variable tower boundary distribution diagram and feature screening index are designed. The detailed research content is as follows:

(1) An adaptive Ailinggram that uses variable spectral segmentation framework to optimize analytical mode decomposition to automatically decompose the mode information in rotating machinery signals was proposed. The framework relies on the variability of the window width and envelope estimation characteristics of order statistics filter to increase the diversity of the center frequencies and bandwidth. A novel harmonic correlation index is designed to identify the characteristics of rotating machinery faults from various levels of results, and to improve the usability in mechanical equipment fault diagnosis. The method can be applied to fault diagnosis of rotating machinery under high speed/dynamic load conditions.

(2) Fast Entrogram was proposed to segment the spectrum and accurately filtering fault information from the frequency domain. The fluctuation state of the Fourier spectrum is of key importance in distinguishing the distribution of different components in the signal at each frequency. After the Fourier transform of the spectrum is intercepted and reconstructed, the minimum points of the new sequence can separate different components in the signal. Subsequently, the frequency slice function is used to extract each frequency band to obtain better filtering effects than the finite impulse response filter. Finally, the proposed novel correlation spectral negentropy is sensitive to periodic pulses and can be used to screen the component that contains the most fault information. The simulation results show that the proposed Fast Entrogram can effectively extract periodic pulses. It is verified by experimental signals that the method can be applied to fault diagnosis of rotating machinery under low speed/heavy load conditions.

(3) The power spectral density will be calculated and used to segment the spectrum, which can reduce the number of extreme points and the dependence on them. According to the variability of the PSD window width, a tower boundaries distribution diagram (W-Autogram) and weighted unbiased autocorrelation would be used to extract specific information is proposed. Simulation signals and experimental results verify that the proposed method can be applied to the fault diagnosis of rolling bearings in rotating machinery.

(4) In order to extract the periodic pulse information in the signal and weaken the influence of the interference signal, we proposed Harmonic spectral kurtosis which can extract the harmonic information in the envelope spectrum, quantify the periodic pulses in the signal, and suppress the influence of interference such as random pulse. The simulation signal shows that the proposed method is accurate and effective. The data of bearing inner ring, outer ring and compound faults prove that the method can be applied to bearing fault diagnosis.

(5) Quaternion analytical mode decomposition (QAMD) is proposed to process multiple

acoustic signals and extract fault information in industrial machinery systems with high sampling frequency, low speed, and heavy load. QAMD can separate characteristic information from frequency domain and extend it to the fault diagnosis of rotating industrial machinery. The multi-signal fusion method based on quaternion can process multiple sets of longer digital signals at the same time, which provides a new idea for the synchronous processing of big data. The proposed quaternion Fourier trend spectral segmentation method can not only automatically obtain bisecting frequencies and divide the signal into several frequency bands, but also realize the fusion and modal decomposition of multiple sets of digital signals in frequency domain. Experimental results show that the proposed method can effectively extract useful information from acoustic signals and apply it to bearing fault diagnosis.
Keywords: analytical mode decomposition, rotating machinery, order statistics filter, harmonic correlation index, Entrogram, correlation spectral negentropy, power spectral density, weighted unbiased autocorrelation, Harmonic spectral kurtosis, Quaternion.

Acknowledgments

It has been a great honour for me to study for Doctor of Engineering in Mie University since coming to Japan.

Under the careful guidance of my supervisor, Prof. Jinyama Ho, I completed this doctoral dissertation. Prof. Jinyama Ho not only gave me patient guidance academically, but also gave me a lot of help in life, and taught me a humble and rigorous learning attitude. I would like to thank Prof. Jinyama for giving me the opportunity to study abroad. In the future, I will take the professor as an example, be strict with myself, be lenient with others, strive for perfection, and be rigorous in my studies.

COVID-19 came suddenly and brought a lot of inconvenience to my life. Thanks to Mie University and the "Honda Benjiro International Student Engineer Development Scholarship Fund" for giving me financial help and solving the difficulties in my life, which allows me to devote more energy to scientific research and experiments.

I would like to thank Prof. WANG Xiulun, Prof. FUKUSHIMA Takashi, Prof. MURAKAMI Katsusuke, and Prof. MORIO Yoshinari for their invaluable advice during the doctoral course. Moreover, I also want to thank SONG Liuyang, LIAO Zhiqiang, TANG Haihong, DUAN Tangshao, SONG Xuewei for their enthusiastic support and help in my study and life

I would like to thank my parents and Shi Ling for their support and encouragement to my study abroad. Thanks to all my friends who care and support me.

Zhang Kun
张 坤
2022.8.24

Content

Chapter 1
Introduction

1.1 Background

In recent years, industries around the world have basically achieved interconnection. Industrial globalization is inseparable from the rapid development of science and technology and the iterative upgrade of large-scale electromechanical equipment [1-2]. "Industry 4.0" and "Made in China 2025" have put forward higher requirements for information technology to promote industrial transformation [3-5]. The digitalization and intelligence of industrial production will become the main theme of the future industry. With the rapid development of science and technology around the world, large-scale electromechanical equipment not only occupies a dominant position in the industrial system, but also has a wide range of applications: transportation, medical care, industry, agriculture, national defense, etc. The use method and operating state of the equipment become more complicated [6]. The high-precision automatic control system not only ensures the automatic operation of the equipment, but also avoids the harm and threat to people in the harsh working environment. The labor cost is reduced and the production efficiency is increased [7-9]. However, when the equipment is operated under heavy load and high temperature for a long time, it is easy to damage parts and increase the failure rate. If equipment fails, timely maintenance will result in huge economic losses, and failure to maintain timely may result in casualties [10,11]. Under this premise, the development of equipment condition monitoring system and equipment fault diagnosis system has important economic significance and social value [12].

The equipment condition monitoring system in the traditional sense needs to have signal acquisition system and simple statistical index calculation system. The equipment fault diagnosis system not only has signal acquisition module, but also needs signal processing module and fault identification module [13,14]. The traditional signal processing process includes time-frequency analysis, signal decomposition, mode extraction and so on. Correctly distinguishing the interference and fault information in the signal is the difficulty and focus of signal processing. The current research objects are rich and advanced: intelligent manufacturing products represented by robotic arms [15], rail transit equipment represented by high-speed rail and locomotives [16-18], high-tech equipment represented by aero-engines[19], sustainable energy machinery represented by wind turbine, etc. [20]. As modern equipment gradually tends to be complex, overloaded, large-scale, high-speed, and high-precision, which means that traditional signal processing methods are difficult to be universal and need to be updated iteratively [21].

Bearings, as one of the most widely used important mechanical parts, are popular in the field of signal processing [22]. When industrial equipment is under high temperature, heavy load, high speed and other conditions, the bearing may work in this environment for a long time. The harsh environment will not only damage the bearing, but may also bring complex interference information [23,24]. How to locate the damaged bearing and predict the time when the bearing may be damaged requires high accuracy of the condition monitoring system and fault diagnosis system to avoid major failures of the equipment [25]. Therefore, constantly exploring new signal processing methods and applying them to fault diagnosis is the focus of scholars' attention and research. The proposal of the new method and the application of the new technology not only enrich the theoretical basis of the field of mechanical fault diagnosis, but

also promote the further development of the mechanical fault diagnosis technology.

1.2 Modern signal decomposition methods

Modern signal decomposition methods include many classical algorithms, which can be classified into time-domain/frequency-domain signal decomposition methods, and time-frequency analysis methods. Traditional signal decomposition methods generally need to manually adjust parameters and extract components, such as short-time Fourier transform, Wigner-Ville distribution, wavelet analysis, etc. [26-28]. Empirical mode decomposition (EMD) proposed by Huang N E [29] makes the adaptive signal processing method a new hot topic. The equipment status online monitoring system collects the vibration acceleration signal or acoustic signal of the vulnerable parts, which can detect the equipment abnormality in time. Since the vibration signal during the operation of mechanical equipment often presents non-stationary and nonlinear characteristics, the difficulty of extracting signal features from the time domain is easily disturbed by the environment such as noise [30,31]. This paper is devoted to the research and promotion of processing modes for extracting signals from the frequency domain, such as analytic mode decomposition, empirical wavelet transform and frequency slice wavelet transform.

Analytical mode decomposition (AMD) extracts component from the Fourier spectrum by searching for useful modes [32]. It is characterized by manual selection of frequencies to be separated and filtering out high-frequency noise or low-frequency interference. This method does not require finding outliers in the time domain waveform or calculating the mean value, and can avoid interference from extreme points in the waveform. Compared with empirical mode decomposition, AMD can suppress mode aliasing and end-point effects [33,34]. AMD's application first appeared in the field of construction. Wang [35] used AMD to reconstruct the components of the Synchrosqueezing wavelet transform to attenuate the influence of wavelet function parameters. The Multiple AMD proposed by Qu [36] utilizes the free vibration response and nonlinear oscillator, and defines the besecting frequency with reference to velocity and displacement, which can identify stiffness and damping coefficients. Wu [37] created a time-frequency domain digital scintillation meter using AMD and applied it to wind farms. When collecting vibration signals from electrical or mechanical equipment in operation, a large amount of unpredictable information is generated, and the Fourier spectrum becomes complex. Therefore, manual selection of the besecting frequency is not only difficult but also error-prone, which motivated Wang [38] to replace it with an autoregressive power spectrum. Changing the spectrum does not solve the problem of signal decomposition under non-stationary or strongly noisy signals. The variety of signals will make the selection of frequency bands difficult. It is necessary to study and explore this to find the most suitable besecting frequency to segment the useful frequency band and interference and add adaptability to the algorithm.

Similarly, Gilles [39] proposed a spectral segmentation method based on Meyer wavelet and named it empirical wavelet transform (EWT). EWT divides the signal in the spectrum. The maximum and minimum of the spectrum are used to distinguish useful modes. In earlier versions, the midpoint or minimum of adjacent maxima was used as the boundaries [40-42]. Then, EWT was quickly applied after it was proposed. Premjith [43] uses EWT for Audio Data Authentication. Jiang [44] used EWT to separate the part of the bearing signal containing inner ring fault and outer ring fault, and then used the duffing oscillator to identify the fault information. EWT is also used to judge internal fault current and inrush current in a power transformer [45]. Chen [46] combined clustering and EWT to suppress strong noise in seismic

signals. In addition, EWT is also applied to hyperspectral image classification [47], inspecting debonding defects [48], and so on. It is widely used in rotating equipment such as wind turbine [49], motor bearing [50], bearing with varying speeds [51], and railway axle bearing [52]. Kedadouche [53] proved through simulation and experimental signals that EWT is more effective than EMD in processing bearing fault. The above methods have good results when processing clean or stationary signals, but it is difficult to successfully segment complex signals [54]. In order to reduce parameter input and increase the adaptability of EWT, Gilles [55] proposed a parameterless method based on scale-space in 2014 to find useful modes from histograms. Otsu's method and k-means method are used as reference for readers. After this method was proposed, it was quickly and successfully applied to bearing fault diagnosis [56] and rotor rubbing fault diagnosis [57]. Pan [58] found a suitable scale space curve with pre-determined scale parameter through a large number of experiments. Pearson's correlation coefficient is cited to filter components with fault information [56,58]. Amezquita - Sanchez [59] uses multiple signal classification to calculate the new spectrum, and treats the minimum value near the maximum value as the boundaries after zeroing the part below the threshold. Research on the rules for allocating frequency bands is constantly being updated. Faced with more complex signals, more general spectral segmentation algorithms are worth studying.

Given that the frequency slice wavelet transform (FSWT) proposed by Yan [60, 61] has strong time-frequency identification properties and cleaner filtering properties, we explore the application value of FSWT in the field of spectral segmentation. The method analyzes the FSWT by frequency resolution and Dirac function and selects a new scaling function to specify the observation frequency to extract useful information[62]. Liu [63] used this method of decomposing signals from the time/frequency domain and improved the positioning accuracy of the beam damage. Duan [64] combined FSWT and kurtosis to apply this method to the diagnosis of rolling bearing damage and achieved certain results. Guo [65] performs detailed feature analysis on the specified frequency slice interval based on the full-band time-frequency energy distribution of FSWT and uses it for feature extraction of blasting vibration signals. In addition, Yan [66] explored the modal signals separation and damping identification.

After the above analysis methods are introduced into the field of mechanical fault diagnosis, the non-stationary and nonlinear vibration signal processing and fault feature extraction technology has been developed rapidly.

1.3 Kurtogram and component selection indicators

With the development of decomposition methods, various statistical indicators also have more applications. Dwyer [67] proposed the spectral kurtosis (SK) to represent the non-Gaussian components in the signal and their location in the frequency domain. SK is a very powerful statistical tool used in place of power spectral density. Pagnan and Ottonello [68] revised the definition of spectral kurtosis and used short-time Fourier transform to optimize spectral kurtosis to recover random signals corrupted by steady-state noise. Geoff [69] proposed the Maximum correlated Kurtosis deconvolution to detect periodic and impulsive vibration behavior in gears and bearings. Capdevielle[70] used the theory of higher order statistics and gave a more formal definition on the theoretical basis. Although this definition cannot effectively obtain the feature components of non-stationary signals, it has inspired many scholars to conduct in-depth research on it. Borghesani [71] explored the relationship between squared envelope spectrum, kurtosis and cepstrum pre-whitening, providing a theoretical starting point for deriving new metrics. He[72] successfully identified multiple faults in rotating

machinery after combining minimum entropy deconvolution with spectral kurtosis. Meanwhile, multiple fault detection methods based on spectral kurtosis and minimum entropy deconvolution have also been proposed [73]. After the concept of spectral kurtosis was proposed, it has been widely used in the fields of bearings and gears [74]. Xiang [75] combined probabilistic principal component analysis and spectral kurtosis to effectively suppress noise and low-frequency interference. After combining SK and autoregressive AR models, Cong [76] eliminated the interference frequency components, providing theoretical verification for early fault diagnosis. Arivazhagan [77] uses the SK and Teager Kaiser energies of the optimal Gabor subband to identify ship targets. Barszcz [78] used spectral kurtosis to detect cracks in wind turbine planetary gear teeth. When studying the correlation performance of the four-way reversing valve, Wang [79] introduced SK to separate the FIV pulse signal from the background noise. In order to improve the theory of spectral kurtosis, Antoni[80,81] elaborated the relevant theory of spectral kurtosis in detail, and formally gave the mathematical definition of spectral kurtosis. The spectral kurtosis is defined as the energy-normalized fourth-order spectral cumulant.

Antoni [82] not only proved that the new definition of SK has good effect on feature detection of non-stationary signals in noise, but also proposed the Fast Kurtogram (FK) method. Fast Kurtogram uses 1/3-binary tree filter bank to segment the spectrum and extracts each frequency band through finite impulse response (FIR) filters and calculates its spectral kurtosis. This method has been widely used since its appearance [83]. Fast Kurtogram was used by Zhang [84] to estimate the fault frequency band. The obtained frequency band would be input into the genetic algorithm to reduce the calculation time and make the final results have better demodulation effect. Wang [85] adopted the method of dividing the spectrum equally to construct the boundary of the filter, which improved the computational efficiency. This new technique based on dual-tree complex wavelet transform and Kurtogram still has drawbacks. The meaning of the center frequency and frequency conversion bandwidth obtained by dividing the spectrum equally cannot be explained theoretically, which means that the results cannot reflect the real situation. In order to improve the limitation of FIR filter, Similarly, Peter [86] and Wang [87] introduced wavelet packet transform (WPT) and calculated the sparsity measurements of the power spectra from the envelopes of the wavelet packet coefficients to determine resonant frequency bands. The improved IESFOgram by Mauricio [88] did not change the basic framework of Kurtogram, but replaced it with new indicators. Although kurtosis is sensitive to non-stationary characteristics, it is vulnerable to noise. In view of this, Antoni [89] proposed Infogram based on spectral negentropy (SNE) in 2015. The proposed spectral negentropy, similar to spectral kurtosis, is more sensitive to periodic pulses and more resistant to noise. Spectral negentropy was applied by Feng [90] to planet bearing fault diagnosis. Wang [91] calculated Fast Kurtogram of fault signal and health signal respectively, then extracted fault frequency band by spectral kurtosis ratio, and applied this method to planet bearing fault detection. The common feature of the above improved method is the average spectrum segmentation. Although this method can improve the operation efficiency, it reduces the accuracy and has limitations. Moshrefzadeh [92] made more improvements on this basis. First, the Maximal Overlap Discrete Wavelet Packet Transform is used to replace the FIR filter in the Kurtogram. The kurtosis of the unbiased autocorrelation of the squared envelope of each component is used to upgrade the kurtosis.

Some authors have made a series of improvements to the problem of spectrum segmentation: Wang and Liang [93] adopted the average segmentation method. The method adaptively determines the bandwidth and center frequency of the filter by incorporating a right

expansion window to maximize the filtered signal kurtosis. Although it is very difficult to preset the window width, it breaks the conventional thinking mode. However, the method of merging windows does not change the disadvantage of average spectrum segmentation. Sweeping mode is very complex and takes a long time. T. Barszcz [94] obtained the center frequency by pre-estimating the optimal bandwidth and scanning the whole band, which is closer to the real one. Another adaptive spectral kurtosis method used Morlet wavelet to construct filter banks, and the center frequency was defined by wavelet correlation filtering [95]. In order to optimize spectrum segmentation, Xu suppresses the diagnostic error caused by spectrum segmentation by sweeping [96] and order statistics filter [97]. Feng [98] used maximum correlation kurtosis deconvolution to preprocess the signal, which can enhance the periodic pulse component of the vibration signal. In fact, the process has a large uncertainty, and this step has a high possibility of weakening the useful information in the signal. Obviously, the above methods all have their limitations. Neither replacing the filtering structure nor changing the filtering metrics have fundamentally improved the basic framework of Fast Kurtogram [99]. In view of this, it is necessary to explore more reasonable adaptive spectral segmentation methods in the field of multi-level spectral segmentation similar to Fast Kurtogram.

1.4 Signal fusion method

When performing condition monitoring or fault diagnosis of equipment, it is a common method to use multi-sets of sensors to collect vibration acceleration signals in multiple directions. But for many devices, the contact-less method for data acquisition is not only safer than multi-channel sensors, but can also avoid problems such as power supply difficulties, installation difficulties, and data transmission. Therefore, although it is difficult to process acoustic signals, it can solve the problems of many common sensors. Adam Glowacz [100] applies acoustic signal fault detection methods to three-phase induction motor and stator faults of the single-phase induction motor [101]. This non-contact signal processing method provides researchers with new ideas and enlightenment. Subsequently, Lu [102] and Hu [51] used the non-contact acoustic signal detection method to successfully diagnose the rolling bearing fault, which broadened the field of it. In addition, the acoustic signal fault detection method has also been extended to centrifugal pump [103] by scholars.

For high-speed bearing signals, short data may contain a large amount of fault information, while a low-speed heavy-duty acoustic signal not only contains a long amount of data, but also contains a lot of noise which brings more challenges to fault diagnosis. There are many fault diagnosis methods for a single set of data. The operating signals of mechanical equipment are complex, which may include vibration information of parts, modulation signals, noise generated by collisions between materials, and strong environmental noise. These noises can cause great distress to sinle-level spectral segmentation method which needs to determine the important frequency. For analytical mode decomposition, the number and location of the bisecting frequency determine the quality of the final result. The median frequency of adjacent important frequencies will be defined as bisecting frequency. Through iteration, bisecting frequencies will divide the spectrum into several frequency bands and each frequency band is corresponds to a result. In order to reduce the difficulty of manually selecting bisecting frequency, Zhao [104] uses chaotic particle swarm optimization algorithm and auxiliary signal to calculate the best cutoff frequency. Rikam [105] used periodogram estimation of the power spectral density of the three-phase current space vector to detect and diagnose bearing faults in three-phase asynchronous equipment.

These are good ideas, but they did not solve the problems of synchronization of multiple groups of long data and adaptive spectrum segmentation. Bendoumia [106] tried a two-channel acoustic signal processing method and obtained good results. Jeon [107] uses multi-channel distributed speakers to optimize production and localize vibration. Hamdan [108] designed the Multichannel crosstalk cancellation system on the basis of singular value decomposition. Subsequently, more channels of signal fusion methods appeared. Salah [109] uses Quaternion discrete Fourier transform to process audio watermarking. Martins [110] avoids avionics curvature parametric rotation locking with the help of quaternions. Yi [111] uses the phase space reconstruction method to form the signals of the four channels into their own Hankel matrix to obtain the quaternion trajectory matrix, which realizes the fault diagnosis of mechanical equipment. Ma [112] combined symplectic geometry, SSA and Quaternion to capture the characteristic frequency of faults in gear fault diagnosis. It can be seen that Quaternion can play a very important role in the process of multi-channel or multi-group signal synchronization[113].

1.5 Structure of the Thesis

Bearings in rotating equipment usually run at a constant speed. When the bearing is damaged, we can extract the information containing the fault characteristics in the signal to diagnose the fault location. There are serious mode aliasing and redundancy in traditional one-dimensional signal processing methods and single-level spectral segmentation methods. In this paper, after studying the analytical mode decomposition, frequency slice wavelet transform, empirical wavelet transform and quaternion, the fixed spectral segmentation framework in the traditional Kurtogram algorithm is upgraded to a variable spectral segmentation framework. Subsequently, the bearing inner ring and outer ring data are used to verify the effectiveness of the proposed algorithm. The main contents of the paper mainly include the following:

Chaper 1 expounds the background, research significance and research status of the topic, including modern signal decomposition, multi-level spectral segmentation methods, etc., which provides a theoretical basis for the improvement of the method and the experimental verification.

Chaper 2 proposed Ailinggram to optimize analytical mode decomposition. The framework relies on the variability of the window width and envelope estimation characteristics of order statistics filter to increase the diversity of the center frequencies and bandwidth. A novel harmonic correlation index is designed to identify the characteristics of rotating machinery faults from various levels of results, and to improve the usability in mechanical equipment fault diagnosis.

Chapter 3 constructs the tower-shaped boundary distribution diagram through the fluctuation of the Fourier spectrum.The frequency slice function is used to extract each frequency band to obtain better filtering effects than the finite impulse response filter. Finally, the proposed novel correlation spectral negentropy is sensitive to periodic pulses and can be used to screen the component that contains the most fault information.

Chapter 4 proposes W-Autogram and weighted unbiased autocorrelation based on the variability of the PSD window width to extract specific information. Simulation signals and experimental results verify that the proposed method can be applied to the fault diagnosis of rolling bearings in rotating machinery. Then this chapter proposed Harmonic spectral kurtosis which can extract the harmonic information in the envelope spectrum, quantify the periodic pulses in the signal, and suppress the influence of interference such as random pulse.

Chapter 5 proposed quaternion analytical mode decomposition (QAMD) to process multiple acoustic signals and extract fault information in industrial machinery systems with high sampling frequency, low speed, and heavy load. QAMD can separate characteristic information from frequency domain and extend it to the fault diagnosis of rotating industrial machinery.

Chapter 6 made the conclusions and provided insights into future work for the intelligent fault diagnosis.

1.6 List of Publication

1.6.1 Journal Publications

[1] **張坤**, 廖志強, 唐海紅, 宮崎修治, 陳山鵬, 逐次統計フィルタに基づく経験的周波数スライスウェーブレット変換と軸受故障診断への応用, 日本設備管理学会誌, 2020, 32(4): 119-125.

[2] **Kun Zhang**, Chaoyong Ma*, Yonggang Xu, Peng Chen, Jianxi Du, Feature extraction method based on adaptive and concise empirical wavelet transform and its applications in bearing fault diagnosis, *Measurement*, 2021, 172: 108976. (IF=5.131, Q1)

[3] **Kun Zhang**, Yonggang Xu*, Peng Chen. Feature extraction by enhanced analytical mode decomposition based on order statistics filter, *Measurement*, 2021, 173: 108620. (IF=5.131, Q1)

[4] **Kun Zhang**, Yonggang Xu*, Zhiqiang Liao, Liuyang Song, Peng Chen, A novel Fast Entrogram and its applications in rolling bearing fault diagnosis, *Mechanical Systems and Signal Processing*, 2021, 154: 107582. (IF=8.934, Q1, TOP)

[5] **Kun Zhang**, Weikang Tian, Peng Chen, Chaoyong Ma, Yonggang Xu*, Sparsity-guided multi-scale empirical wavelet transform and its application in fault diagnosis of rolling bearings, *Journal of the Brazilian Society of Mechanical Sciences and Engineering*, 2021, 43: 398. (IF=2.181, Q2)

[6] **Kun Zhang**, Ling Shi, Yue Hu, Peng Chen, and Yonggang Xu*, Variable spectral segmentation empirical wavelet transform for noisy signal processing, *Digital Signal Processing*, 2021, 117: 103151. (IF=2.92, Q1)

[7] **Kun Zhang**, Peng Chen, Miaorui Yang, Liuyang Song, Yonggang Xu*, The Harmogram: A periodic impulses detection method and its application in bearing fault diagnosis, *Mechanical Systems and Signal Processing*, 2022, 165: 108374. (IF=8.934, Q1, TOP)

[8] **Kun Zhang**, Haihong Tang, Peng Chen, Yonggang Xu*, Aijun Hu, A method for extracting fault features using variable multi-level spectral segmentation framework and harmonic correlation index, *IEEE Transactions on Instrumentation and Measurement*, 2022, 71: 3505109. (IF=5.592, Q1)

[9] **Kun Zhang**, Yunjie Deng, Peng Chen, Chaoyong Ma, Yonggang Xu*, Quaternion Empirical Wavelet Transform and Its Applications in Rolling Bearing Fault Diagnosis, *Measurement*, 2022, 195: 111179. (IF=5.131, Q1)

[10] Yonggang Xu, Yunjie Deng, Chaoyong Ma, **Kun Zhang***, The Enfigram: A robust method for extracting repetitive transients in rolling bearing fault diagnosis, *Mechanical Systems and Signal Processing*, 2021, 158: 107779(IF=8.934,, Q1, TOP)

[11] Zhipeng Sheng, Yonggang Xu, **Kun Zhang***, Applications in bearing fault diagnosis of an improve Kurtogram algorithm based on flexible frequency slice wavelet transform filter bank, *Measurement*, 2021, 174: 108975. (IF=5.131, Q1)

[12] Ling Shi, **Kun Zhang***, Application of Variable Spectral Segmentation Method in Fault

Detection of Rolling Bearings, *International Journal of Comprehensive Engineering*, 2020, 9(1): 23-24.

1.6.2 International Conference Publications

[1] **Zhang Kun**, Liao Zhiqiang, Jinyama Ho, Application of a New Spectral Decomposition Method in Bearing Fault Diagnosis. 日本機械学会, 第 18 回評価・診断に関するシンポジウム講演論文集: 2019: 116-121.

Chapter 2
Multilevel spectral segmentation method based on order statistics filter and analytical modal decomposition and its application in bearing fault diagnosis under high speed and dynamic load conditions [33, 34]

2.1 Introduction

Since the signal of electrical or mechanical equipment is more complex than that of buildings, it may contain modulation information, material impact vibration, strong environmental noise, etc. This is a huge challenge for analytical modal decomposition (AMD), and it has received very few applications in past research. The core of AMD is correctly determining useful components or bisecting frequencies, which will affect the success rate of feature extraction. AMD needs to manually observe the Fourier spectrum and then define specific frequency bands or high-amplitude frequencies as useful components. The median frequency of adjacent useful components is the bisecting frequency which can divide the signal into high-frequency part and low-frequency part. The mode is similar to using a low-pass filter to remove noise.

This chapter proposed a novel variable spectral segmentation method to optimize AMD and distinguish modes. The proposed method uses order statistics filter to automatically identify useful modes from the spectrum, which means that the original observation method will be discarded. The basic modes are unevenly distributed in the spectrum, and the computational efficiency and accuracy are improved. Further, multi-level spectral segmentation framework called Ailinggram is designed to expand low-pass filter in the original AMD into multiple sets of band-pass filters. Ailinggram draws on the ideas of the traditional Fast Kurtogram construction framework but supplements and corrects its shortcomings. Different from the fixed frame in the traditional Fast Kurtogram, Ailinggram focus on the variability of order statistics filter and envelope estimation characteristics which can be used to construct signal-related variable spectral segmentation framework. The calculation process of Ailinggram provides multiple center frequencies and flexible bandwidths for the subsequent screening steps. The adaptability of the algorithm is improved, and the noise can be separated in multiple stages. The new variable frame inherits the strategy of the traditional Kurtogram and makes up for the shortcomings of the fixed frame, providing more flexible possibilities for signal processing and fault diagnosis. This chapter introduces a novel harmonic correlation index (HCI) for identifying feature information from the results of each level and improving the usability of Ailinggram in non-stationary signal processing and mechanical equipment fault diagnosis.

2.2 Traditional analytical mode decomposition method

2.2.1 Basic definition of analytical mode decomposition

Different form the data-driven decomposition method, AMD extracts the signal from the spectrum. For the signal $x(t)$ which consists of two components:

$$x(t) = x_{c1}(t) + y_{c2}(t) \tag{2.1}$$

Among them, the frequencies of $x_{c1}(t)$ and $x_{c2}(t)$ are important frequencies: ω_{c1}, ω_{c2}, which can be seen in Fig.1. Reference [32] takes the average of adjacent important frequencies

as the bisecting frequency: $\omega_b = \frac{\omega_{c1}+\omega_{c2}}{2}$. If $\hat{X}(\omega)$ is used to represent the Fourier transform of $x(t)$, then ($|\omega_{c1}| < \omega_b < |\omega_{c2}|$). Let $s_k(t)$ denotes a sine or cosine function whose frequency is equal to the bisecting frequency. When $k = c$, $s_k(t) = s_c(t) = \cos(\omega_b t)$; $k = s$, $s_k(t) = s_s(t) = \sin(\omega_b t)$. The Hilbert transform ($H[\bullet]$) of $s_k(t)x(t)$ can be expressed by the following formula:

$$H[s_k(t)x(t)] = H[s_k(t)x_{c1}(t)] + H[s_k(t)x_{c2}(t)] \tag{2.2}$$

According to the Bedrosian theorem, Eq.2.2 can be rewritten as:

$$H[s_k(t)x(t)] = x_{c1}(t)H[s_k(t)] + s_k(t)H[x_{c2}(t)] \tag{2.3}$$

Substituting c and s into Eq.2.3 respectively can be obtained:

$$\begin{cases} H[s_c(t)x(t)] = x_{c1}(t)H[s_c(t)] + s_c(t)H[x_{c2}(t)] \\ H[s_s(t)x(t)] = x_{c1}(t)H[s_s(t)] + s_s(t)H[x_{c2}(t)] \end{cases} \tag{2.4}$$

Then,

$$\begin{cases} H[x_{c2}(t)] = \frac{H[s_c(t)x(t)] - x_{c1}(t)H[s_c(t)]}{s_c(t)} \\ H[s_s(t)x(t)] = x_{c1}(t)H[s_s(t)] + s_s(t)\frac{H[s_c(t)x(t)] - x_{c1}(t)H[s_c(t)]}{s_c(t)} \end{cases} \tag{2.5}$$

So such results can be obtained:

$$\begin{cases} y_{c1}(t) = \frac{s_s(t)H[s_c(t)y(t)] - s_c(t)H[s_s(t)y(t)]}{s_s(t)H[s_c(t)] - s_c(t)H[s_s(t)]} \\ H[y_{c2}(t)] = \frac{H[s_c(t)]H[s_s(t)y(t)] - H[s_s(t)]H[s_c(t)y(t)]}{s_s(t)H[s_c(t)] - s_c(t)H[s_s(t)]} \end{cases} \tag{2.6}$$

Since the Hilbert transform of $s_s(t)$ is $H[s_s(t)] = -\cos(\omega_b t)$, the Hilbert transform of $s_c(t)$ is $H[s_c(t)] = \sin(\omega_b t)$, and $s_s(t)H[s_c(t)] - s_c(t)H[s_s(t)] = 1$. Therefore, Eq.2.6 can be simplified to:

$$\begin{cases} y_{c1}(t) = s_s(t)H[s_c(t)y(t)] - s_c(t)H[s_s(t)y(t)] \\ H[y_{c2}(t)] = H[s_c(t)]H[s_s(t)y(t)] - H[s_s(t)]H[s_c(t)y(t)] \end{cases} \tag{2.7}$$

Finally, $y_{c2}(t)$ can be calculated by Eq.2.1.

In AMD, how to determine the "important frequency" or "bisecting frequency" is the most difficult step. At present, only a few scholars have conducted in-depth research on the selection of important frequency. Moreover, the manual selection of important frequency by means of observation has a great obstacle to the application of the method in the condition monitoring system.

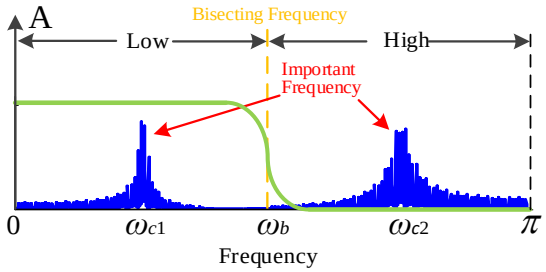

Fig.2.1 Schematic diagram of the AMD method.

2.2.2 Pitfalls and inadequacies of AMD

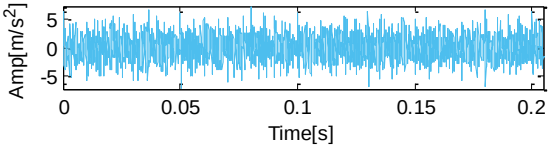

Fig.2.2 The wavelet of simulated signal.

In order to simulate the failure of the rotating machine, a simulation signal was constructed.

$$\begin{cases} s_{c1} = A_1 e^{-g\times 2\pi f_n t} \times \sin\left(2\pi f_n t \times \sqrt{1-g^2}\right) \\ s_{c2} = A_2 \sin(2\pi f_1 t)\sin(2\pi f_2 t + \sin(2\pi f_3 t)) \\ s_{c3} = A_2 \sin(2\pi f_1 t)\sin(2\pi f_4 t + \sin(2\pi f_3 t)) \\ s_1 = s_{c1} + s_{c2} + s_{c3} + \zeta \end{cases} \tag{2.8}$$

where the damping coefficient $g = 0.07$, $f_1 = 50$ Hz, $f_2 = 1000$ Hz, $f_3 = 100$ Hz, $f_4 = 4000$ Hz. The natural frequency of the periodic pulse information is $f_n = 2500$ Hz. The amplitude $A_1 = 5\text{m/s}^2$, $A_2 = 2\text{m/s}^2$, $\zeta = \text{SNR(3dB)}$. The waveform is shown in Fig.2.2.

The first step in AMD is to segment the spectrum, five frequencys [488Hz, 1435Hz, 3574Hz, 4473Hz] can be set as "bisecting frequency". So, five AMs would be extracted and shown in Fig.2.3. AM-1 and AM-5 are noises; AM-2 and AM-4 are amplitude modulated signals corresponding to components s_{c2} and s_{c3}; the periodic pulse information in AM-3 is obvious, corresponding to component s_{c1}.

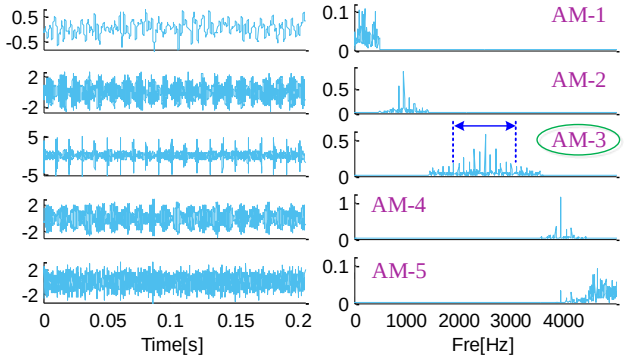

(a) Waveforms of AMs (b) The spectra of AMs

Fig.2.3 The results decomposed by AMD.

In order to verify the superiority of the extraction method, a traditional adaptive modal decomposition method (empirical mode decomposition, EMD) is introduced here. EMD decomposed the signal into 12 IMFs. The first 4 components have more than 90% of the energy, while the 5th and subsequent components are concentrated in the low frequency portion, which are invalid components. By superimposing the invalid components on IMF-5, the waveforms and spectra of IMF-1 to IMF-5 can be shown in Fig.2.4. IMF-1 contains s_{c3}, which also contains part of s_{c1}; IMF-2 contains not only most of the energy of s_{c1} but also part of s_{c2} and s_{c3}. Therefore, there is modal aliasing between IMF-1 and IMF-2.

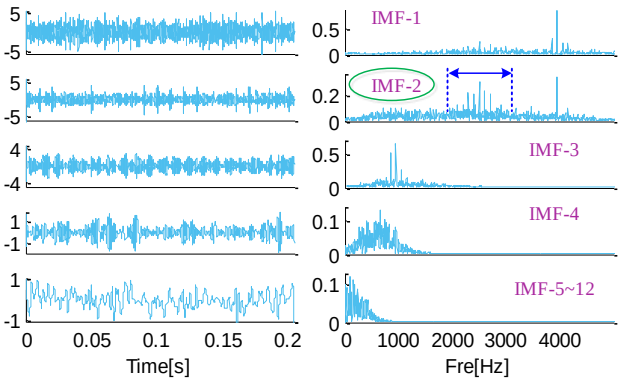

(a) Waveforms of IMFs (b) the spectra of IMFs

Fig.2.4 The results decomposed by EMD.

In order to measure the difference among the components extracted by the two methods, the root mean square(RMS) was used.

$$\mathrm{RMS} = \sqrt{\frac{1}{N}\sum(s_n - s_o)^2} \tag{2.9}$$

where s_o is the component of the original signal and s_n is the component extracted by AMD or EMD.

The comparison of the errors of primary components extracted by the two methods was shown in Fig.2.5. The error of EMD is larger than that of AMD.

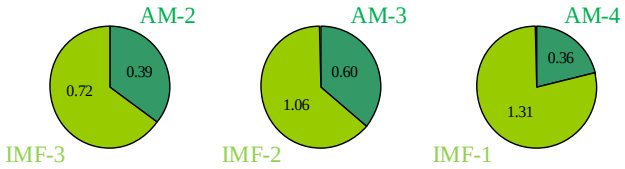

(a) Sc2: fc=1000Hz (b) Sc1: fc=2500Hz (c) Sc3: fc=4000Hz

Fig.2.5 Comparison of the error of three components.

Simulation of s_{c1} for periodic pulses, AM-3 for AMD and IMF-2 for EMD are plotted in Fig.2.6. The repetition between AM-2 and s_{c1} is higher and can be confirmed in the details. The three parts of [0-0.008s], [0.03s-0.038s] and [0.17s-0.178s] were extracted and displayed. In [0-0.008s], IMF-2 has endpoint effect and a mutation at 0.0035s. But the endpoint of AM-3 is convergent. In [0.03s-0.038s], IMF-2 has energy loss and large error. But AM-3 has almost no energy loss. At 0.176s in Fig.2.6b, IMF-2 has a mutation. The energy of each pulse obtained by AM-3 is balanced, without many singularities. The main reason for the above is the difference in filtering. EMD relies on extreme points to extract high frequency components from the signal. AMD can split the high and low frequencies from the Fourier spectrum and weaken the modal aliasing. The representative filter that calculates the mode from the spectrum is the finite impulse response (FIR) filters, which can be used to verify the effectiveness of AMD in filtering(Fig.2.7).

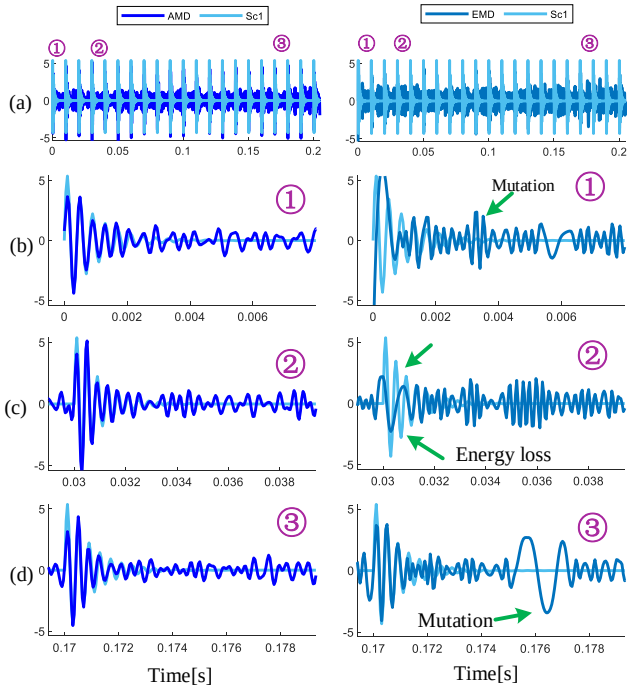

Fig.2.6 Comparison of the results decomposed by AMD and EMD.

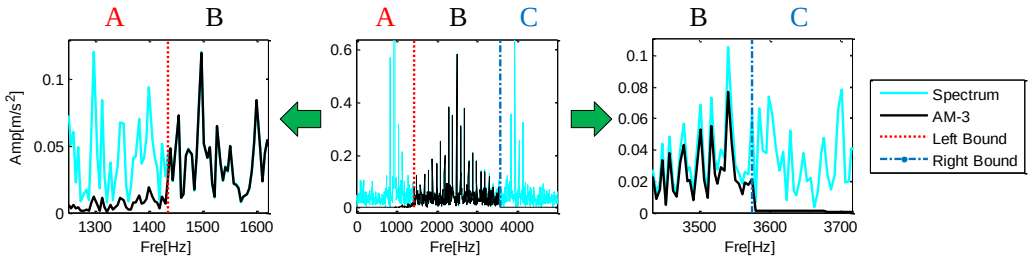

(a) The filtering effects of the AMD method

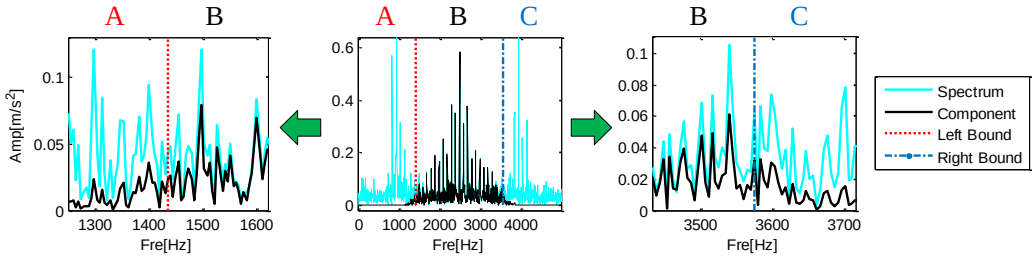

(b) The filtering effects of FIR

Fig.2.7 The filtering effects of (a) AMD and (b) FIR.

The leakage ratio of the two methods is 2.72% and 3.95%, as shown in Fig.2.8a. At the position of part B near the left boundary, AMD has almost no energy leakage, and FIR has a small amount of leakage. For part C, AMD has almost no energy leaks, but FIR has it. The leakage ratio of the two methods is 1.13% and 4.86%, as shown in Fig.2.8b. The results obtained by the two methods also have a small amount of energy loss in part B. After calculation, the energy loss of AMD was 3.07% and the FIR was 5.49%. It can be seen that AMD leaks less energy in part A and part C, losing less energy in part B. Therefore, the proposed method has a better filtering effect than the traditional FIR filter.

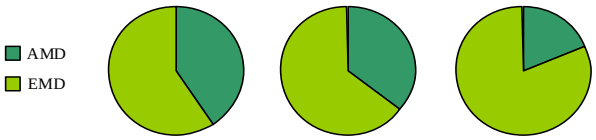

(a) Part A: Leakage ratio: (b) Part B: Loss ratio: (c) Part C: Leakage ratio:

Fig.2.8 Comparison of FIR and AMD filtering effects.

2.3 Variable spectral segmentation analytical mode decomposition

2.3.1 Order statistics filter

Order statistics filter is a statistical estimation method that can be used to estimate the upper, lower, or median of the data. This section proposed an OSF-based trend spectrum estimation method. The maximum value filter is more susceptible to the influence of the peak value; the minimum value filter is more susceptible to the influence of the valley value; the average value filter is closer to the signal trend. In this section, the data processed by the filter is the spectrum. The value in the spectrum is positive, and there is more useful information in the peak, so this article uses the maximum filter. Take $a = [2,8,9,12,8,13,10,8,6,5,7,8,5,9,6,4,3,2,1,3,5,6,3,2]$ as an example (Fig.2.9a). The data length is 24, and 5 peaks are gathered in three frequency bands. OSF can obtain the upper envelope of the data by calculation. The data in the first window is [2,8,9], and the maximum value 9 should be extracted. The second group is [8,9,12], the maximum value is 12. The maximum value in each

window should be extracted to form a new sequence: [2,9,12,12,13,13,13,10,8,7,8,8,9,9,9,6,4,3,3,5,6,6,6,2]. As shown in Fig.2.9b. The fluctuations in the original data have 5 peaks and 4 valleys. The new sequence has 5 flat tops and 2 valleys. The trend spectrum estimation method uses the valley values as the demarcation points. The boundaries are set at the 10th point and the 19th point. The signal will be divided into three parts. This method can be applied to find the important frequencies in the spectrum.

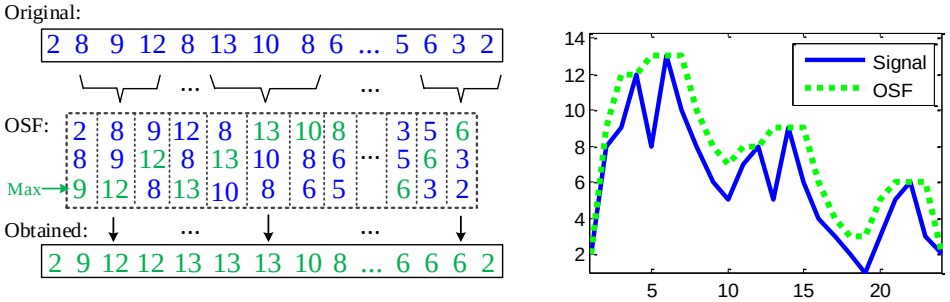

(a) Order statistics filter (b) Original data and the obtained data

Fig.2.9 Trend spectrum estimation method based on OSF.

The waveform is shown in Fig.2.10a. This is an amplitude modulation signal. The amplitude of the signal varies greatly. The upper envelope and lower envelope obtained by OSF have fewer extreme points than the original signal. The mean of the envelope approximate the trend of the signal. Then, the spectrum of the signal is shown in Fig.2.10b. The signal contains several low frequency components. The OSF-based trend spectrum estimation method adds a "flat top" above the spectrum. The valley between the flat tops divides the spectrum into several independent components. By amplifying the frequency band between 100 Hz and 160 Hz, the component with lower amplitude can also be divided, which means that the amplitude of the signal has less influence on the OSF. Amplitude can affect OSF, but OSF can also detect small amplitude components. The OSF has reliable envelope capability and filtering characteristics.

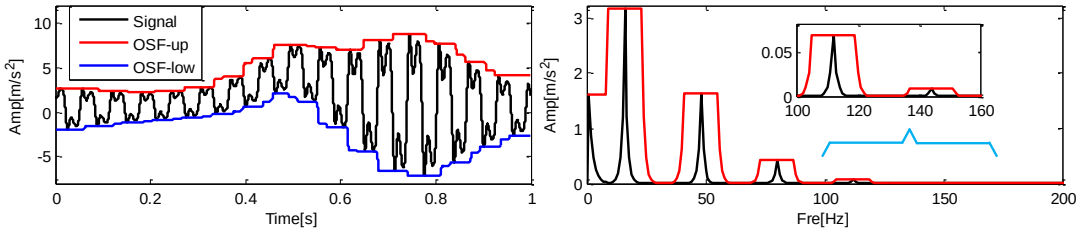

(a) Simulated signal and its envelope (b) Spectrum and its envelope

Fig.2.10 The simulated signal decomposed by OSF.

2.3.2 Single-level spectral segmentation based on OSF and AMD

Analytical mode decomposition can identify effective information from the Fourier spectrum. This section proposed a variable spectral segmentation method to optimize AMD which is mainly reflected in the design and selection of bisecting frequency. The complex Fourier spectrum contains rich information, especially the characteristic information hidden in the noise will not be filtered out. Different from the simulated signal, the collected signal may contain modulation of the drive module, environmental noise, pulses caused by accidental interference, fault information, etc. They interfere with each other and are difficult to distinguish, and may also appear in any frequency band. Noise often exists in the entire spectrum, the energy of other components is concentrated near the nature frequency, and more than 95% of the energy is contained in a certain bandwidth. AMD manually defines different

center frequencies, which wastes time and causes errors. Since each component in the signal may appear in any frequency band, this section uses order statistics filter (OSF) with statistical estimation characteristics to roughly calculate the location and quantity of the bisecting frequency. If x(t) is used to represent the signal, x_i represents the i-th component contained in the signal. The signal can be written as:

$$x(t) = \sum_{i=1}^{M} x_i(t) \tag{2.10}$$

Let $\hat{X}(\omega)$ represents the Fourier spectrum of $x(t)$. The important frequency or center frequency of $x_i(t)$ can be defined as ω_{ci}. The position between important frequencies is called bisecting frequency, which is represented by ω_{bi}. The bandwidth is $\Delta\omega_i = \omega_{bi} - \omega_{b(i-1)}$. The component located in this interval can be described as $x_i(t; \omega_{ci}, \Delta\omega_i)$ in time domain. Therefore, Eq.2.10 can be rewritten as:

$$x(t) = \sum_{i=1}^{M} x_i(t; \omega_{ci}, \Delta\omega_i) \tag{2.11}$$

All bisecting frequencies are redefined as boundaries:

$$\begin{cases} |\omega_{c1}| < \omega_{b1} \\ \omega_{b1} < |\omega_{c2}| < \omega_{b2} \\ \omega_{b2} < |\omega_{c3}| < \omega_{b3} \\ \cdots \\ \omega_{b(M-1)} < |\omega_{cM}| \end{cases} \tag{2.12}$$

Acoording to Eq.2.6 and Eq.2.7， the results can be written as:

$$\begin{cases} x_1(t) = \frac{s_s(t)H[s_c(t)x(t)] - s_c(t)H[s_s(t)x(t)]}{s_s(t)H[s_c(t)] - s_c(t)H[s_s(t)]} \\ H[x_{Res1}(t)] = \frac{H[s_c(t)]H[s_s(t)x(t)] - H[s_s(t)]H[s_c(t)x(t)]}{s_s(t)H[s_c(t)] - s_c(t)H[s_s(t)]} \end{cases} \tag{2.13}$$

$$\begin{cases} x_1(t) = s_s(t)H[s_c(t)x(t)] - s_c(t)H[s_s(t)x(t)] \\ H[x_{Res1}(t)] = H[s_c(t)]H[s_s(t)x(t)] - H[s_s(t)]H[s_c(t)x(t)] \end{cases} \tag{2.14}$$

Therefore, the first component can be extracted by ω_{b1}:

$$\begin{cases} x_1(t) = \sin(\omega_{b1}t)\, H\big[\cos(\omega_{b1}t)\,[x(t)]\big] \\ \qquad\quad - \cos(\omega_{b1}t)\, H\big[\sin(\omega_{b1}t)\,[x(t)]\big] \\ x_{Res1}(t) = x(t) - x_1(t) \end{cases} \tag{2.15}$$

After that, ω_{b2} is used to extract the second component:

$$\begin{cases} x_2(t) = \sin(\omega_{b2}t)\, H\big[\cos(\omega_{b2}t)\,[x_{Res1}(t)]\big] \\ \qquad\quad - \cos(\omega_{b2}t)\, H\big[\sin(\omega_{b2}t)\,[x_{Res1}(t)]\big] \\ x_{Res2}(t) = x_{Res1}(t) - x_2(t) \end{cases} \tag{2.16}$$

The i-th component can be calculated by the following formula:

$$\begin{cases} x_i(t) = \sin(\omega_{bi}t)\, H\left[\cos(\omega_{bi}t)\,[x_{Res(i-1)}(t)]\right] \\ \qquad\quad - \cos(\omega_{bi}t)\, H\left[\sin(\omega_{bi}t)\,[x_{Res(i-1)}(t)]\right] \\ x_{Resi}(t) = x_{Res(i-1)}(t) - x_i(t) \end{cases} \tag{2.17}$$

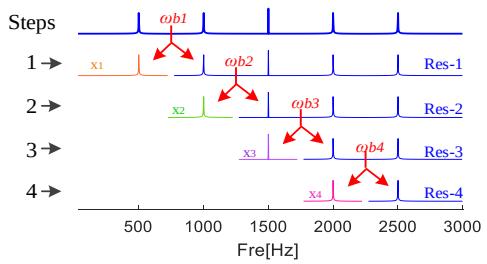

Fig.2.11 Decomposition steps of variable spectral segmentation method

The original signal can be expressed as the sum of several analytical modes and one residual:

$$x(t) = \sum_{i=1}^{M-1} x_i(t) + x_{Resi}(t) \tag{2.18}$$

where $\mathrm{x_{Resi}(t)}$ is the residual component with highest frequency. The cyclic extraction process is described in Fig.2.11:

2.3.3 Variable multi-level spectral segmentation framework

This section designs a multi-level spectral segmentation framework that utilizes the envelope estimation feature on OSF. The multi-level operation construct the framework can enrich the distribution and quantity of the bisecting frequency, which will affect the results of the obtained components. The process of OSF is like a window sliding from the beginning to the end of the data, which means the window width ϖ needs to be set. ϖ is an odd number that greater than 3. The window separates the signal into $N - \varpi + 1$ groups, i-th group is $[\hat{X}(i), \hat{X}(i+1), \hat{X}(i+2), \ldots, \hat{X}(i+\varpi-1)]$, $1 \le i \le N - \varpi + 1$. When ϖ is at the beginning of the data, the previous ϖ data will be wrapped, and the maximum value will be extracted and stored in the new sequence. Move the window step by step to the end of the data, and a new sequence named $Y(n)$ with a length of $N - \varpi_i + 1$ will be obtained. Obviously, $(\varpi_i + 1)/2$ data are missing in $Y(n)$. We use the average of the data in the first window to add $(\varpi_i - 1)/2$ points before $Y(n)$, we use the average of the data in the last window to add $(\varpi_i - 1)/2$ points after $Y(n)$. The length of the new sequence $Y(n)$ is the same as the original data $X(n)$. $Y(n)$ is a positive value which can not only reduce the number of extreme points, but also suppress noise and enhance the modes in the spectrum. If $Y(n)$ is smooth enough, the minimum points can divide the spectrum into several parts. Subsequently, the boundaries can be applied to decompose the signal into several analytical modes (AMs).

The core of the multi-level spectral segmentation framework proposed in this section is to increase the variability of ϖ. Let ϖ_j denote the window width of the j-th level, and $Y_j(n)$ is the corresponding sequence. A large ϖ_j can obtain a smoother upper envelope curve with less extreme points, which is more like the fluctuation trend of the spectrum. A small ϖ_j can obtain a more complex upper envelope curve with plenty of extreme points, which is closer to the prototype of the spectrum. In this section, ϖ_j is set to a gradually increasing variable value with an initial value. Of course, ϖ_j is fixed at each level. The initial ϖ_1 needs to be defined by the generalized extreme point spacing d_{OSF}:

$$d_{OSF} = \frac{N}{n_{eg}} \tag{2.19}$$

where n_{eg} is the number of maximum or minimum values in the discretized Fourier spectrum $\mathrm{X(n)}$, and ϖ_1 is set to be the smallest odd number greater than $\mathrm{d_{OSF}}$. Obviously, the initial ϖ_1 may be a small value. Adding variability to this value can add more possibilities for spectral segmentation. This section sets $\varpi_j = \varpi_{j-1} + 2$. Of course, this cumulative increase of ϖ_j is not the only way. The accumulated value needs to be adjusted according to data of different lengths. When the amount of data is large, the change span of the window width can be appropriately increased. Then, the minimum values of $Y_j(n)$ can be calculated and their positions will be defined as boundaries. A smaller ϖ_j corresponds to a larger number of boundaries and a narrower frequency band. Narrow frequency bands are generally not useful for signal processing. When the number of boundaries is less than 20, the acquired boundaries start to be recorded. With the increase of ϖ_j, $Y_j(n)$ may become a monotonously changing curve, and the

number of boundaries may be zero, which means that the multi-level spectral segmentation framework is successfully established. This new method is named Ailinggram

Following simulated signals are designed to show the framework mentioned above. s_1 is a cosine at 30 Hz; s_2 is a modulation interference signal; the center frequency of interference s_3 is 1200 Hz; s_4 is periodic pulses whose center frequency is 2400 Hz and the bandwidth is 20 Hz.

$$\begin{cases} s_1 = 3\cos(2\pi \cdot 30t) \\ s_2 = \cos(2\pi \cdot 4t) \times \cos(2\pi \cdot 400t) \\ s_3 = 5\sin(2\pi \cdot 35t) \times \sin(2\pi \cdot 1200t + \sin(2\pi \cdot 100t)) \\ \qquad\qquad +0.8\cos(2\pi \cdot 2t) \times \cos(2\pi \cdot 50t) \\ s_4 = \sum_{i=1}^{M} 4e^{-g\times 2\pi f_n^i t} \times \sin\left(2\pi f_n^i t \times \sqrt{1-g^2}\right) \\ s = s_1 + s_2 + s_3 + s_4 \end{cases} \tag{2.20}$$

where the damping coefficient is $g = 0.006$, natural frequency is $f_n = 2400$ Hz, the period of pulses is $T = 0.05$ s. The waveforms and Fourier spectra are shown in Fig.2.12.

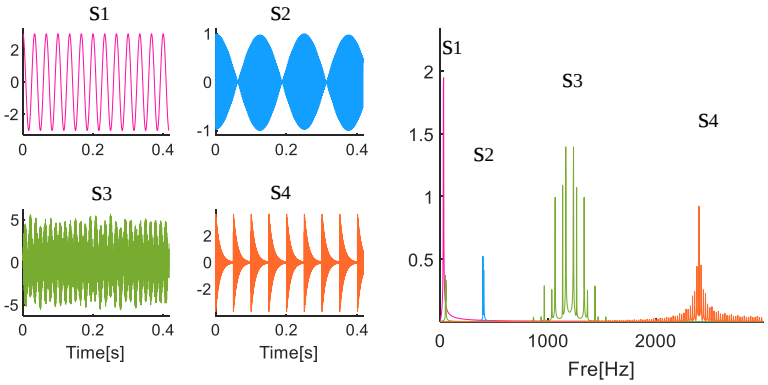

(a) Components (b) Spectrum

Fig.2.12 Signals and Fourier spectrum

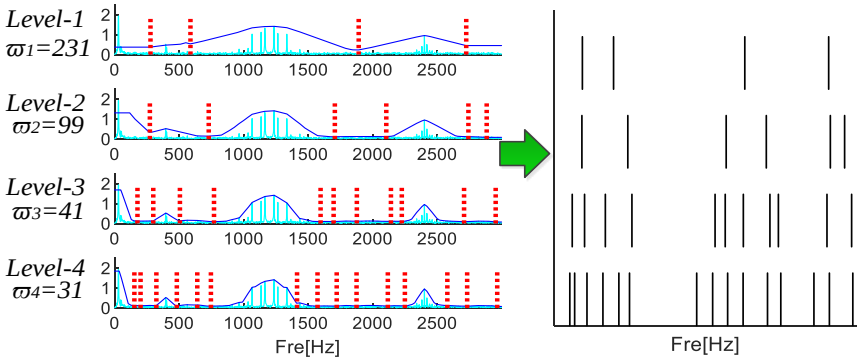

Fig.2.13 Variable multi-level spectral segmentation method

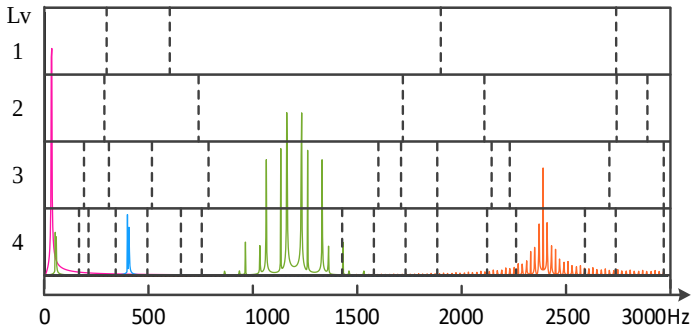

Fig.2.14 The proposed Ailinggram

The energies of components are concentrated around their center frequencies. The

bandwidth of s_1 and s_2 is narrow, the energy of s_3 is concentrated between 1000 Hz and 1500 Hz, and the energy of s_4 is concentrated between 2300 Hz and 2500 Hz. The multi-level spectral segmentation method needs to continuously update the value of ϖ_j to construct the framework. This section adds noise with SNR=8dB to Eq.2.20 and designs four sets of ϖ. The upper envelope curves and the number of boundaries obtained by the four sets of ϖ are different. In Fig.2.13, the curve of ϖ_1 is smooth, which contains 4 minima, which divides the spectrum into 5 parts. When ϖ_2=99, the curve fluctuates, and the number and position of the minimum values change. When ϖ_3=41, more frequency bands are obtained between s_3 and s_4, but their own frequency bands are narrowed, which means that the noise contained in s_3 or s_4 has been reduced. When ϖ_4=31, there are 15 boundaries. Record the position of boundaries after changing the window width, a series of variable spectral segmentation groups can be constructed into a new frame. Fig.2.14 is used as an example to show the "Ailinggram" framework proposed in this section. The position and number of boundaries of each level from Lv-1 to Lv-4 are the same as in Fig.2.13.

2.3.4 Feature screening index based on bearing fault simulation

The method can be applied to processing vibration, sound, electrical pulse and other signals, and can also be applied to the fields of electrical, construction, and machinery. This chapter not only proposed a signal decomposition method, but also looks forward to expanding the method to play roles in more fields. The fault data of this type of rotating equipment often has certain rules. Aiming at these characteristics, this section designs a new indicator and uses simulation signals to demonstrate and verify its effectiveness.

The periodicity of uniform rotating machinery or its parts is usually fixed, which provides a structural basic model for the establishment of new indicators. Whether it is a bearing or gear failure, its periodicity can be predicted. The damage models of bearings are shown in Fig.2.15. The vibration signal usually contains many pulses. Whether looking for pulses in the signal or looking for "cyclostationary" features, existing methods expect that the final result obtained will contain less noise or interference and contain more feature information. How to quantify feature information is the main function of various indicators. The performance of the fault characteristic in time domain is periodic pulses. In the frequency domain, there are many sidebands near the center frequency. The fault characteristics in the signal and Fourier spectrum can be easily masked by various interference or noise contained in the signal. The most convenient and commonly used method is to calculate the Hilbert envelope spectrum of the signal and observe the fault characteristic frequency and its harmonics. Considering that the fault features in the envelope spectrum are more stable and referable, this section introduced a new harmonic correlation index (HCI) to filter the fault frequency band in Ailinggram.

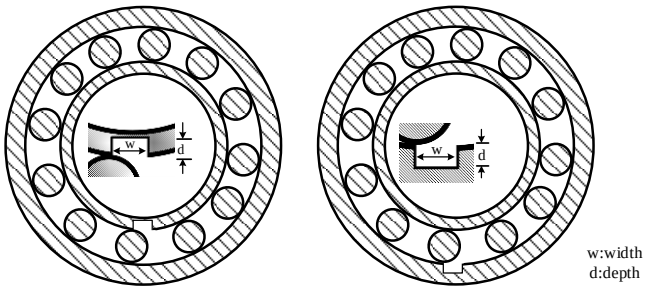

(a) Inner ring fault (b) Outer ring fault

Fig.2.15 Inner ring or outer ring fault and the size of the damage

For electrical or mechanical equipment that may occur damage, the specific information of the bearing model is known. Although it is hard to find the period from the actual collected signal, it is relatively easy to find characteristic frequencies or harmonics from the Hilbert envelope spectrum. HCI does not require all information of bearing, and only needs the fault characteristic frequency to simulate the time domain data of the bearing fault. The Hilbert envelope spectrum of each component becomes the objective function to be analyzed. The correlation between the envelope spectrum of the collected signal and the component would be compared. When their correlation is high, there are high-amplitude fault characteristic frequencies and harmonics in the Hilbert envelope spectrum of the collected signal, which contains a large amount of fault information. When their correlation is low, there is no high-amplitude fault characteristic frequency or corresponding harmonic in the Hilbert envelope spectrum of the collected signal. HCI can avoid the complicated steps of the observation method and provide more possibilities for big data processing.

Eq.2.21 provides a basic model of bearing failure:

$$s(t) = \sum_{i=1}^{M} Ae^{-g\times 2\pi f_n^i t} \times sin\left(2\pi f_n^i t \times \sqrt{1-g^2}\right) \tag{2.21}$$

where f_n is the natural frequency; g is the damping coefficient. Since the object of calculating the correlation is the envelope spectrum, and the natural frequency and the damping coefficient will not interfere with the envelope spectrum, the values of these two parameters can be empirically taken without calculation.

Use $\hat{s}(t)$ to represent the Hilbert transform of the signal:

$$\hat{s}(t) = \frac{1}{\pi}\int_{-\infty}^{+\infty} \frac{s(\tau)}{t-\tau} d\tau \tag{2.22}$$

Remove the trend item: $u(t) = |\hat{s}(t)| - \overline{|\hat{s}(t)|}$. If the Fourier transform of $u(t)$ exists, the data will be:

$$\hat{u}(\omega) = CFT[u(t)] = \int_{-\infty}^{+\infty} u(t)e^{-i\omega t} dt \tag{2.23}$$

The Hilbert envelope spectrum can be expressed as:

$$\hat{v}(\omega) = |\hat{u}(\omega)| \tag{2.24}$$

The simulated fault signal only contains fault information, and there is no noise in its Hilbert envelope spectrum. The collected signal may contain various interferences or strong noises. For similar but slightly different two sets of signals, the Pearson product-moment correlation coefficient (Pearson's correlation coefficient) can be used to measure the linear correlation. Pearson's correlation coefficient is located in [-1,1]. In view of its characteristics, changes in the positions and scales of the two variables will not affect it. The amplitudes of the two envelope spectra to be compared can be normalize to [0,1].

Set $\mathrm{V} = \hat{\mathrm{v}}(\omega)$ denote the envelope spectrum of the simulated fault, let U denote the envelope spectrum of the collected signal. Their Pearson's correlation coefficient is defined as the product of the covariance of the two variables divided by their standard deviations:

$$\rho_{\mathrm{U,V}} = \frac{\mathrm{cov(U,V)}}{\sigma_{\mathrm{U}}\sigma_{\mathrm{V}}} = \frac{\mathrm{E}[(\mathrm{U}-\mu_{\mathrm{U}})(\mathrm{V}-\mu_{\mathrm{V}})]}{\sigma_{\mathrm{U}}\sigma_{\mathrm{V}}} \tag{2.25}$$

where E[·] represents the expectation of the signal, and the sample Pearson's correlation coefficient can be expressed as:

$$\mathrm{r_{UV}} = \frac{\sum_{\mathrm{i=1}}^{\mathrm{n}}(\mathrm{U_i}-\bar{\mathrm{U}})(\mathrm{V_i}-\bar{\mathrm{V}})}{\sqrt{\sum_{\mathrm{i=1}}^{\mathrm{n}}(\mathrm{U_i}-\bar{\mathrm{U}})^2}\sqrt{\sum_{\mathrm{i=1}}^{\mathrm{n}}(\mathrm{U_i}-\bar{\mathrm{U}})^2}} \tag{2.26}$$

where $\bar{\mathrm{U}}$ represents the mean value. In order to better show the algorithm proposed in this paper, Fig.2.16 provides a flowchart.

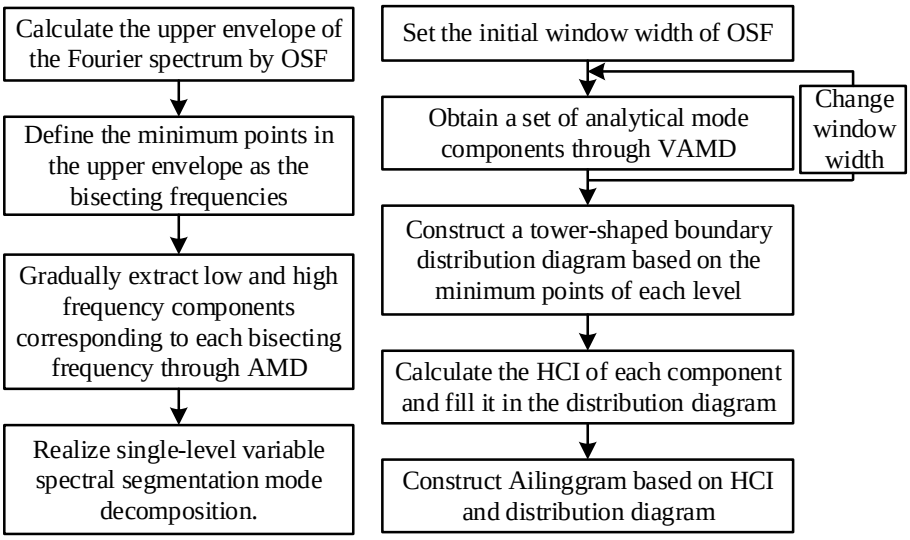

(a) VAMD (b) Ailinggram

Fig.2.16 The flowchart of Ailinggra

2.4 Verification

2.4.1 Simulation signal verification

A simulated signal of a bearing inner ring and outer ring compound fault is shown in Eq.2.27. The outer ring fault simulation signal is a set of periodic pulses. The inner ring fault simulated signal contains not only periodic pulses, but also amplitude modulation information and rotation frequency information, so it is more complicated.

$$\begin{cases} s_O(t) = \sum_{i=1}^{L} A_1 e^{-g_1 \times 2\pi f_{n1}^i t} \times \sin\left(2\pi f_{n1}^i t \times \sqrt{1-{g_1}^2}\right) \\ s_{I1}(t) = \sum_{i=1}^{M} A_2 e^{-g_2 \times 2\pi f_{n2}^i t} \times \sin\left(2\pi f_{n2}^i t \times \sqrt{1-{g_2}^2}\right) \\ s_{I2}(t) = \cos(2\pi f_r t) \\ s'_{I2}(t) = \begin{cases} s_{I2}(t), & s_{I2}(t) \geq 0 \\ 0, & s_{I2}(t) < 0 \end{cases} \\ s_{I3}(t) = A_3 \sqrt{\left(s'_{I2}(t)\right)^3} \\ u(t) = \begin{cases} 1, & t = 0.01n \\ 0, & others \end{cases} \\ s_I(t) = \left(s_{I3}(t) \times s'_{I2}(t) \times u(t)\right) * s_{I1}(t) \\ s(t) = s_O(t) + s_I(t) + \eta \end{cases} \tag{2.27}$$

where the amplitude A_1=1, A_2=0.5, A_3=3; the nature frequency is f_{n1}=1000 Hz, f_{n2}=3500 Hz; the damping coefficient $g_1 = 0.05$, $g_2 = 0.02$; $L = 17$, $M = 6$; rotation frequency f_r=12 Hz; $n = 1,2,3,\ldots,50$; η is noise with SNR $= -2$dB.

The model constructed by Eq.2.27 is shown in Fig.2.17, including the waveforms of the outer ring and inner ring, the Fourier spectrum of each component, and the envelope spectrum. Although the intensity of the noise is small, the time-domain waveform of the outer ring fault has been buried. Although the frequency domain waveform of the inner ring fault is buried, the frequency of rotation and the characteristic frequency of the inner ring fault can be found from the envelope spectrum. The variable multi-level spectral segmentation framework and the harmonic correlation index proposed in this chapter are used to process the signal, and the

characteristic frequencies of the outer ring and inner ring fault are input respectively.

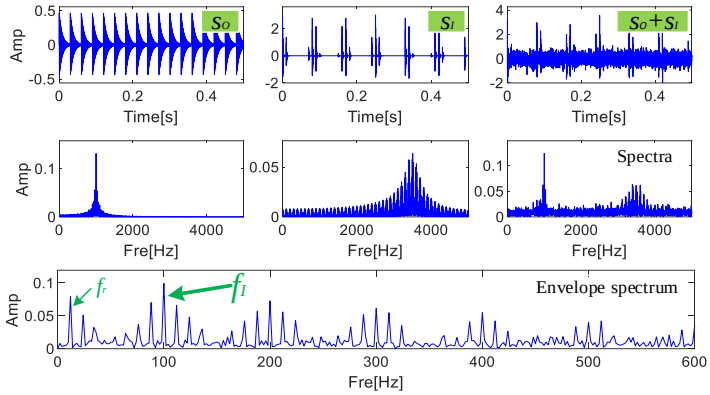

Fig.2.17 Composite fault data and spectra of outer and inner ring

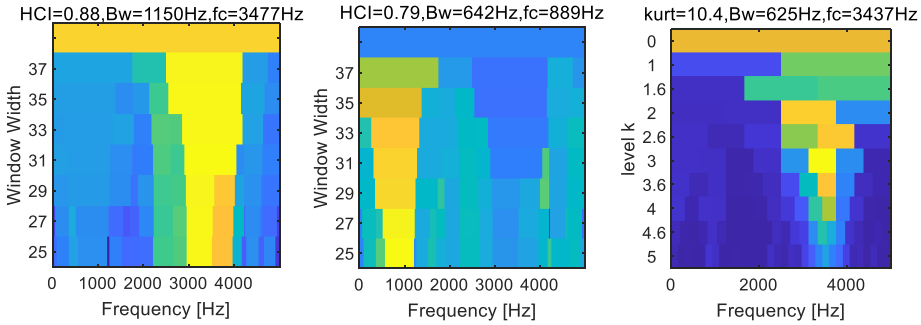

(a) Ailinggram-1 (b) Ailinggram-2 (c) Fast Kurtogram

Fig.2.18 Fault data processed by Ailinggram and Fast Kurtogram

Fig.2.18a-b shows the results of Ailinggram that extracts the faults of outer/inner ring. The frame will be divided into 7 levels, and the window width of OSF is increased from 25 to 37. The difference between them is the distribution of HCI. In Fig.2.18a, the large HCI is concentrated around 3477 Hz. The largest HCI is located at OSF=31, Ailinggram divided the spectrum into 11 frequency bands, and the 8th has the largest HCI. In Fig.2.18b, the large HCI is concentrated around 889 Hz, the largest HCI is located at OSF=25, Ailinggram divided the spectrum into 19 frequency bands, and the 4th has the largest HCI. The bandwidth is 642 Hz. Fig.2.18c shows the results obtained by the classic blind source Fast Kurtogram. The largest kurtosis located in the sixth component of level 3 with the center frequency of 3437 Hz, which is related to bearing inner ring fault. The bandwidth is 642 Hz.

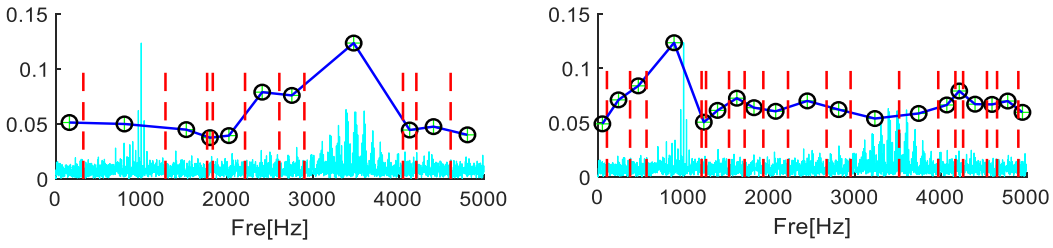

(a) Boundary distribution of Ailinggram-1-lv4 (b) Boundary distribution of Ailinggram-2-lv8

Fig.2.19 Boundaries and HCI distribution of Ailinggram

The boundaries and HCI distribution of Ailinggram can be seen in Fig.2.19. The frequency band with a center frequency of 3500 Hz in Fig.2.19a, 1000 Hz in Fig.2.19b has the largest HCI, while other frequency bands are much smaller than it. Reconstruct the time-domain waveform

of these frequency bands and calculate their envelope spectra (Fig.2.20). Although the amplitude of the pulses in the time-domain waveform is low, these pulses are obviously periodic. The envelope spectrum of the component (blue) and the simulated inner/outer ring fault (red) are in good agreement. The characteristic frequency and harmonics of the outer ring/inner ring of the bearing have a high degree of conformity with the simulation characteristics.

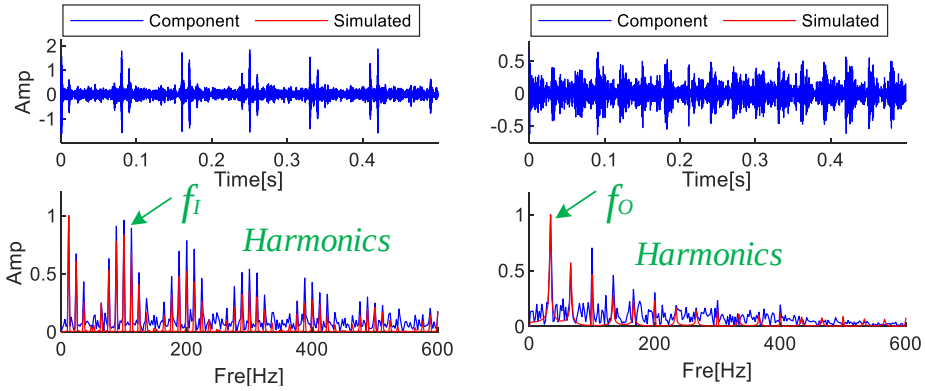

(a) Inner ring feature extraction (b) Outer ring feature extraction

Fig.2.20 Components with the largest HCIs and their envelope spectra

2.4.2 Bearing fault signal verification

2.4.2.1 Bearing inner ring fault data

This section uses the data collected by the bearing failure test bench of Mie University to verify the application of the proposed Ailinggram in fault diagnosis system of rotating machinery which is shown in Fig.2.21. The bearing type is NU204. The bearing inner ring has a width of 0.3 mm and a depth of 0.05 mm, the bearing outer ring has a width of 0.3 mm and a depth of 0.05 mm which is shown in Fig.2.21c.

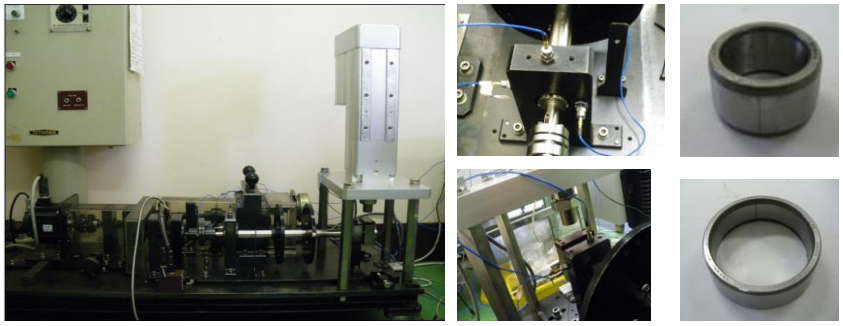

(a) Bearing test bench (b) Sensors (c) Ring fault

Fig.2.21 Bearing failure test bench

The bearing in operation bears a dynamic load of 0-300kg, and the speed of the motor is 1000 r/min. The inner ring fault characteristic frequency is $f_I = 110$ Hz, the period is $T_I = 0.0091$ s. Fig.2.22 shows the waveform and Fourier spectrum of the data. The pulses in the waveform have been buried by the strong environmental noise.

This section uses Ailinggram to design the multi-level spectral segmentation frame and filter the bearing inner ring fault information; the first component obtains the largest HCI. The center frequency is 2617 Hz. It can be found that although the window width is increased from 113 to 155, the width of the first frequency band is hardly divided, which is the characteristic of

the proposed Ailinggram. The large HCIs obtained are all located in this frequency band. Calculate the component and its Hilbert envelope spectrum, the results are shown in Fig.2.23.

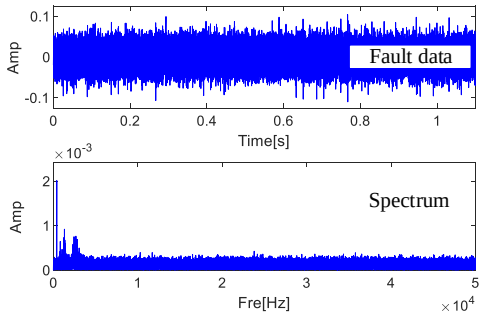

Fig.2.22 Collected bearing inner ring fault data

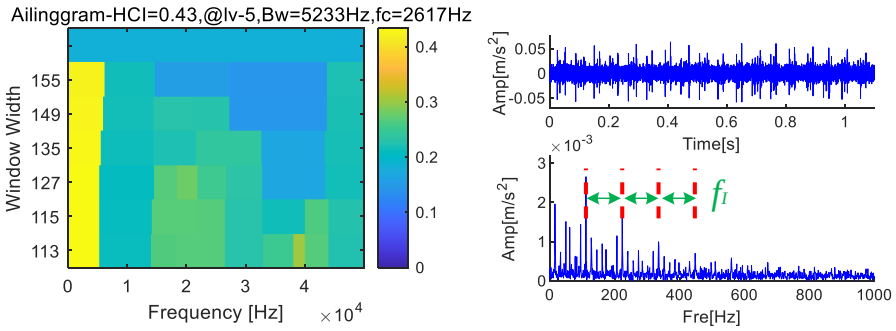

(a)Ailinggram (b) Component and its envelope spectrum

Fig.2.23 Inner ring fault extracted by Ailinggram and HCI distribution

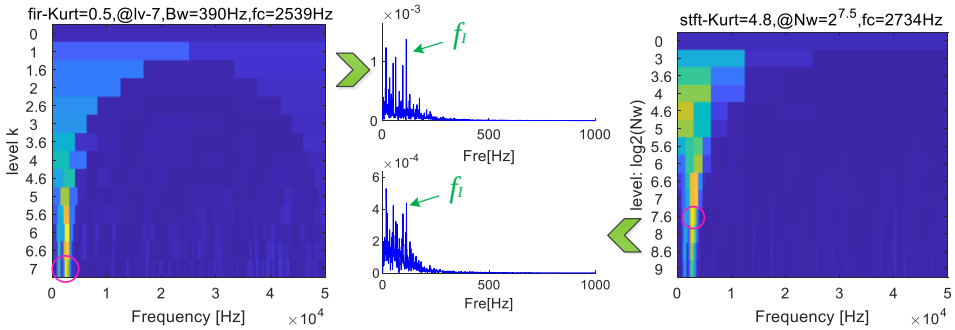

(a) FIR- Based Fast Kurtogram (b) Envelope spectrum (c) STFT-Based Fast Kurtogram

Fig.2.24 Inner ring fault extracted by Kurtogram

Although the amplitude of the waveform is reduced, many pulses with similar spacing appear. Compared with the original signal, the noise in this component is weakened and the impulse information is enhanced. In the Hilbert envelope spectrum, there are inner ring fault characteristic frequencies and their harmonics whose amplitude decreases in steps. There are sidebands near the harmonics, which is consistent with the characteristics of the bearing inner ring failure. The traditional Fast Kurtogram is used to process the signal to verify the advantages of Ailinggram. The FIR-based method obtained 7 levels of spectral segmentation groups, and the 7th component get the largest kurtosis in level 7. The STFT-based method obtained 9 levels of spectral segmentation groups, and the 8th frequency band of Level 7.6 get the largest kurtosis. The envelope spectra of these two components would be extracted and shown in Fig.2.24. Although the fault characteristic frequency can be found from them, the corresponding harmonic information cannot be found. Therefore, it is impossible to determine whether there is

a bearing inner ring fault here. Compared with the typical Fast Kurtogram, the proposed Ailinggram has better adaptability and diagnostic efficiency.

In this section, the calculation speeds of the traditional Fast Kurtogram, Autogram and the Ailinggram proposed in this chapter are tested and shown in Table 1. The traditional Fast Kurtogram still has the fastest speed, which can hardly be replaced. The calculation speed of Autogram is very slow. Although the Ailinggram proposed in this chapter is slower than Fast Kurtogram, it can still obtain results faster.

Table 1 Statistics of experimental results

	Fast Kurtogram	Autogram	Ailinggram
Time consuming	0.437s	297.145s	12.486s

2.4.2.2 Bearing outer ring fault data

When collecting the fault data of the outer ring, the bearing in operation bears a dynamic load of 0-300 kg, and the speed of the motor is 1500 r/min. The outer ring fault characteristic frequency is $f_O = 100$ Hz, the period is $T_O = 0.01$ s. Due to the strong noise, the time-domain waveform of the data collected in Fig.2.25 has little impulse information. Using Ailinggram to process the signal, the signal is decomposed into 6 levels. In all levels, the part less than 10,000 Hz has large HCI. Extract the level with the largest HCI and display the boundary distribution in Fig.2.26b. The Fourier spectrum is divided into 6 parts and the first frequency band with HCI=0.08 theoretically contains the most fault information. After reconstructing this frequency band, the noise in the is significantly reduced. The existence of the characteristic frequency and harmonics of bearing outer ring fault proves that the bearing outer ring fault exists in the signal. The Ailinggram can be applied to bearing fault diagnosis.

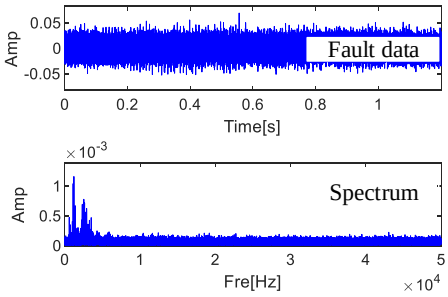

Fig.2.25 Bearing outer ring fault data and its Fourier spectrum

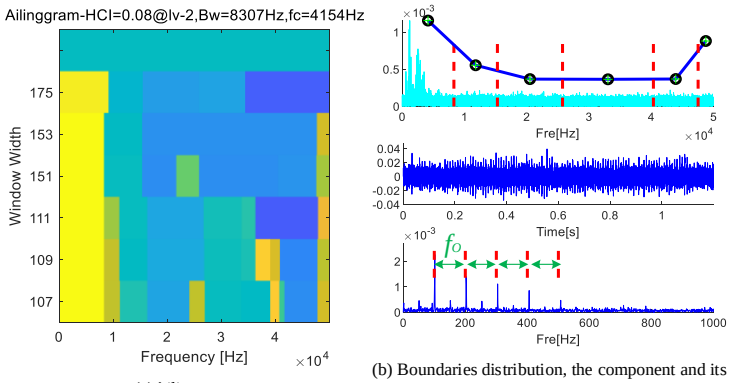

(a)Ailinggram

(b) Boundaries distribution, the component and its envelope spectrum

Fig.2.26 Outer ring fault extracted by Ailinggram and HCI distribution

Fast Kurtogram will get different results when processing this signal. The FIR-based

method obtained 7 levels and STFT-based method obtained 9 levels. Extracted the components with the largest kurtosis and shown the envelope spectra in Fig.2.27. Although the outer ring fault characteristic frequency can be found from it, the corresponding harmonic information cannot be found.

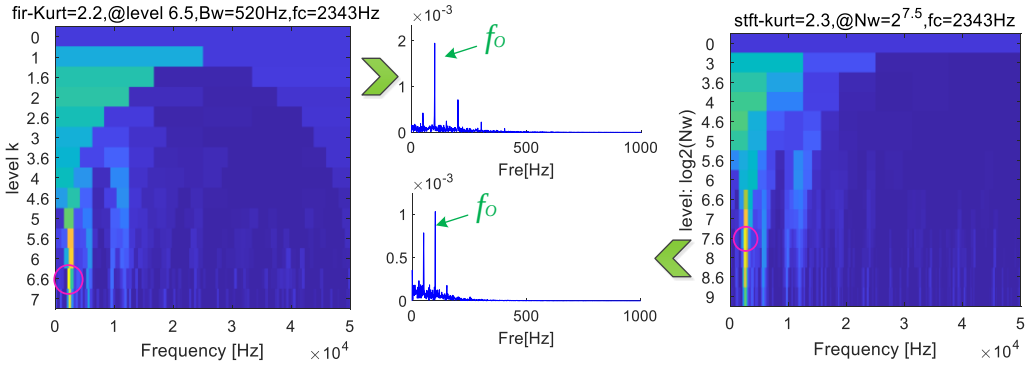

(a) FIR- Based Fast Kurtogram (b) Envelope spectrum (c) STFT-Based Fast Kurtogram

Fig.2.27 Outer ring fault extracted by Kurtogram

2.4.2.3 Bearing compound fault data

Shanghai Jiao Tong University provided data for this experiment. Fig.2.28 shows the bearing fault simulator and compound fault model. The motor rotation frequency is 30Hz, the motor rotation speed is 1800r/min, and the bearing model is 6200 deep groove ball bearing. The compound fault of the bearing includes the damage of the inner ring and the outer ring. There are three vibration acceleration sensors in the vertical, horizontal and axial directions of the faulty bearing. There is a fourth sensor in the vertical direction away from the faulty bearing.

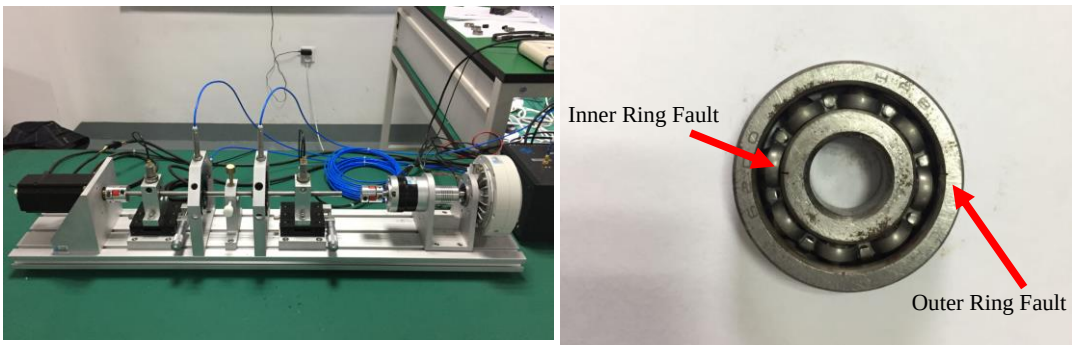

Fig.2.28 The bearing fault simulator

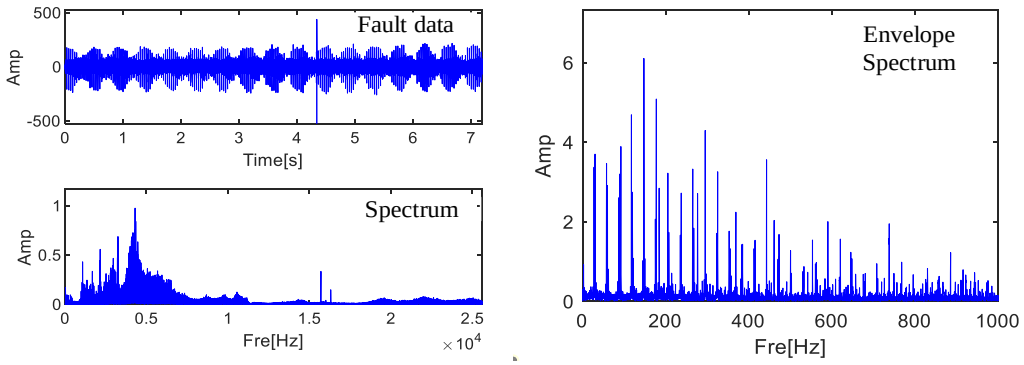

Fig.2.29 Collected signal, Fourier spectrum and envelope spectrum

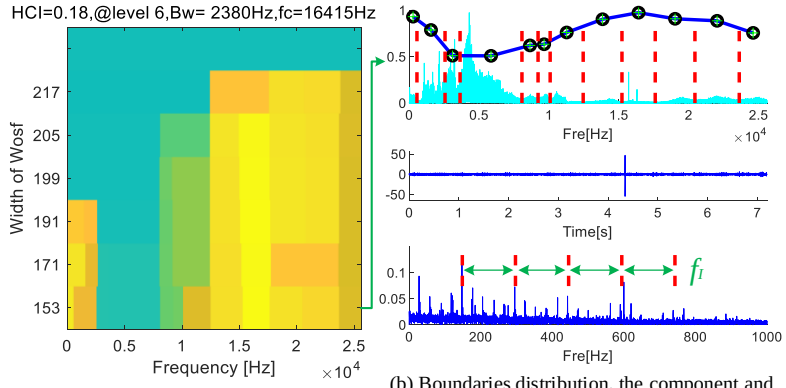

(a)Ailinggram-Inner ring fault extract

(b) Boundaries distribution, the component and its envelope spectrum

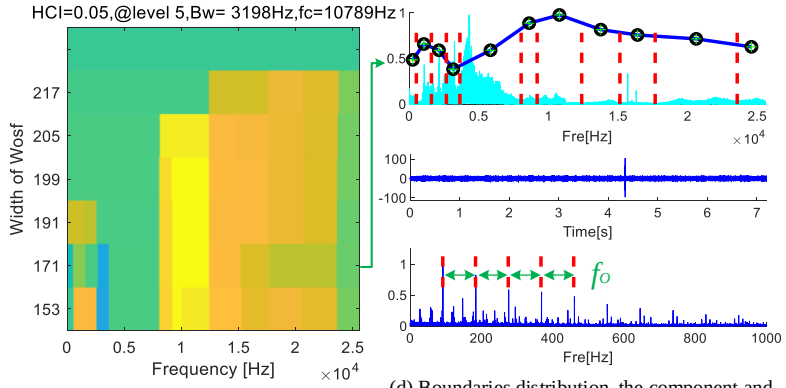

(c)Ailinggram-Outer ring fault extract

(d) Boundaries distribution, the component and its envelope spectrum

Fig.2.30 Inner and outer ring fault extracted by Ailinggram

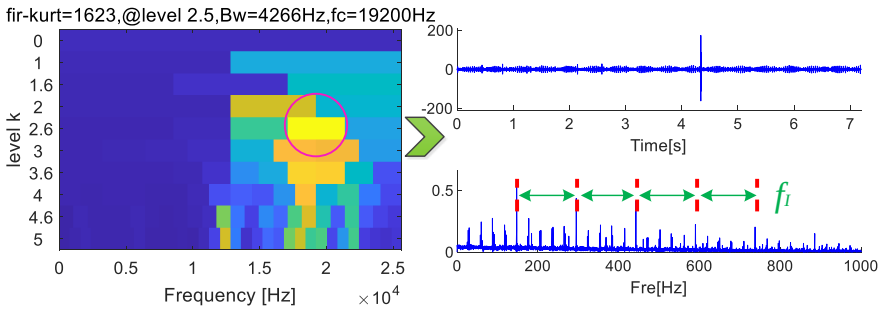

(a) FIR- Based Fast Kurtogram

(b) Component and its envelope spectrum

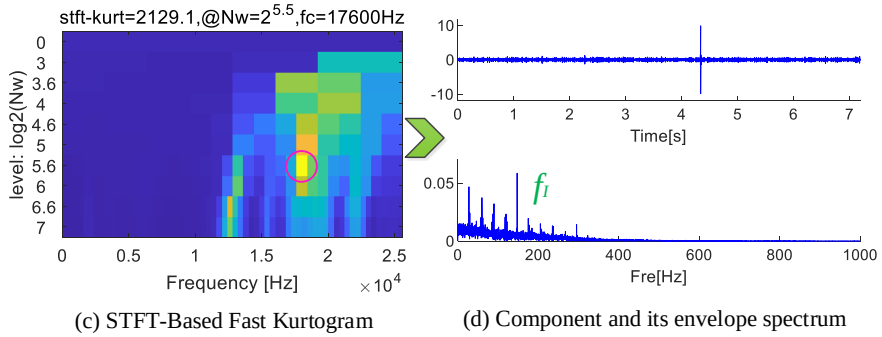

(c) STFT-Based Fast Kurtogram

(d) Component and its envelope spectrum

Fig.2.31 Inner and outer ring fault extracted by Kurtogram

The inner ring fault characteristic frequency is $f_i = 148.6$ Hz; the outer ring fault characteristic frequency is $f_o = 91.8$ Hz. The signal in Fig.2.29 has a single pulse, which may interfere with traditional indicators such as kurtosis. The Fourier spectrum is complex which proves that there are many types of information in the signal. The motor rotation frequency and

its multiples existed in the envelope spectrum, and it is necessary to continue processing the signal to diagnose the fault.

The results of Ailinggram extracting the bearing compound faults can be found in Fig.2.30. Large HCIs are distributed in different areas. When the bearing inner ring is faulty, the large HCI is distributed around 16000 Hz; when the bearing outer ring is faulty, the large HCI is distributed around 11000 Hz. The boundary and HCI distribution in the Level where the largest HCI is located in the two figures prove that the proposed method has higher adaptability. In the decomposition process, although the noise is suppressed, the single pulse has not been eliminated. The fault characteristics of the bearing inner and outer rings in the signal were successfully identified.

Fast Kurtogram will get different results when processing this signal. The FIR-based method obtained 5 levels and STFT-based method obtained 7 levels. Extracted the components with the largest kurtosis and shown the envelope spectra in Fig.2.31. FIR Based Fast Kurtogram can extract the fault of the bearing inner ring, but not the outer ring. STFT-Based Fast Kurtogram extracts information with a bandwidth of about 2130Hz near the center frequency of 17600Hz. Although the characteristic frequency of the inner ring fault can be found, the harmonics and the outer ring fault characteristic do not exist.

The above experiments verified that the proposed Ailinggram can successfully locate and extract the fault information of the inner ring and the outer ring The HCI is sensitive to pulse information with specific periodicity.

2.5 Conclusion

A novel framework of multi-level spectral segmentation (Ailinggram) were proposed. Ailinggram relies on OSF's window width variability and envelope estimation characteristics to achieve multi-level spectral segmentation, which replaces the manual selection of bisecting frequency and provides adaptability for AMD. The variable multi-level spectral segmentation framework increases the diversity of the center frequency and bandwidth, and suppresses the noise and interference in the reconstructed component. In order to filter the feature from the analytical modes of each level, this chapter proposes harmonic correlation index (HCI) for feature recognition and improves the usability of Ailinggram in the field of non-stationary signal processing and mechanical equipment fault diagnosis. The simulated and experimental signal proved that the proposed method is effective and can successfully extract the bearing faults.

Compared with Kurtogram, Ailinggram is more practical for rotating machinery. Although there is a slight difference between theory and practice, it does not affect the feature extraction process and the fault identification. Experiments have proved that when the frequency band with the largest HCI is extracted, the probability of fault information in the envelope spectrum is greater than that of spectral kurtosis.

Chapter 3
Multilevel spectral segmentation method based on optimized frequency slice wavelet transform and its application in bearing fault diagnosis under low speed and heavy load conditions [62]

3.1 Introduction

In this chapter, Fast Entrogram is proposed as a new method for separating components from the frequency domain and accurately filtering fault information. This method distinguishes the distribution of different components in each frequency band by the fluctuation characteristics of the spectral amplitude. We find that after the Fourier transform of the spectrum is intercepted, the reconstructed new sequence is directly related to the fluctuation characteristics of the spectral amplitude. The minima points of the sequence can be used to segment the spectrum and then separate different components. The frequency slice function would be used to extract components in each frequency band. By comparing with the finite impulse response filter, the component leakage energy extracted by the frequency slice function is less. In order to filter the periodic pulse information from all components, this section proposed correlation spectral negentropy (CSNE). The simulation results showed that the proposed Fast Entrogram method can effectively extract periodic pulses. The experimental signals verified that the method can be applied to fault diagnosis of bearing inner and outer rings.

3.2 Fast Kurtogram

3.2.1 A brief introduction to Fast Kurtogram

Fast Kurtogram has two forms of expression to represent the spectral kurtosis of the signal on the $(f, \Delta f)$ plane. Firstly, the center frequency f and the corresponding bandwidth Δf are defined in the plane. The Fast Kurtogram based on the 1/3-binary tree of filter-banks is shown in Fig.3.1a. The center frequency determines the position of the component to be extracted in the spectrum; the bandwidth determines the amount of information contained in the frequency band to be extracted.

In Fast Kurtogram based on FIR, dichotomy and trichotomy are nested. In Fig.3.1a, Level 0 is the spectrum of the original signal and he frequency band is $\Delta f \in [0, \pi/2]$. The red arrow indicates the dichotomy: the frequency band in Level 0 is divided into two parts, low frequency $[0, \pi/4]$ and high frequency $[\pi/4, \pi/2]$, and this part is named Level 1. The blue arrow indicates the trichotomy: Level 0 is divided into three parts: low frequency $[0, \pi/6]$, intermediate frequency $[\pi/6, \pi/3]$, and high frequency $[\pi/3, \pi/2]$. Then, the low frequency $[0, \pi/4]$ and high frequency $[\pi/4, \pi/2]$ in Level 1 can be decomposed into Level 2 by the same method, more and narrower frequency bands would be obtained. In Level n, the spectrum will be divided into 2^n parts by dichotomy and $3 \times 2^{n-1}$ parts by trichotomy. The corresponding bandwidth is $1/2^{n+1}$ and $1/(3 \times 2^n)$. The 1/3-binary tree of filter-banks is an optimization and supplement to the STFT-based Fast Kurtogram. The spectrum representation of STFT-based Fast Kurtogram is similar to that of dichotomy, as shown in Fig.3.1b.

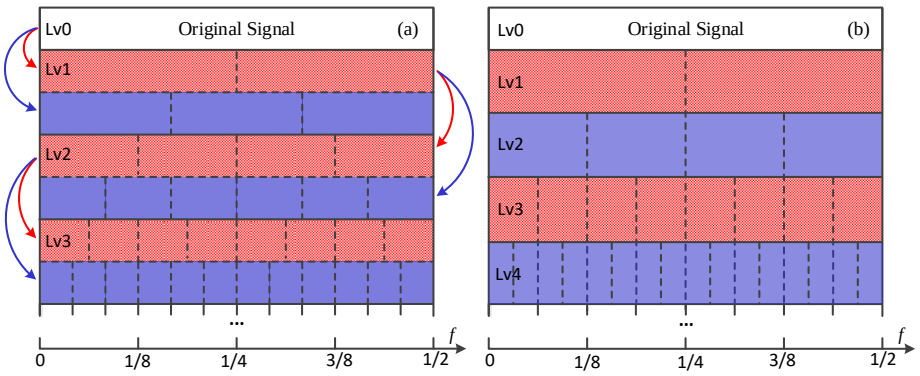

Fig.3.1 Frequency-band division methods: (a) FIR based Fast Kurtogram; (b) STFT based Fast Kurtogram

STFT and FIR are used to filter the signal. Take dichotomy as an example: two filters will be constructed: a low-pass filter $f_l(n)$ and a high-pass filter $f_h(n)$

$$\begin{cases} f_l(n) = f(n)e^{\frac{jn\pi}{4}} = f(n)\left[cos\left(\frac{n\pi}{4}\right) + jsin\left(\frac{n\pi}{4}\right)\right] \\ f_h(n) = f(n)e^{\frac{j3n\pi}{4}} = f(n)\left[cos\left(\frac{3n\pi}{4}\right) + jsin\left(\frac{3n\pi}{4}\right)\right] \end{cases} \tag{3.1}$$

where f(n) is a low pass FIR filter with a cutoff frequency $f_c = 1/8 + \varepsilon$.

Spectral kurtosis (SK) is defined as the energy-normalised fourth-order spectral cumulant which represents the peak of the probability density function

$$K = \frac{\langle |\{f_c, \Delta f\}|^4 \rangle}{\langle |\{f_c, \Delta f\}|^2 \rangle^2} - 2 \tag{3.2}$$

where $\{f_c, \Delta f\}$ denotes the frequency band with center frequency of f_c and bandwidth of Δf.

3.2.2 Shortcomings of Fast Kurtogram

This section introduces some details that Fast Kurtogram can be optimized:

a) Kurtogram is a framework and will be preset. The center frequency and bandwidth that may be obtained are related to the sampling frequency, so they are specific values which tends to cause the center frequency to be inappropriate or the bandwidth to be wide or narrow. The segmentation mode is fixed, so the obtained center frequency may offset when compared with the real situation. When the offset value is large, the effect of envelope demodulation will be affected. In addition, the obtained bandwidth is inversely proportional to the level of segmentation. For bearing fault signals, the narrow bandwidth may sometimes cause difficulties in diagnosis. This fixed mode brings limitations to Fast Kurtogram. When the center frequency is near $k/2^{n+1}$ or $k/(3 \times 2^n)$, it is difficult to find a suitable bandwidth. If a suitable bandwidth is selected preferentially, only a limited number of center frequencies are associated with it. For example, when the center frequency of the component to be extracted is exactly at $\pi/4$, it is only appropriate to obtain the frequency band $[\pi/6, \pi/3]$ after Level 0 is processed by trichotomy in FIR Based Fast Kurtogram. The width of this frequency band is fixed.

b) Energy leakage exists in FIR filters.

c) Kurtosis is very sensitive to random shocks, which makes the algorithm vulnerable to noise.

3.3 Proposed method of Fast Entrogram

When the rolling bearing in the rotating machine is damaged, the collected signal would contain fault information. Usually, these fault information will be concentrated in specific frequency bands on the spectrum. However, due to different bearing types and installation

positions in different equipment, the natural frequency will be different, so the center frequency representing the location of the fault information needs to be found. In this chapter, Fast Entrogram is proposed to find frequency bands that contain fault information in the spectrum. Since noise exists in both low and high frequencies, it is important to make the extracted component contain more fault information and less noise as the main task of the algorithm. For this reason, this chapter uses the trend spectrum----extracting the fluctuation trend of the spectrum from the Fourier transform function of the spectrum----to segment the spectrum, which can separate the parts where the amplitudes of the spectrum are concentrated from each other. Unlike Fast Kurtogram, which divides the spectrum evenly, this method performs division based on the characteristics of the amplitude fluctuation of the spectrum. The obtained results are related to the components in the signal. After successfully separating the spectrum into several frequency bands, this chapter uses the frequency slice function to extract each component. By comparing with the finite impulse response filter, the component leakage energy extracted by the frequency slice function is less. Considering the characteristics of periodic pulse signals, and in order to filter out the one that contains more fault information from many components, this chapter proposes correlation spectral negentropy. The specific steps are as follows:

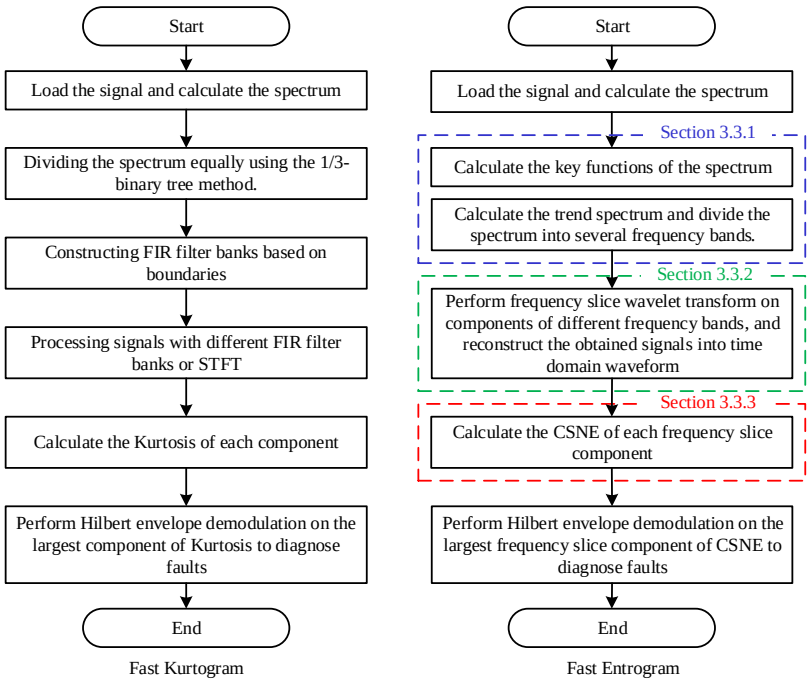

Fig.3.2 The flowcharts of Fast Kurtogram and Fast Entrogram.

Step 1: Collect the signal; calculate the Fourier transform of the spectrum to obtain the key function and set the initial interception length.

Step 2: According to the interception length, a part of the key function should be reconstructed to obtain the trend spectrum. Calculate the minimum points of the trend spectrum and divide the spectrum into several frequency bands.

Step 3: Use frequency slice function to extract each frequency band, a series of frequency slice components (FSCs) would be obtained.

Step 4: Increase the interception length and repeat steps 2 to 3 several times. Correlation spectral negentropy could be calculated for each group of FSCs.

Step 5: Arrange the frequency bands obtained under different interception lengths

according to the position of the center frequency of each frequency band. A new Entrogram can be obtained by identifying each band according to its bandwidth and the CSNE of the reconstructed component.

Fig.3.2 shows the flowchart of the above steps.

3.3.1 A novel spectral segmentation method

The collected signal often contains several kinds of unknown information, such as the characteristic information of the equipment during normal operation, the characteristic information of the faulty parts, and the environmental noise. If the equipment in normal operating conditions has not been severely disturbed by the outside world, its vibration signal may contain non-faulty modulation information and unavoidable environmental noise. In addition, when materials and equipment collide or random pulse signals generated by noisy environments may also be collected by sensors. When bearings, gears or other rotating parts in the equipment fail, collision may occur between balls and the inner or outer ring of the bearing, and may also occur between the normal gear and the damaged gear. The collision produces a pulse signal. Although the pulse signal will gradually weaken, repeated collisions at a steady speed will make the pulse signal periodic.

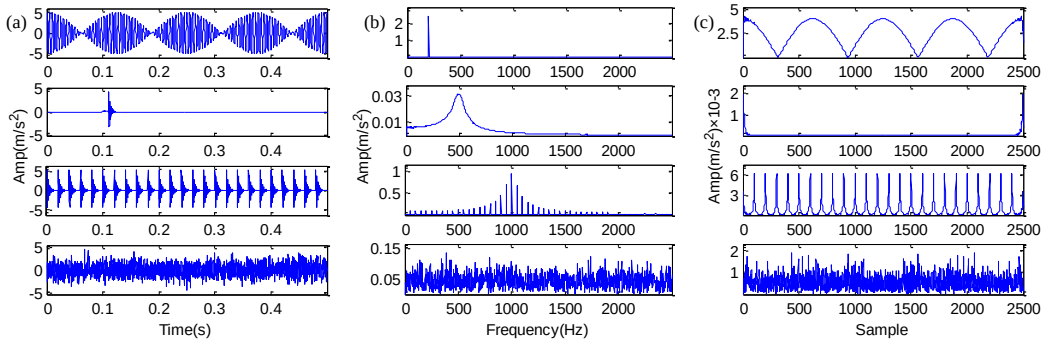

Fig.3.3 Four signals and their key functions: (a) signals; (b) spectra; (c) key functions.

Fig.3.3 simulates the modulation signal, pulse signal, periodic pulse signal and noise. These four signals have the same amplitude, which is $5\mathrm{m/s^2}$. If these four signals are superimposed into one complex signal, it is very difficult to separate them from the time domain. After calculating the Fourier spectrum of each signal separately, it can be found that although these signals are difficult to be distinguished in the time domain, they could be distinguished from the frequency domain because the center frequencies representing their vibration characteristics are located in different frequency bands. The characteristic frequency of the modulated signal in Fig.3.3 is lower than 300Hz, and the shape is two straight lines. The waveform of the pulse signal is an attenuated signal, but it is an arched curve in the frequency domain, and its energy is concentrated near the center frequency of 500 Hz. The center frequency of the periodic pulse signal is located at 1000 Hz, and there are lots of sidebands near the center frequency. Although the sidebands are spread all over the band, most of the energy is concentrated near the center frequency. In addition, noise can be found throughout the entire frequency band. If only the information of a certain frequency band is extracted, the noise in the obtained component will be small, but it is very difficult to separate all the noise. When the above signals are superimposed into one complex signal, the position of the original components in the spectra will not change. If the information between 750Hz and 1250Hz is extracted, the modulation signal, pulse signal and most noise will not be included, and most of the energy of the periodic pulse signal will be obtained. Based on this characteristic, this paper

proposed a spectral segmentation method based on the key function and trend spectrum to distinguish the components in the spectrum.

If the Fourier transform $\hat{f}(\omega)$ of the signal $f(t)$ exists, it can be calculated by the following formula:

$$\hat{f}(\omega) = \int_{-\infty}^{+\infty} f(t)\, e^{-i\omega t} dt \tag{3.3}$$

The spectrum $\left|\hat{f}(\omega)\right|$ does not contain imaginary parts, and it is discretized as a new signal. Let $g(n) = \left|\hat{f}(n)\right|$, $n = 0,2,3, \ldots, L-1$. L is the length of the new signal. It can be found that $g(n)$ is a discrete set of non-negative sequences. Calculate its discrete Fourier transform by Eq.3.4:

$$\hat{g}(u) = \sum_{n=0}^{L-1} g(n) e^{-i\frac{2\pi}{L}un} \tag{3.4}$$

Similar to the Fourier transform of the signal, $\hat{g}(u)$ contains real and imaginary parts. $|\hat{g}(u)|$ is called the key function in this paper. Fig.3.3c shows the relationship among key functions, signals and spectra. The key functions of the different signals are in different forms. If a part of $\hat{g}(u)$ is used to perform the inverse discrete Fourier transform, a new spectral function similar to the Fourier spectrum can be obtained. Using $\hat{g}_p(u)$ to represent the part of $\hat{g}(u)$, that can be used for calculation. The trend spectrum can be expressed as:

$$T(f) = \int_{-\infty}^{+\infty} \hat{g}_p(u) e^{i2\pi uf} du \tag{3.5}$$

where $T(f)$ is the trend spectrum.

Use Eq.3.3-3.5 to calculate the trend spectrum of the above three stationary signals. Compared with the Fourier spectrum, the amplitude of the trend spectrum is lower. The high-frequency part of the modulation signal is 200Hz, and the peak of the trend spectrum is also located at this position; the peak of the trend spectrum of the pulse signal coincides with the peak of its Fourier spectrum; so is the periodic pulse signal. In addition, the trend spectrum of the periodic pulse signal is similar to the upper envelope of its Fourier spectrum. It can be found that the trend spectrum contains information related to the fluctuation of the amplitude of the Fourier spectrum. The trend spectrum is also large where the amplitude of the spectrum is high. This regular phenomenon can be further used to segment different components in complex signals.

For a single signal, the trend spectrum has the above characteristics. For combined signals, the characteristics of the trend spectrum are worth exploring. Fig.3.4 shows that the center frequency of signal 1 is located at 200Hz, the center frequency of signal 2 is located at 500Hz, and the center frequency of signal 3 is located at 1000Hz. If signal 1 and signal 3 are combined, the Fourier spectrum and trend spectrum can be found in Fig.3.5a. The Fourier spectrum contains a lot of minimum points, but the trend spectrum has fewer minimum points. It is easy to separate the parts representing signal 1 and signal 3 from 260 Hz. If signal 2 and signal 3 are combined, the Fourier spectrum and trend spectrum can be found in Fig.3.5b. Signal 2 is a single pulse, and its energy is very small in the Fourier spectrum and hard to be found. The part of the trend spectrum that represents a single pulse can be detected. It is easy to separate the parts representing signal 2 and signal 3 from 750 Hz. If the three signals are combined, the Fourier spectrum and trend spectrum can be found in Fig.3.5c. These three components can be separated from 260 Hz and 750 Hz. The most critical part in the process of reconstructing the trend spectrum is how to determine the number of reconstruction points. Fig.3.6 shows the trend spectrum corresponding to different values. Small value means rough trend spectrum and fewer minimum points; the spectrum can be split into a small number of frequency bands. Large value

corresponds to complex trend spectrum and more minimum points and the spectrum will be split into a large number of frequency bands. This feature can be extended to the application.

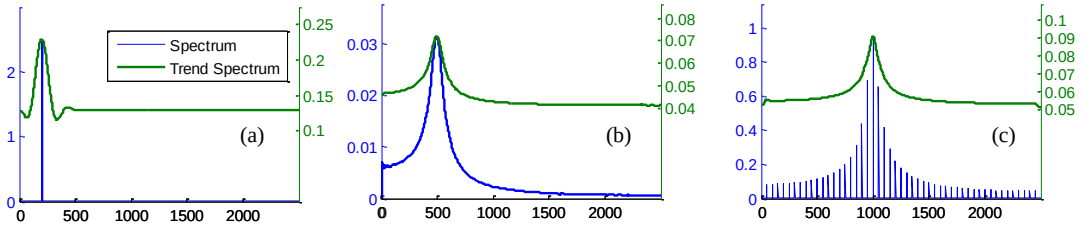

Fig.3.4 The relationship between Fourier spectrum and Trend spectrum: (a) signal 1: modulation signal; (b) signal 2: pulse signal; (c) signal 3: periodic pulse signal.

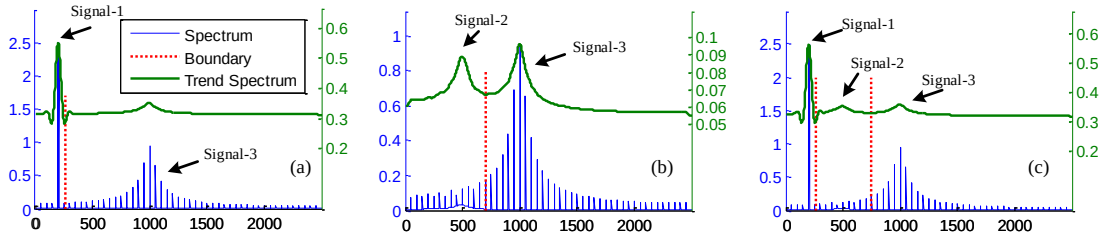

Fig.3.5 The Fourer spectrum and Trend spectrum of the superimposed signal: (a) Signal 1+3; (b) Signal 2+3; (c) Signal 1+2+3.

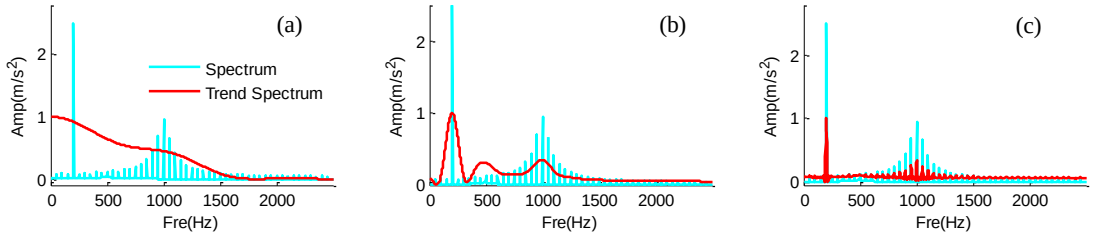

Fig.3.6 Trend spectrum corresponding to different values: (a) Value=5; (b) Value=25; (c) Value=300.

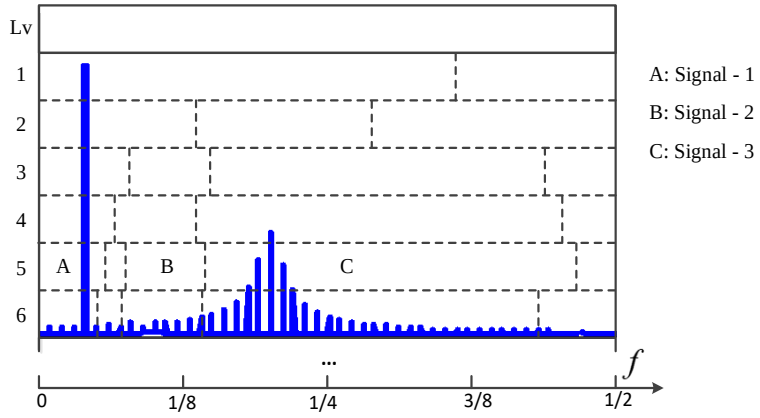

Fig.3.7 The proposed spectrum segmentation method.

If the initial value of the number of reconstruction points is 5, the trend spectrum has one minimum value, such as Lv1 in Fig.3.7. The spectrum is divided into two parts. When the value increases to 25, the number of boundaries increases to 4, as in Lv5. The spectrum is divided into five parts. It can be found that the number and position of the boundary will change as the value increases; sometimes the number of boundary does not change but the position changes. It should be noted that when the value is too large, too many boundaries will cause the frequency band to be narrow. Such segmentation results are meaningless and may increase the

computation time, so it is necessary to control the number of segmentation bands to be no more than 20.

3.3.2 Filtering characteristics of frequency slice wavelet transform

This section introduces the frequency slice function to fit the frequency band obtained in Section 3.3.1. The frequency slice wavelet transform can be expressed as:

$$W_f(t,\omega,\lambda,\sigma) = \frac{1}{2\pi}\lambda \int_{-\infty}^{+\infty} \hat{f}(u)\,\hat{p}^*\left(\frac{u-\omega}{\sigma}\right) e^{iut} du \tag{3.6}$$

where the scale factor $\sigma \neq 0$, t, ω, and u are the observation time, the observation frequency, and the evaluation frequency; λ can be set as a constant; $\hat{p}(\omega)$ is a frequency slice function (FSF); $*$ represents the conjugate. The time domain expression of Eq.3.6 is:

$$W_f(t,\omega,\sigma) = \sigma e^{i\omega t} \int_{-\infty}^{+\infty} f(\tau) e^{-i\omega t}\, p^*(\sigma(\tau - t)) d\tau \tag{3.7}$$

Yan explained that when $p(t)$ and $\hat{p}(\omega)$ take special values, FSWT can be transformed into traditional methods such as fast Fourier transform, short-time Fourier transform, and so on. It shows that FSWT is a generalized transformation method that can parse signals in the frequency domain.

Let $\sigma \propto \omega$ and $\kappa = \omega/\sigma$, then:

$$W_f(t,\omega,\kappa) = \frac{1}{2\pi}\int_{-\infty}^{+\infty} \hat{f}(u)\,\hat{p}^*\left(\kappa\frac{u-\omega}{\omega}\right) e^{iut} du \tag{3.8}$$

At this time, κ is defined as the relative resolution related to the observation frequency and the evaluation frequency. Eq.3.7 can be expressed as:

$$W_f(t,\omega,\kappa) = \frac{1}{\kappa}\omega e^{i\omega t} \int_{-\infty}^{+\infty} f(\tau) e^{-i\omega t}\, p^*\left(\frac{\omega(\tau-t)}{\kappa}\right) d\tau \tag{3.9}$$

Let $\Delta\omega_p$ be the frequency window width of the FSF. Consider the bandwidth-frequency ratio characteristic of the frequency slicing function, the frequency resolution of the FSF $\eta_p = \sigma\Delta\omega_p/\omega = \Delta\omega_p/\kappa$; the frequency resolution of the signal $\eta_p = \Delta\omega_s/\omega_s$. Usually, $\eta_p \ll 1$, so η_p can be adjusted by κ to achieve multi-resolution. If $\hat{p}(\omega)$ satisfies $\hat{p}(0) = 1$, the original signal or component can be reconstructed according to the following formula:

$$f(t) = \frac{1}{2\pi}\int_{-\infty}^{+\infty}\int_{-\infty}^{+\infty} W_f(\tau,\omega,\kappa)\, e^{i\omega(t-\tau)} d\tau d\omega \tag{3.10}$$

It can be seen from Eq.3.10 that the inverse frequency slice wavelet transform is only related to κ, and can be arbitrarily selected in the time-frequency interval of $f(t)$ to extract the required signal components. The following conditions need to be noted when constructing a frequency slicing function, but not all of them:

a) $\int_{-\infty}^{+\infty} |\hat{p}(\omega)|^2\, d\omega < \infty$; b) $\hat{p}(0) \neq 0$ or $\hat{p}(0) = 1$;

c) $\hat{p}(\pm\infty) = 0$; d) $|\hat{p}(\omega)| \leq |\hat{p}(0)|$ or $|p(t)| \leq |p(0)|$.

According to the above conditions, the following slicing function group can be constructed:

FSF-1: $\hat{p}(\omega) = e^{-\frac{1}{2}\omega^2}$, $p(t) = e^{-\frac{1}{2}t^2}$; FSF-2: $\hat{p}(\omega) = \frac{1}{1+\omega^2}$, $p(t) = e^{-|t|}$;

FSF-3: $\hat{p}(\omega) = e^{-|\omega|}$, $p(t) = \frac{1}{1+t^2}$; FSF-4: $\hat{p}(\omega) = \frac{\sin\omega}{\omega}$, $p(t) = \begin{cases} 1 & |t| \leq 1 \\ 0 & |t| > 1 \end{cases}$;

FSF-5: $\hat{p}(\omega) = \begin{cases} 1 & |\omega| \leq 1 \\ 0 & |\omega| > 1 \end{cases}$, $p(t) = \frac{\sin t}{t}$;

where, $\hat{p}(\omega) = \frac{1}{1+\omega^2}$ and $p(t) = e^{-|t|}$ are the most commonly used slicing functions. At this time, the frequency window width $\Delta\omega_p = \sqrt{2}/2$ of the frequency slicing function, the frequency resolution $\eta_p = \eta_s = 0.025$, and the scale $\kappa = 28.28$ can be calculated.

A simulation signal s_1 is constructed to demonstrate the filtering characteristics of the FSWT. The signal consists of periodic pulses s_{c1}, modulated signal s_{c2} and random noise:

$$\begin{cases} s_{c1} = A_1 e^{-g\times 2\pi f_n t} \times sin\left(2\pi f_n t \times \sqrt{1-g^2}\right) \\ s_{c2} = A_2\, sin(2\pi f_1 t)\, sin(2\pi f_2 t + sin(2\pi f_3 t)) + A_3\, cos(2\pi f_4 t)\, cos(2\pi f_1 t) \\ s_1 = s_{c1} + s_{c2} + \zeta \end{cases} \tag{3.11}$$

where, the nature frequency $f_n = 800$ Hz, damping coefficient $g = 0.07$, $f_1 = 50$ Hz, $f_2 = 3000$ Hz, $f_3 = 100$ Hz, $f_4 = 2$ Hz, amplitude $A_1 = 4$ m/s2, $A_2 = 2$ m/s2, $A_3 = 0.8$ m/s2, $\zeta =$ SNR$(-15$dB$)$. The waveform of the signal and its spectrum are shown in Fig.3.8.

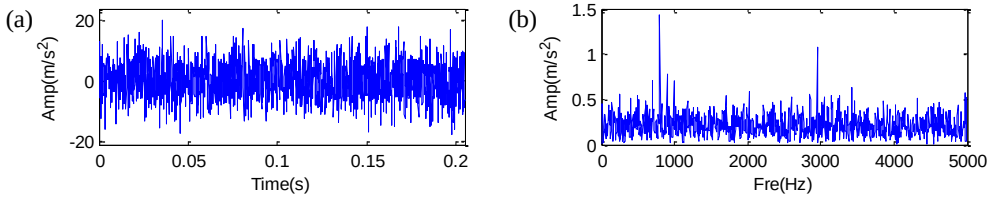

Fig.3.8 The first simulated signal: (a) waveform; (b) spectrum.

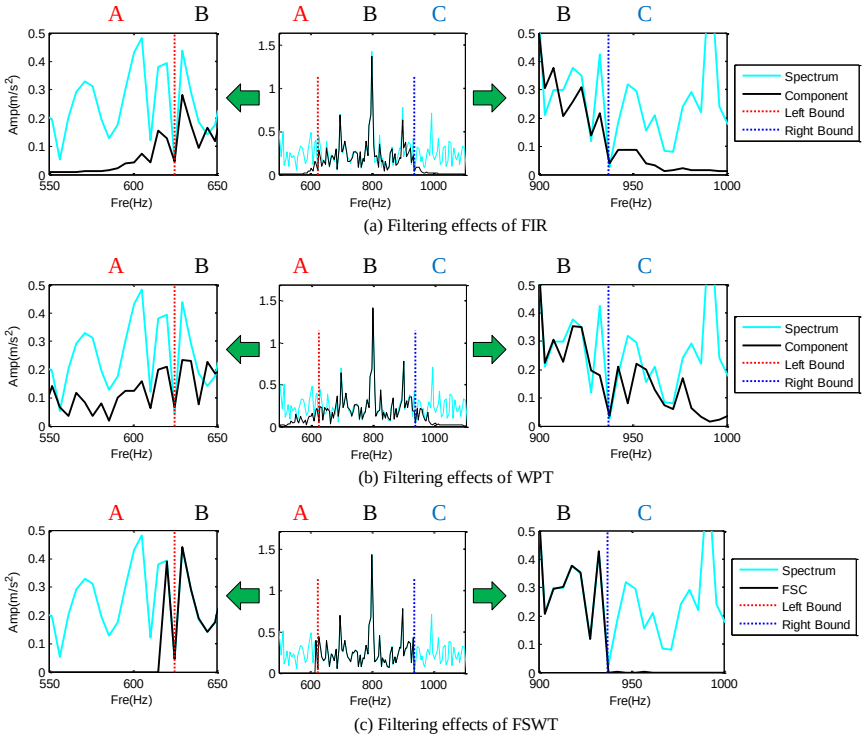

(a) Filtering effects of FIR

(b) Filtering effects of WPT

(c) Filtering effects of FSWT

Fig.3.9 Filtering effect of three methods.

Taking 800 Hz as the center frequency and the frequency band of 625 Hz to 937 Hz can be extracted for comparison. The filtering effects of FIR filter, wavelet packet transform (WPT) and FSWT are shown in Fig.3.9. Among them, Light blue are the spectra of the original signal; black are the results. Red is the left boundary and blue is the right. The boundaries divide the spectrum into three parts of A, B and C. The optimal filtering effect should be: The frequencies of bands A and C are infinitely close to zero; in band B, there is no energy loss in the spectrum. It can be found that the FIR filter and WPT have serious energy leakage in both A and C. After zooming in on the details around the boundaries, it can be noticed that FIR and WPT have a lot of energy leakage at A but FSWT has almost no leakage. The same situation exists at C. In addition, at B, the spectrum obtained by FIR and WPT differs from the spectrum of the original signal in this band, but FSWT is the same as the original signal. Therefore, in terms of filtering

the selected frequency band, FSWT is more helpful than FIR filters and WPT.

Since FSWT introduces the concept of frequency resolution, the most important research at present is time-frequency analysis. Calculate the time-frequency representation and then select the frequency band for extraction analysis. For signal s_2:

$$\begin{cases} s_{c1} = A_1 e^{-g\times 2\pi f_n t} \times \sin\left(2\pi f_n t \times \sqrt{1-g^2}\right) \\ s_{c2} = A_2 \sin(2\pi f_1 t)\sin(2\pi f_2 t + \sin(2\pi f_3 t)) \\ \quad +A_2 \sin(2\pi f_1 t)\sin(2\pi f_4 t + \sin(2\pi f_3 t)) \\ s_2 = s_{c1} + s_{c2} + \zeta \end{cases} \tag{3.12}$$

where the sampling frequency $f_s = 10000$ Hz, the natural frequency $f_n = 2500$ Hz, which means that the center frequency of the fault signal is located in the center of the frequency band. Damping coefficient $g = 0.07$, $f_1 = 50$ Hz, $f_2 = 1000$ Hz, $f_3 = 100$ Hz, $f_4 = 4000$ Hz, amplitude $A_1 = 4$ m/s2, $A_2 = 2$ m/s2, $\zeta = \mathrm{SNR}(-2\mathrm{dB})$.

The waveform of the signal and its spectrum are shown in Fig.3.10a.The component with the central frequency of 2500Hz carries fault information. The components of the central frequency at 1000Hz and 4000Hz include the side band, which belongs to the interference information. These three components were displayed in Fig.3.10b after being processed by FSWT. At present, the methods proposed by scholars can only determine the left and right boundaries of the three components by means of manual selection after observation, which would prone to large errors. The darkest part is ω_3, followed by ω_1. The band ω_2 has a large width. The results of manually extracting the above three frequency bands are shown in Fig.3.11. In fact, the second band is the part that should be extracted. Sectiong 3.3.1 provides a new idea for frequency band division, but how to select the frequency band containing the most periodic pulse information from each frequency band becomes the main problem to be solved.

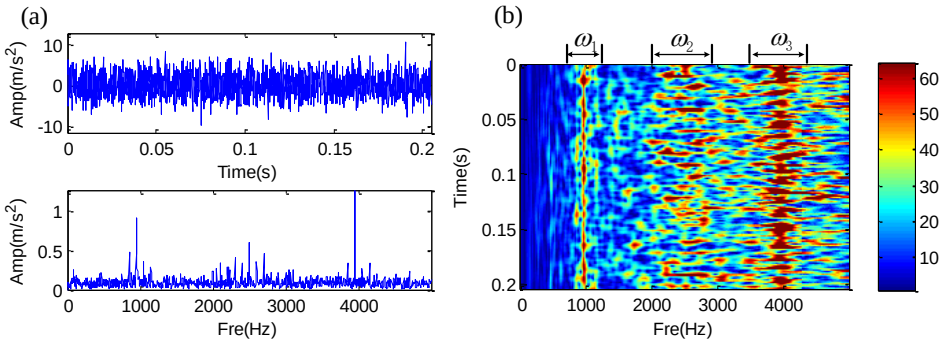

Fig.3.10 The second simulated signal: (a) the signal and its spectrum; (b) the time-frequency distribution

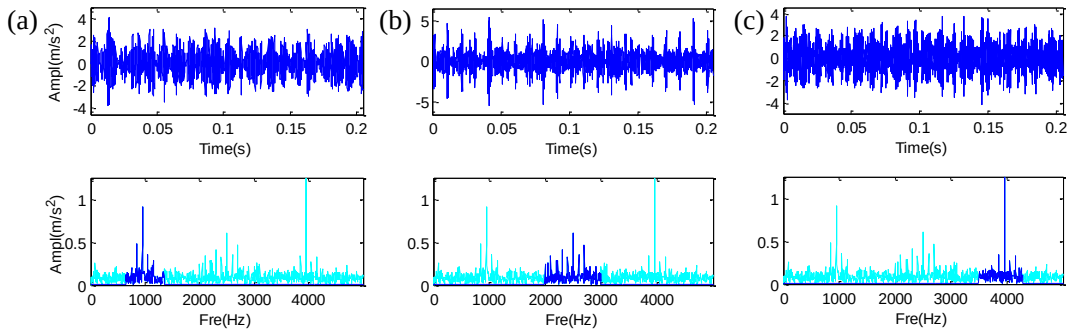

Fig.3.11 Components (a)ω_1, (b)ω_2 and (c)ω_3 obtained by the manual selection method.

3.3.3 Correlation Spectral Negentropy

Vibration signals of rotating machinery in normal operation can be considered as system balance. When parts of rotating equipment such as bearings or gears fail, pulses will appear in the vibration signals, and they would be periodic. The pulse generated by the previous impact must have similarity and correlation with the pulse generated by the next impact. Processing the signal in a correlated manner can amplify information with periodic characteristics. In addition, it is almost impossible to find similar components from the signal with random noise and accidental impact, and the autocorrelation is poor. The newly added impact information due to the fault will break the balance of the original system, and the entropy of the signal after correlation processing will be significantly reduced. Therefore, similar to kurtosis, entropy can be used to test for unbalanced disturbances in the system.

If the signal is $y(t)$, its spectrum $Y(f)$ can be calculated using the Fourier transform. The minimum point of the trend spectrum $T(f)$ divides the spectrum into M bands, $i = 1,2,3 \dots M$. The boundary of the ith band can be expressed as $[b_{i-1}; b_i]$. The center frequency in the interval $[b_{i-1}; b_i]$ is ω_i, and the bandwidth is $\Delta\omega_i$. Then the interval $[b_{i-1}; b_i]$ can also be expressed as $[\omega_i - \Delta\omega_i/2;\ \omega_i + \Delta\omega_i/2]$. Then the square envelope in the frequency band is $|Y(f; \omega_i, \Delta\omega_i)|^2$, and its time domain expression is $|y(t; \omega_i, \Delta\omega_i)|^2$.

The unbiased Autocorrelation is computed on the squared envelope of any one of the bands can be expressed as:

$$\hat{R}_{yy}(\tau; \omega, \Delta\omega) = \frac{1}{N-q}\sum_{i=1}^{M}\sum_{j=1}^{N-q}\left|y(t_j; \omega_i, \Delta\omega_i)\right|^2\left|y(t_j; \omega_i, \Delta\omega_i)\right|^2 \tag{3.13}$$

where $\tau = q/f_s$ is the delay factor, $q = 0,1,2,3 \dots N-1$.

The complex envelope of the optimized signal component in the frequency band $[\omega_i - \Delta\omega_i/2;\ \omega_i + \Delta\omega_i/2]$ is $\hat{R}_{YY}{}'(f; \omega, \Delta\omega)$. The instantaneous flow of energy returned by the squared envelope can be expressed as:

$$\varepsilon_R(f; \omega, \Delta\omega) = |\hat{R}_{YY}{}'(f; \omega, \Delta\omega)|^2 \tag{3.14}$$

The "Correlation spectral negentropy (CSNE)" can be defined as:

$$\Delta I_\varepsilon(\omega; \Delta\omega) = -H_\varepsilon(\omega; \Delta\omega) = -\left\{-\left\langle\frac{\varepsilon_R(f;\omega,\Delta\omega)^2}{\langle\varepsilon_R(f;\omega,\Delta\omega)^2\rangle} ln \frac{\varepsilon_R(f;\omega,\Delta\omega)^2}{\langle\varepsilon_R(f;\omega,\Delta\omega)^2\rangle}\right\rangle\right\} \tag{3.15}$$

Taking Eq.3.12 as an example, we already know that ω_1 and ω_3 are interference, ω_2 contains periodic pulse information, and the residual component is considered as noise. Kurtosis, Spectral Negentropy, Entropy, Sparsity and the CSNE proposed in this paper are used to calculate the above four components.

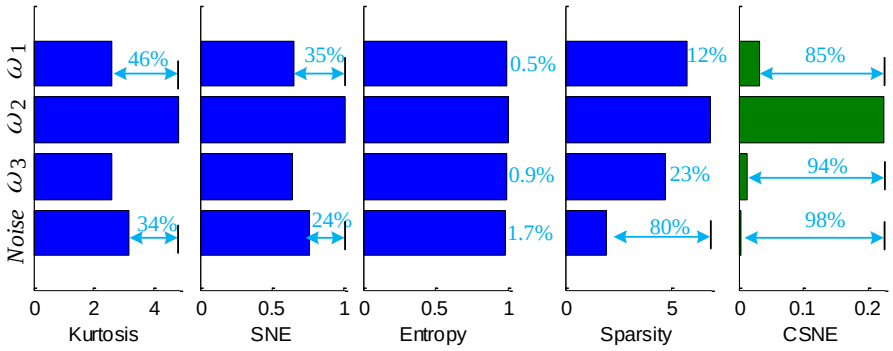

Fig.3.12 Sensitivity of each indicator to periodic pulses.

For the four components of ω_1, ω_2, ω_3 and noise, the indicate will have a large value if it is sensitive to it. Since ω_2 contains periodic pulse information, our desired indicator needs to be more sensitive to this signal than to other signals, and to be highly resistant to interference and

noise. It can be found from Fig.3.12 that Kurtosis and Spectral negentropy are sensitive to periodic pulses and resistant to interference, but will be interfered by noise. Entropy suffers from greater interference and is less resistant to noise. Although Sparsity is highly resistant to noise, it is susceptible to interference. The sensitivity of the CSNE processing results to the four signals is significantly different from the first four methods. CSNE is sensitive to periodic impact information and has strong anti-interference and anti-noise capabilities.

3.4 Verification

3.4.1 Simulation signal verification

3.4.1.1 Case study 1

A simulation signal s_2 is constructed to simulate faults with periodic pulses. The signal consists of periodic pulses s_{c1}, modulated signal s_{c2} and random noise:

$$\begin{cases} s_{c1} = A_1 e^{-g\times 2\pi f_n t} \times \sin\left(2\pi f_n t \times \sqrt{1-g^2}\right) \\ s_{c2} = A_2 \sin(2\pi f_1 t)\sin(2\pi f_2 t + \sin(2\pi f_3 t)) \\ \qquad +A_3 \cos(2\pi f_4 t)\cos(2\pi f_1 t) \\ s_2 = s_{c1} + s_{c2} + \zeta \end{cases} \tag{3.16}$$

where, the nature frequency $f_n = 800$ Hz, damping coefficient $g = 0.07$, $f_1 = 50$ Hz, $f_2 = 3000$ Hz, $f_3 = 100$ Hz, $f_4 = 2$ Hz, amplitude $A_1 = 4$ m/s2, $A_2 = 2$ m/s2, $A_3 = 0.8$ m/s2, $\zeta =$ SNR$(-8$ dB$)$. The repeated cycle is $T = 0.01$ s. The characteristic frequency is $f_q = 100$ Hz.

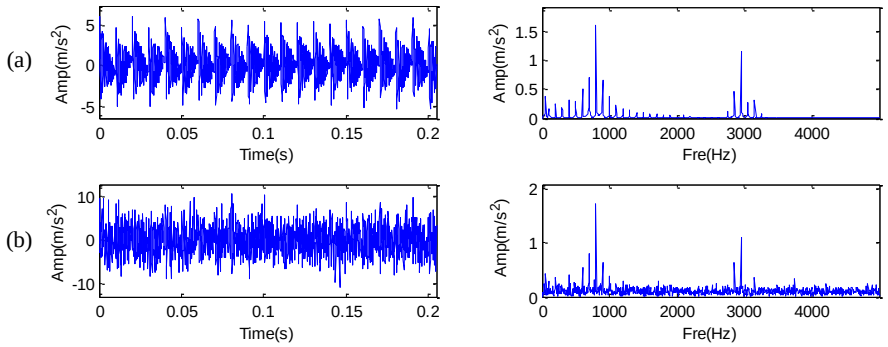

Fig.3.13 (a) The signal without noise and its spectrum; (b) the signal with noise and its spectrum

The waveform of the signal and its spectrum are shown in Fig.3.13a. The periodic pulse characteristics in the waveform are obvious. Fig.3.13b is the simulated signal and its spectrum after noise is added. The periodic pulse characteristics in the waveform are masked by noise. The component with the natural frequency of 800 Hz is periodic pulse information; the component with the natural frequency of 3000 Hz is interference information. We need to adaptively separate the component with the center frequency of 800Hz from the other components in the spectrum.

In view of the tediousness and non-adaptability of the original manual extraction method, this paper uses the adaptive traditional Fast Kurtogram to compare with the proposed Fast Entrogram. First, the signal is processed using Fast Entrogram. As the number of reconstruction points increases, the signal is divided into five levels, and the spectrum is divided into several frequency bands in each level. The color in the frequency band represents the value of CSNE. When the color in the frequency band is red, it means that there is more periodic pulse information in this band. When the color in the band is blue, it means that there are many other

components in the band. It can be found from Fig.3.14a that the largest CSNE component in all frequency bands is located in Level 5(A). Details of the spectral segmentation and trend spectrum of this Level are shown in Fig.3.14b. In this Level, the 10 boundaries at the minimum of the trend spectrum divide the spectrum into 11 parts. The CSNE of the second band is the largest, with the center frequency of 793Hz, which is very close to 800Hz; the bandwidth is 679Hz, CSNE = 0.52. The method in Section 3.3.2 can be used to extract the component in the second frequency band (Fig.3.14c) and calculate its envelope spectrum (Fig.3.14d). The components contain pulses, and these pulses are periodic. The characteristic frequency of 100 Hz and its harmonics appear in the envelope spectrum. Therefore, the method proposed in this chapter is effective in extracting periodic pulse information.

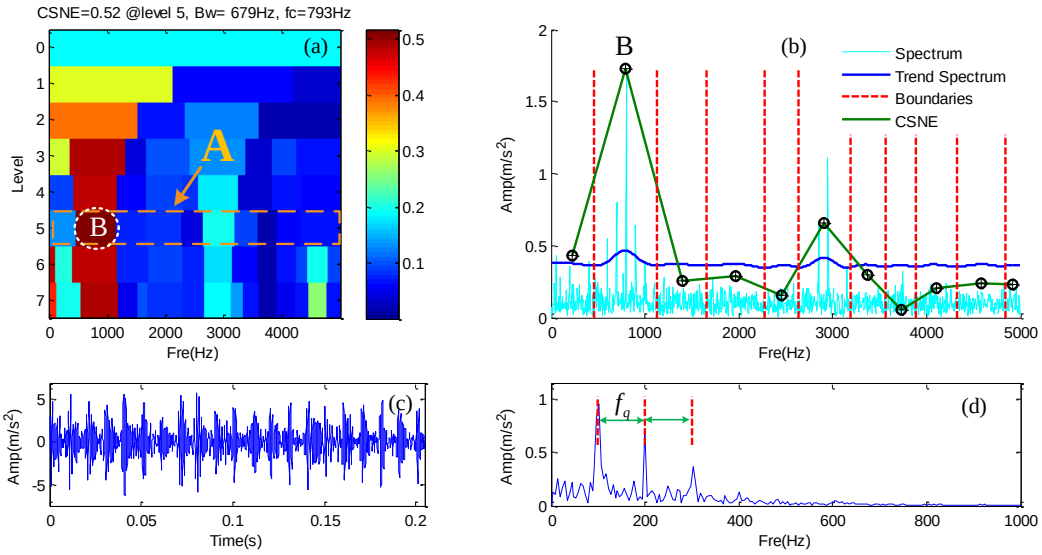

Fig.3.14 Results decomposed by (a) Fast Entrogram; (b) Trend spectrum, boundaries and CSNE of Level 5; (c) Component B with maximum CSNE; (d) the envelope spectrum of Component B.

Then, this signal is processed by Fast Kurtogram based on FIR filter (Fig.3.15a), and the spectrum is divided into 4 levels. The component of maximum kurtosis is located in the last frequency band in Level 4, and its center frequency is 4843Hz, which is different from 800Hz. Although this frequency band contains a small amount of periodic pulse information, it also contains a lot of noise, so it is not enough to extract fault features. This is not the frequency band that needs to be extracted. At last, process the signal by Fast Kurtogram based on STFT (Fig.3.15b) and the spectrum is divided into 6 levels. The component of maximum kurtosis is at Level 6. The center frequency is 3437Hz. The periodic pulse information contained in this band is not enough for feature extraction.

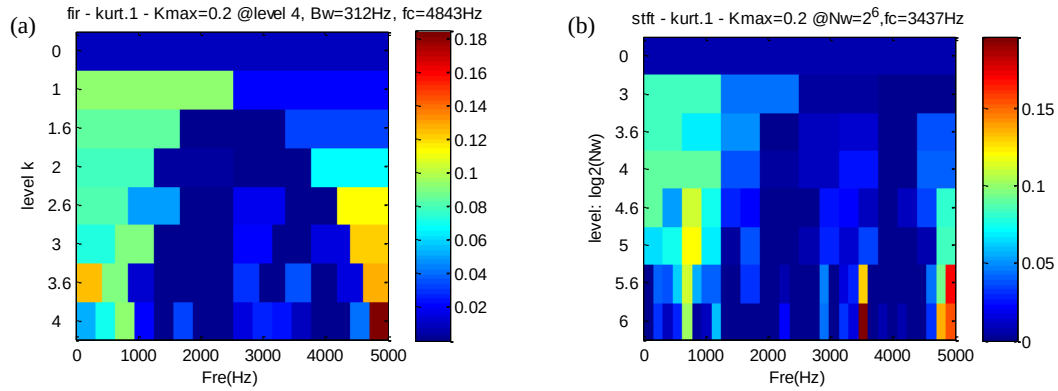

Fig.3.15 The results decomposed by: (a) FIR based Fast Kurtogram; (b) STFT based Fast Kurtogram.

3.4.1.2 Case study 2

This section explores the effect of bandwidth on extraction results. Construct a periodic pulse signal without noise:

$$s_c = Ae^{-g\times 2\pi f_n t} \times sin\left(2\pi f_n t \times \sqrt{1-g^2}\right) \tag{3.17}$$

where the natural frequency $f_n = 2500$ Hz. Damping coefficient $g = 0.07$, amplitude $A = 4$ m/s^2. After calculation, the width of the sideband is 100Hz, characteristic frequency $f_q = 100$ Hz.

The spectrum is shown in Fig.16. In the spectrum, the periodic pulse information is unevenly distributed throughout the frequency band and most of the energy is concentrated near the center frequency. The signals collected in the application often contain interference and noise, selecting more frequency bands near the center frequency for extraction can obtain more effective information. This experiment set three sets of boundaries. B1 = 200 Hz contains only two sidebands, B2 = 600Hz contains 6 sidebands and B3 = 1400 Hz contains 14 sidebands. The signals within the three groups of boundaries are extracted and their envelope spectra are calculated. Fig.3.16b shows their envelope spectra. When the frequency band contains only 2 sidebands, there is the characteristic frequency in the envelope spectrum without harmonics; when the frequency band contains 6 sidebands, there is characteristic frequency and a few harmonics in the envelope spectrum; when the frequency band contains 14 sidebands, there is characteristic frequency and a large number of harmonics in the envelope spectrum. For the above fault simulation signal, the fault information contained in the two sidebands near the center frequency is small; the information in the 6 sidebands is easily masked by noise. For the signal shown in Fig.3.16, most of the signal's information is already available in the 14 sidebands, so 1400 Hz can be regarded as a reasonable bandwidth in this signal.

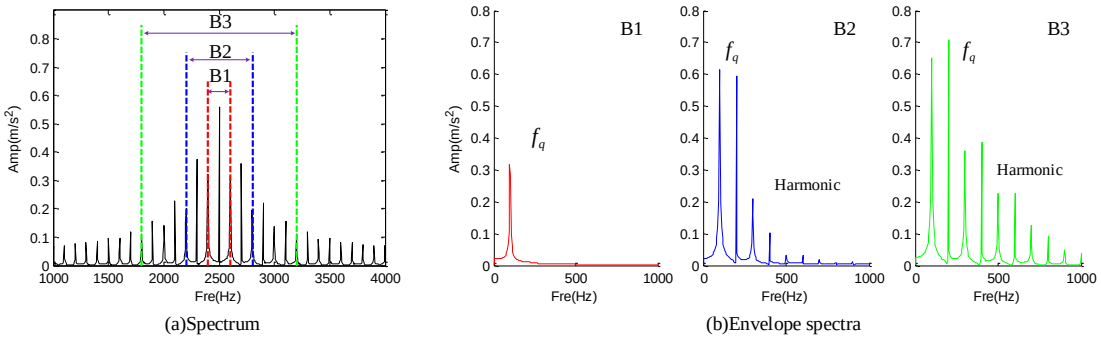

(a)Spectrum (b)Envelope spectra

Fig.3.16. The spectrum of the simulated signal and the envelope spectrum of each component.

Subsequently, two interference signals are added to the simulation signal, the center frequency of the first interference signal is 1000 Hz, and the center frequency of the second interference signal is 4000 Hz, as shown in Eq.3.12 and Fig.3.10a. The spectra of the constructed interference signals are similar to the original signal, and they also contain sidebands. We need to find and extract periodic pulse information with a center frequency of 2500 Hz and a bandwidth of about 1400 Hz from the new signal. First, the new signal is processed using the Fast Entrogram method proposed in this paper, and the results are shown in Fig.3.17. The process of drawing Entrogram is to increase the number of reconstruction points in the obtained trend spectrum. As the level increases, the number of reconstruction points increases to 45, and the spectrum is divided into 7 levels. The number of boundaries is positively related to the number of reconstruction points, and the bandwidth becomes narrower as the boundary increases. Narrow bandwidth may interfere with the accuracy of the diagnosis.

At Level 5-7, the information around the center frequency of 2500 is divided into several parts, but at Level 2-4, the information is complete and the largest CSNE appears at Level 3. The center frequency of this band is 2514 Hz, which is only 0.56% different from expected. The bandwidth is 1240Hz and includes 12 sidebands. In order to show the relationship between the spectrum and the selected frequency band, the spectrum is placed in Level 1 of Fast Entrogram. The information in this frequency band is extracted, and its waveform and envelope spectrum are shown in Fig.3.17c. Periodic pulses can be easily observed from the waveform of this component. Although there is still a small amount of noise that has not been removed, it does not affect the peak value of the pulses. In addition, the characteristic frequency of 100 Hz and its harmonics appear in the envelope spectrum, which proves that the above conclusion is correct. Therefore, the proposed Fast Entrogram method can extract periodic pulse information in signals containing interference information and noise.

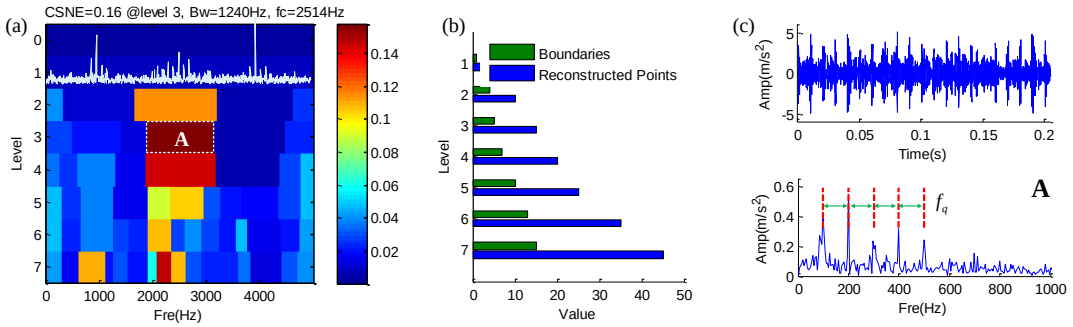

Fig.3.17 Result decomposed by (a) Fast Entrogram; (b) Boundaries corresponding to reconstructed points; (c) Component with maximum CSNE and its envelope spectrum.

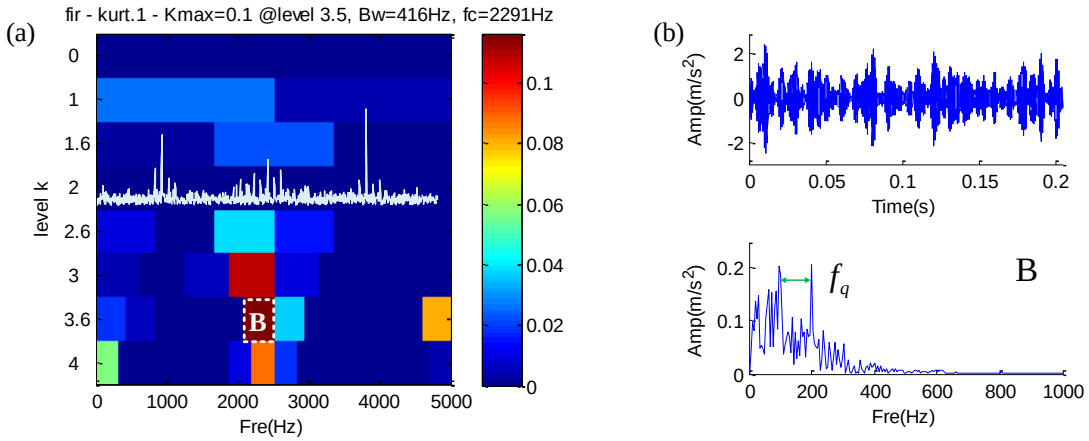

Fig.3.18 Result decomposed by (a) Fast Kurtogram; (b) Component with maximum Kurtosis and its envelope spectrum.

If Fast Kurtogram is used to process this signal, the result is shown in Fig.3.18. The center frequency is 2500 Hz which is located at the center of the Kurtogram. In all division methods, only the center frequency of the second frequency band of Level 1.6 is 2500Hz, and its bandwidth is 1667Hz. The calculation results show that Kurtosis in this band is very small. The largest Kurtosis is at Level 3.6. Its center frequency is 2291Hz and its bandwidth is 416Hz. Although the bandwidth is close to the optimal bandwidth, the noise in the signal has a huge impact on Kurtosis, which leads to deviations in the selection of the frequency band. Extract the component with the center frequency of 2291Hz and calculate the envelope spectrum. Although there are pulses in the waveform of this component in Fig.3.18b, the periodicity of these pulses is difficult to calculate. The characteristic frequency and its double frequency appear in the

envelope spectrum, but the amplitude is low. A bandwidth of 416Hz can only contain three sidebands. The noise contained in such a narrow bandwidth easily masks effective information.

The center frequency offset rate (r_o) and the bandwidth error rate (r_e) are used to demonstrate the accuracy of the two algorithms. After the device is successfully assembled, its natural frequency does not change when a fault occurs and periodic pulse information is generated. The center frequency offset ratio is the ratio of the center frequency offset natural frequency of the extracted band. When r_o is positive, the center frequency is shifted to the right; when r_o is negative, the center frequency is biased to the left:

$$r_o = \frac{f_c - f_n}{f_n} \tag{3.18}$$

The bandwidth error rate is the difference rate between the extracted bandwidth B_w and the optimal bandwidth. Its calculation formula is as follows:

$$r_e = \frac{|B_w - B_o|}{B_o} \tag{3.19}$$

Calculate the center frequency offset rate and bandwidth error rate of Fast Entrogram and Fast Kurtogram, respectively, as shown in Fig.3.19.

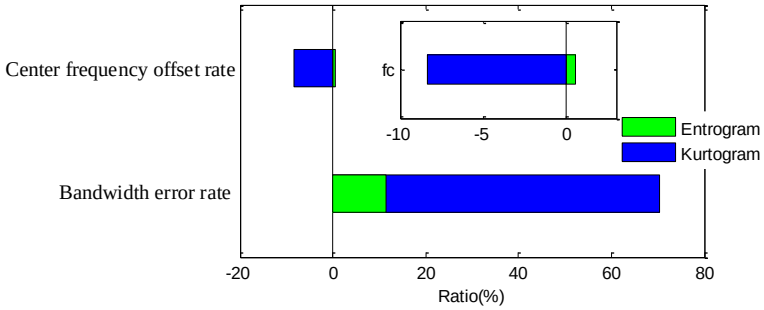

Fig.3.19 Center frequency offset rate and bandwidth error rate

The center frequency of Fast Kurtogram is shifted to the left by 8.36% and the offset rate is slightly larger. The center frequency of Fast Entrogram deviates to the right by 0.56% and the offset rate is small. The advantages of the method proposed in this paper can also be seen in a partially enlarged view. The center frequency obtained by Fast Entrogram is more accurate than Fast Kurtogram. The bandwidth obtained by Fast Entrogram is 1240 Hz and can contain 12 sidebands, so the characteristic frequency and harmonics can be found in the envelope spectrum. The Fast Kurtogram obtained a bandwidth of 416 Hz and can only contain 4 sidebands. The envelope spectrum calculated by extracting only 4 sidebands will contain fewer harmonics than the 12 sidebands. Therefore there is no other harmonics in the envelope spectrum of Fast Kurtogram. At the same time, the bandwidth error rate of Fast Entrogram is 11.43%, and that of Fast Kurtogram is 70.29%. It can be proved that the center frequency and bandwidth obtained by Fast Entrogram contain more periodic pulse information than Fast Kurtogram. This kind of characteristic can play a big advantage in the fault diagnosis of the inner and outer rings of the bearing. For the method of using wavelet transform to separate the signal, there are some challenges in completely extracting the frequency band with the center frequency near $k/2^{n+1}$. The center frequency of the periodic pulse information of the simulated signal used in this section is located in the center of the spectrum (2500 Hz). Autogram uses Maximal overlap discrete wavelet packet transform to process the signal. Similar to Fast Kurtogram, Autogram also needs to manually select the level to be obtained. If we choose Level 5, the result can be found in Fig.3.20a. The component with the largest unbiased autocorrelation is the fourth component of Level 3. The center frequency is 2187.5 Hz, which has a certain error

with 2500 Hz. There is no case in Autogram's framework where the center frequency is 2500 Hz, which is inevitable. Extract component A, the waveform and spectrum are shown in Fig.3.20b. The light blue line is the spectrum of the original signal, and the dark blue line is the spectrum of component A. It is not difficult to find that the energy of component A leaks between 2500Hz and 3000Hz, which is also the deficiency of general wavelet transform. If we choose the decomposition level to be 7, the Autogram in Fig.3.20c will be obtained. The largest component of unbiased autocorrelation is located at Level 7, with a center frequency of 1738 Hz and a bandwidth of 39 Hz. This is the disadvantage of the traditional method: it is sometimes inconvenient to manually select the number of decomposed levels.

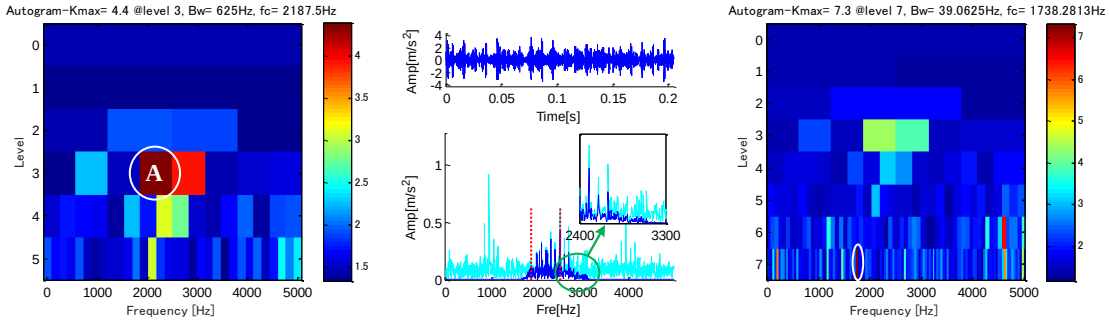

(a) Autogram (b) Component A and its spectrum (c) Autogram

Fig.3.20 Result decomposed by (a) Autogram; (b) Component with maximum Kurtosis and its envelope spectrum; (c) Autogram with lv-7

3.4.2 Bearing fault signal verification

The vibration signal experimental data used in this section comes from Mie University. The bearing fault simulator is shown in Fig.3.21. The drive end and the bearing part are connected with a pulley. The part where the bearing is installed is very heavy and also bears a load of about 500 kg. The rotation speed of the shaft is 70 rpm. At the same time, this experiment uses rusty chains to add noise to the system. During the experiment, the vibration acceleration sensor, acoustic emission sensor, and Microphone collected signals synchronously. This chapter uses the experimental field signal collected by vibration acceleration sensors. The sampling frequency of is 100 kHz, the acquisition time is about 20 s.

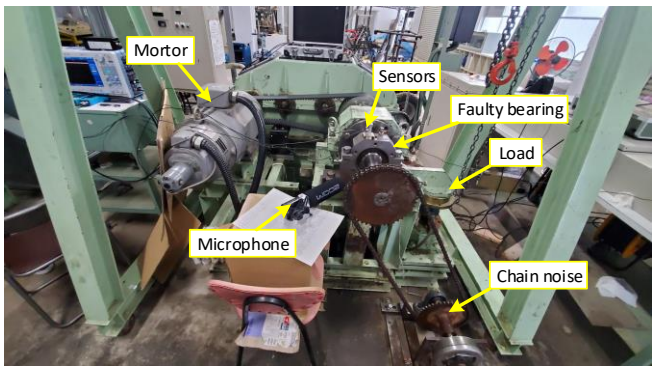

Fig.3.21 The bearing fault simulator

3.4.2.1 Analysis of bearing outer ring fault data

In this experiment, a rolling bearing model NTN NU312 was used. The diameter of the inner ring is 60mm, the diameter of the outer ring is 130mm, the width is 31mm, the number of rollers is 12. The outer ring of the bearing has been manually processed with linear damage with a width of 2.0 mm and a depth of 0.6 mm. The specific details are shown in Fig.3.22.

(a) Healthy Bearing (b) Faulty Bearing

Fig.3.22 Healthy bearing and faulty bearing

The periodic pulses in the waveform are masked by strong noise. The data was processed using Fast Entrogram and the results are shown in Fig.3.23. Extract band A which CSNE is the largest, then show its waveform and spectrum. The light color line in Fig.3.24b is the spectrum of the original signal, and the blue line is the spectrum of the component A.

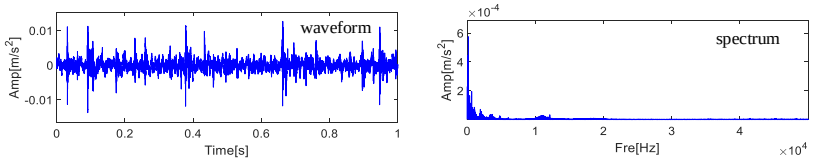

Fig.3.23 The original signal and its spectrum.

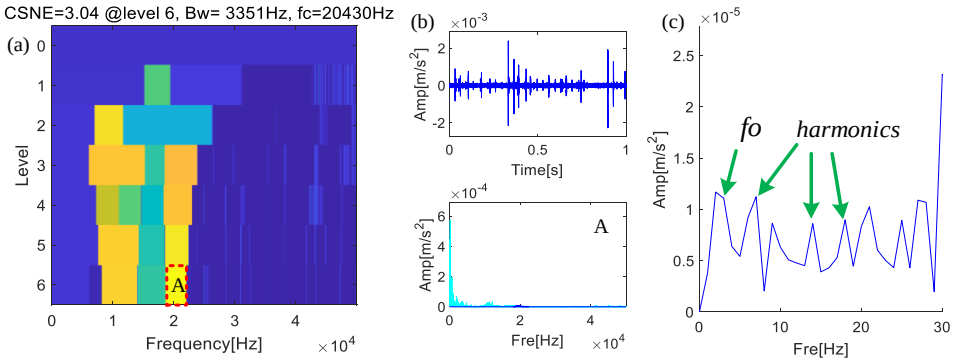

Fig.3.24 The results decomposed by Fast Entrogram: (a) Fast Entrogram; (b) Component A and its spectrum; (c) Envelope spectrum of A.

For this bearing outer ring fault data, Fast Entrogram believes that the frequency band with a center frequency of 20430 Hz and a bandwidth of 3351 Hz contains bearing fault information. The waveform of component A contains periodic pulses. In addition, the envelope spectrum contains the bearing outer ring fault characteristic frequency and its harmonics, which proves that the signal contains periodic pulse information and the bearing outer ring is damaged. The Fast Entrogram proposed in this section can effectively extract periodic pulse information in the rolling bearing vibration signal and successfully diagnose the fault. Fast Kurtogram may not be able to achieve perfect results when dealing with such signals. Fig.3.25 shows the results of Fast Kurtogram. The spectral kurtosis of the signal in the sixth frequency band of Level 6 is the largest. This level divides the spectrum into too many parts. The 64 components averaged the 50000 Hz, and each component has a width of 781 Hz. After extracting the component B, the waveform and spectrum are shown in Fig.3.25b. The frequency band extracted by this method is too narrow. So, there is no outer ring fault characteristic frequency in the envelope spectrum, there are few harmonics. Therefore, the failure of the outer ring of the bearing is not certain.

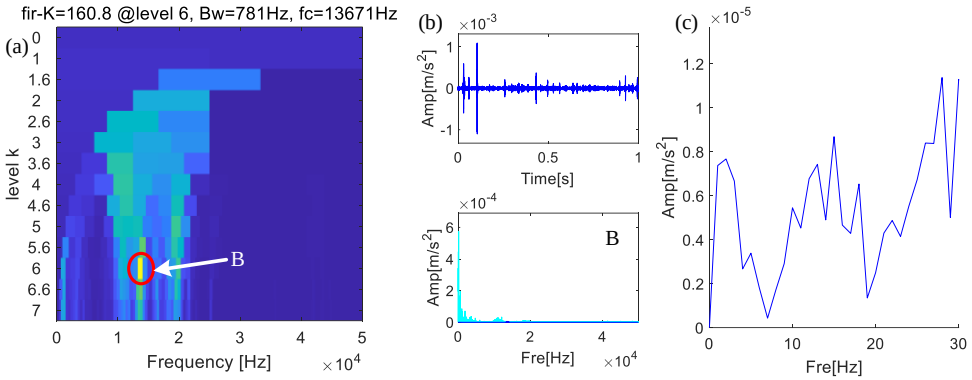

Fig.3.25 The result decomposed by Fast Kurtogram: (a) Fast Kurtogram; (b) Component B and its spectrum; (c) Envelope spectrum of B.

3.4.2.2 Analysis of bearing inner ring fault data

The faulty inner ring bearing used in this experiment was manually processed with linear damage with a width of 2.0mm and a depth of 0.6mm. The specific details of the inner ring of the bearing are shown in Fig.3.26a. Fig.3.26b shows the waveform and its spectrum of the signal. In the spectrum of the signal, the amplitude of the low frequency part is higher than high frequency part.

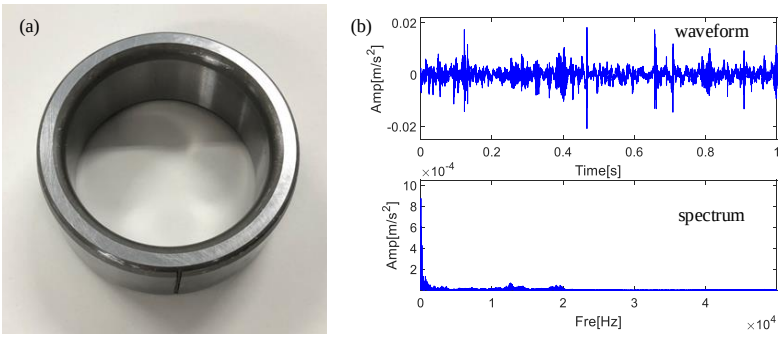

Fig.3.26 (a) The inner ring faulty bearing; (b) Original signal and its spectrum.

The higher amplitude part does not contain a lot of fault information, it cannot be determined that the lower amplitude part does not contain fault information. Since the bearing inner ring fault information is spread over the full frequency band of the spectrum, the higher amplitude of the low frequency part may mask the fault information. At this point, the high frequency part might contain more fault information.

The signal is processed using Fast Entrogram proposed in this section, shown in Fig.3.27. The spectrum is divided into 9 levels. Among them, level 4 obtained the most number of frequency bands. At level 4, the largest CSNE is obtained. The amplitude of the clusters between 5500 Hz and 9500 Hz is low, but the largest CSNE appears here. Extract the frequency band A where the largest CSNE is located. The envelope spectrum of the reconstructed component is shown in Fig.3.27b. The envelope spectrum has the characteristic frequency of the bearing inner ring fault and its harmonics. Therefore, it can be considered that the bearing inner ring has failed. The Fast Entrogram proposed in this chapter is suitable for fault diagnosis of the inner ring of rolling bearings. Using Fast Kurtogram to process this data, the component with the maximum SK is located at Level 6 and the signal is split into 64 parts. Because the frequency spectrum is divided evenly, each frequency band is relatively small, which will cause

the characteristics of the frequency spectrum to be ignored. Fig.3.28a shows the processing results of Fast Kurtogram. The largest SK occurs in the 36th frequency band. Then extract component B and show the envelope spectrum in Fig.3.28b. It is difficult to find the fault characteristic frequency of the inner ring of the bearing from the envelope spectrum. Therefore, it is not certain that the signal contains fault information and whether the device has failed.

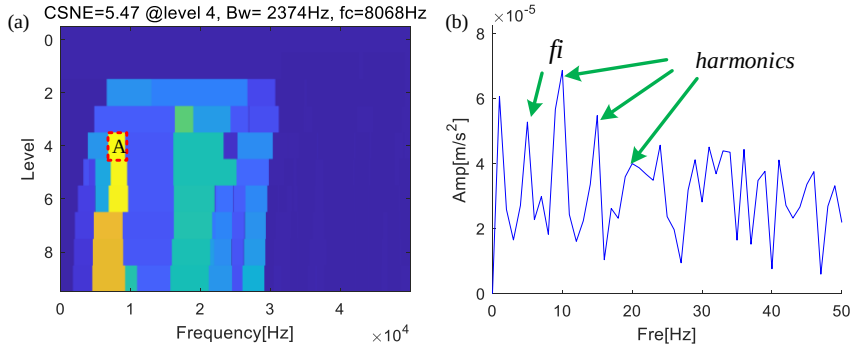

Fig.3.27 The result decomposed by Fast Entrogram: (a) Fast Entrogram; (b) the envelope spectrum of A.

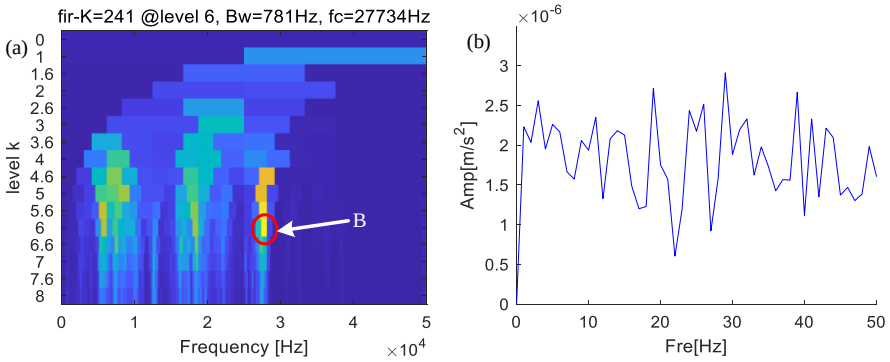

Fig.3.28 The result decomposed by (a) Fast Kurtogram; (b) the envelope spectrum of B

3.5 Conclusion

A new Fast Entrogram method for segmenting the spectrum and extracting periodic pulse information from the frequency domain was proposed in this chapter. The Fast Entrogram method obtains different trend spectrum and boundary positions by changing the number of reconstructed points. Then, the frequency slice wavelet transform with better filtering effect than the FIR filter and WPT was used to extract the components in each frequency band. In order to filter fault information from the components, a novel indicator named correlation spectral negentropy that could suppress random pulse and noise and could amplify periodic information was proposed.

The research proves that the proposed method not only increases the adaptability of the frequency slice wavelet transform, but also optimizes and improves the boundary segmentation method, component filtering effect and feature screening indicator of Fast Kurtogram. The simulation signal verifies that the proposed correlation spectral negentropy is sensitive to periodic pulses and is not sensitive to random pulse. The offset rate of the center frequency obtained by Fast Entrogram is low, but Fast Kurtogram exceeds 5% of the confidence interval. The error rate of the bandwidth obtained by the two methods is different, and Fast Kurtogram is 60% higher than Fast Entrogram. Fast Entrogram is better in extracting periodic pulses and anti-noise ability and stability. The experimental signal also proves that Fast Entrogram can be effectively applied to the fault diagnosis of the inner and outer rings of rolling bearings.

Chapter 4
Multilevel Spectral Segmentation Method Based on Improved Empirical Wavelet Transform and the Extraction Strategy of Bearing Fault Features [40-42]

4.1 Introduction

If only extreme points are considered, but the relationship between the spectral fluctuation characteristics and the signal is ignored, new problems will appear. With the improvement and upgrade of data acquisition equipment, high sampling frequency and big data analysis have also developed. Due to the higher complexity of the Fourier spectrum, the number of extreme points is greatly affected by the sampling frequency. When analyzing signals with long data, the original method will reduce the quality of the components and affect the effectiveness and efficiency of diagnosis. In order to reduce the number of invalid components and suppress mode aliasing, two concise spectral segmentation methods based on power spectral density are tried to optimize the empirical wavelet transform and a new screening index for periodic pulse components is designed.

Firstly, we proposes a new variable spectral segmentation empirical wavelet transform (VEWT). Different from the traditional scale-space representation and the existing direct segmentation methods, this chapter proposes the selective spectral segmentation (SSS) method. This metiod sets the modal determination before the boundary segmentation, and proposes a modal estimation method based on Multitaper power spectral density (MPSD). Since MPSD is associated with the fluctuation trend of the spectrum, the extreme points obtained by the SSS are less than the Fourier spectrum, and the number of modes obtained is relatively less. On the basis of Levenberg-Marquardt-Fletcher (LMF), an extended algorithm is proposed and the positions of the modes obtained by MPSD in the spectrum are used to calculate the bandwidth corresponding to their center frequencies. The information in each frequency band will be determined as the final mode. In the process of cyclic extraction, a series of boundaries associated with the fluctuations of the spectrum will be obtained. The simulation signal in EWT is used to verify the effectiveness of the proposed method. The MIT-BIH Arrhythmia Database was used to verify the applicability of the proposed method. The influence of noise on the decomposition process can be reduced, and the number of useless components will be reduced. The dependence of the original method on the minimum point is avoided, and the frequency bands in the same type of information concentration will not be separated.

Secondly, in order to reduce the number of invalid components and suppress modal aliasing, this chapter proposes an adaptive and concise empirical wavelet transform (ACEWT). First, the power spectral density of the signal is calculated and used to separate the modes. On the one hand, it can reduce the number of extreme points and weaken the dependence on extreme points; on the other hand, the fluctuation of PSD corresponds to the concentration of different components in the signal, which provides a basis for the process of segmenting the spectrum. In order to expand the application of this method, this cchapter implements adaptive spectral segmentation by constructing a new tower boundaries distribution diagram. The optimized diagram contains different levels of segmentation, and the spectrum would be divided into several frequency bands with different widths. Scholars can extract information of interest from this diagram according to specific methods. This chapter mainly extracts the periodic pulse

information in the signal, and the fault information in the rotating machinery, especially the rolling bearing signal, to provide a new method for fault diagnosis. Then, the tower boundaries distribution diagram (W-Autogram) proposed in this chapter may have narrow frequency bands when the sampling frequency is large. The reconstructed waveforms of such frequency bands are likely to contain pulses and affect the sensitivity of unbiased autocorrelation. In addition, the fault information of the bearing signal is often concentrated around a center frequency in the Fourier spectrum. The more sidebands and less noise the component contains, the easier it is to find faults. Narrow frequency bands containing pulses are usually interference information. In order to filter the fault information in W-Autogram, this chapter proposes a weighted unbiased autocorrelation that correlates the index and the bandwidth.

Lastly, Harmogram is proposed which belongs to multi-level decomposition method. Harmogram avoids the 1/3-binary tree spectral segmentation method and obtains the results of multi-level segmentation through different trend components of the spectrum to perform multi-level decomposition. In order to filter the periodic pulse information in each frequency band of each level, a harmonic spectral kurtosis (HSK) with strong anti-noise ability and anti-single pulse interference ability is proposed. Finally, the selected frequency bands are filtered by scaling function and empirical wavelets constructed based on the variant Meyer wavelet. The simulation results and experimental results show that the method has a good effect in the analysis of rolling bearing fault diagnosis.

4.2 Empirical wavelet transform

4.2.1 Basic concepts of empirical wavelet transform

The essence of empirical wavelet transform is a set of filters based on Meyer wavelet which can decompose the signal into several components. The Fourier spectrum is calculated and normalized to $[0,\pi]$. A parameterless method based on scale-space representation can calculate boundaries that may divide the spectrum into plenty of parts. Each frequency band is defined as a useful mode. Provided that the number of useful modes is defined as N, set ω as boundaries calculated by scale-space method among the bands: $\omega_0 = 0$, $\omega_N = \pi$. The first and second frequency bands can be expressed as $\Lambda_1 = [\omega_0, \omega_1]$, $\Lambda_2 = [\omega_1, \omega_2]$. Set $n = 1,2,\dots,N$, $\Lambda_n = [\omega_{n-1}, \omega_n]$, The spectrum can be expressed as: $\bigcup_{n=1}^{N} \Lambda_n = [0,\pi]$.

EWT will construct a band-pass filter for each frequency band. There is a transition phase between adjacent filters. The transition phase is centered at ω. $2\tau_n$ is the width. The basic structure of the filter is: the transition phase is a set of mutually orthogonal trigonometric functions, and the center of the frequency band is constant. The scaling function $\widehat{\emptyset}_n(\omega)$ and the empirical wavelets $\widehat{\Psi}_n(\omega)$ can be defined as:

$$\widehat{\emptyset}_n(\omega) = \begin{cases} 1; |\omega| \le (1-\gamma)\omega_n \\ \cos\left[\frac{\pi}{2}\beta\left(\frac{1}{2\gamma\omega_n}(|\omega| - (1-\gamma)\omega_n)\right)\right]; \\ (1-\gamma)\omega_n \le |\omega| \le (1+\gamma)\omega_n \\ 0; others \end{cases} \tag{4.1}$$

$$\widehat{\Psi}_n(\omega) = \begin{cases} 1; (1+\gamma)\omega_n \le |\omega| \le (1-\gamma)\omega_{n+1} \\ \cos\left[\frac{\pi}{2}\beta\left((|\omega| - (1-\gamma)\omega_{n+1})/2\gamma\omega_{n+1}\right)\right]; \\ (1-\gamma)\omega_{n+1} \le |\omega| \le (1+\gamma)\omega_{n+1} \\ \sin\left[\frac{\pi}{2}\beta\left((|\omega| - (1-\gamma)\omega_{n+1})/2\gamma\omega_n\right)\right]; \\ (1-\gamma)\omega_n \le |\omega| \le (1+\gamma)\omega_n \\ 0; others \end{cases} \tag{4.2}$$

where the transition function $\beta(x)$, the coefficient γ, and the transition phase τ_n are:

$$\beta(x) = x^4(35 - 84x + 70x^2 - 20x^3) \tag{4.3}$$

$$\gamma < \min\left(\frac{\omega_{n+1}-\omega_n}{\omega_{n+1}+\omega_n}\right) \tag{4.4}$$

$$\tau_n = \gamma\omega_n, 0 < \gamma < 1 \tag{4.5}$$

Set the Fourier transform as $F(\cdot)$, the inverse Fourier transform is $F^{-1}(\cdot)$. The detail coefficients W_f^ε can be defined as:

$$W_f^\varepsilon(n,t) = \langle f(t), \Psi_n(t)\rangle = \int f(\tau)\overline{\Psi_n(\tau - t)}d\tau = F^{-1}(\hat{f}(\omega)\widehat{\Psi}_n(\omega)) \tag{4.6}$$

Calculate the approximation coefficients $W_f^\varepsilon(0,t)$:

$$W_f^\varepsilon(0,t) = \langle f(t), \emptyset_1(t)\rangle = \int f(\tau)\overline{\emptyset_1(\tau - t)}d\tau = F^{-1}(\hat{f}(\omega)\widehat{\emptyset}_1(\omega)) \tag{4.7}$$

where $\hat{f}(\omega)$, $\widehat{\emptyset}_1(\omega)$, $\widehat{\Psi}_n(\omega)$ are the Fourier transforms of $f(t)$, $\emptyset_1(t)$, and $\Psi_n(t)$.

The signal can be rebuilt as follows:

$$\begin{aligned} f(t) &= W_f^\varepsilon(0,t) * \emptyset_1(t) + \sum_{n=1}^{N} W_f^\varepsilon(n,t) * \Psi_n(t) \\ &= F^{-1}\left(\widehat{W}_f^\varepsilon(0,\omega)\widehat{\emptyset}_1(\omega) + \sum_{n=1}^{N}\widehat{W}_f^\varepsilon(n,\omega)\,\widehat{\Psi}_n(\omega)\right) \end{aligned} \tag{4.8}$$

where $\widehat{W}_f^\varepsilon(0,\omega)$ and $\widehat{W}_f^\varepsilon(n,\omega)$ are the Fourier transforms of $W_f^\varepsilon(0,t)$ and $W_f^\varepsilon(n,t)$. The empirical mode could be given by:

$$\begin{cases} f_0(t) = W_f^\varepsilon(0,t) * \emptyset_1(t) \\ f_k(t) = W_f^\varepsilon(k,t) * \Psi_k(t) \end{cases} \tag{4.9}$$

4.2.2 Boundaries detection and its defects

EWT proposed by Gilles detects the boundaries through the scale-space representation, and needs to search for meaningful modes from the histogram. The scale-space satisfies the semigroup characteristics, so iterative convolution is used to find the minimum points at different scales, and then obtain the appropriate boundaries. However, in a signal containing noise, the number of iterations is not only affected by the number of extreme points, which increases the workload but also causes more boundaries and errors. Sometimes EWT cannot obtain reasonable boundaries, and sometimes it generates a large number of boundaries. We set three cosine signals with different frequencies. They are three lines with different amplitudes in the spectrum: 100Hz/150Hz and 300Hz, which is A/B/C in Fig.4.1. The other frequency components in the spectrum are noise. Component C at 300 Hz has been successfully separated. The components A/B at 100Hz and 150Hz are not separated because they are classified as the same component by EWT. In the high frequency part, EWT obtains many invalid boundaries. These noises reduce the operating efficiency of the algorithm, affect the success rate of decomposition, and bring difficulties to its application. Of course, EWT can sometimes separate these three components, but the success rate is very low, and the number of components is still large.

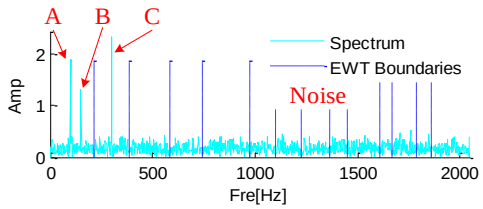

Fig.4.1 Detected boundaries by EWT

4.3 Noisy signal processing of an improved EWT

In order to solve the shortcomings of EWT mentioned, a variable spectral segmentation empirical wavelet transform (VEWT) is proposed in this section. The core of this method is the selective spectral segmentation method, which is different from the scale-space representation. The characteristic of the selective spectral segmentation method is that the determination of the modal is set before the determination of the boundaries. On the one hand, the components that make up the signal should be successfully separated. Section 4.3.1 introduces the modal estimation method based on Multitaper power spectral density (MPSD), and Section 4.3.2 proposes an extended algorithm based on Levenberg-Marquardt-Fletcher (LMF). The positions of the modes obtained by MPSD in the spectrum are used to calculate the bandwidth corresponding to their center frequencies. The information in each frequency band will be determined as the final mode. In the process of cyclic extraction, a series of boundaries associated with the fluctuations of the spectrum will be obtained. The steps of VEWT can be described as follows and shown in Fig.4.2:

1. Load the signal and calculate the power spectral density via Multitaper estimate method..

2. Propose an extended algorithm based on Levenberg-Marquardt-Fletcher. Use the position of the mode obtained by MPSD in the spectrum to calculate the bandwidth corresponding to their center frequencies.

3. Determine each bandwidth as the boundaries

4. Obtain the Fourier spectrum of the signal by Fast Fourier transform and normalize it to the frequency range $[0, \pi]$. The boundaries can divide the same position in the Fourier spectrum into several components.

5. Construct filter bank based on scale function and empirical wavelet function.

6. Reconstruct the information in each filter. The original signal will be decomposed into several components located in different frequency bands.

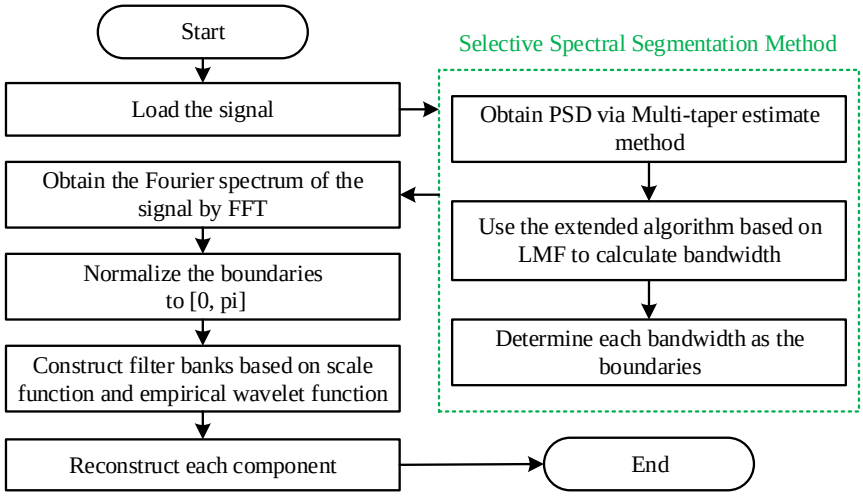

Fig.4.2 Flowcharts of the proposed VEWT method

4.3.1 Mode estimation method based on multitaper power spectral density

The Fourier spectrum contains the details in the signal. Compared with Fourier spectrum, PSD has fewer details and lower complexity. PSD can not only inherit the fluctuation trend of the amplitude of the Fourier spectrum, but also contains fewer extreme points to weaken the influence of noise [114]. In this section, Multitaper power spectral density (MPSD) is used to estimate the center frequencies of the modes. The method can not only improve the accuracy of

PSD estimation, but also reduce the variance. For a zero-mean stationary time signal $y(t)$ with unit sampling, $t \in [0,1,\dots,N-1]$, the Fourier transform is $\hat{Y}(f)$, it's spectral density is $S(f)$ and the MPSD is $\bar{S}(f)$ which can be calculated by:

$$\bar{S}(f) = \frac{1}{M}\sum_{m=0}^{M-1}\widehat{S^{(m)}}(f) \tag{4.10}$$

which is an average of M approximately independent estimates of PSD that can decrease the variance of the overall estimate. The important functions in Eq.4.10 can be obtained as follows:

$$\widehat{S^{(m)}}(f) = \left|\sum_{t=0}^{N-1} g^{(m)}(t)y(t)e^{-i2\pi ft}\right|^2 \tag{4.11}$$

where $g^{(m)}(t)$ is the mth taper orthogonal to other tapers.

It can be found from Eq.4.10 and Eq.4.11 that PSD is a positive number greater than zero and is a frequency-dependent spectrum. n order to show the details and differences between Fourier spectrum and Multitaper PSD, We designed a new complex signal. The new signal consists of six components. Signal 1 is a cosine at 100 Hz with amplitude of 5; Signal 2 is a modulation signal; Signal 3 is a single pulse with a center frequency of 1500 Hz; Signal 4 is interference information with a center frequency of 2500 Hz and a bandwidth of 35 Hz; Signal 5 is the periodic pulses with a center frequency of 3500Hz and a bandwidth of 100Hz; Signal 6 is random noise. Fig.4.3a is the waveform of the six signals, and Fig.4.3b is their Fourier spectra. Noise exists in the entire spectrum. Fig.4.3c shows the spectrum and Multitaper PSD of the superimposed signal. The Fourier spectrum is complex and contains many details, but it is also disturbed by noise. Multitaper PSD suppresses the noise, thereby making it cleaner. The single pulse at 1500 Hz is weak in the Fourier spectrum, but it is easy to recognize from the Multitaper PSD. In short, the fluctuation trend of MPSD is roughly the same as the Fourier spectrum, but there are differences. MPSD is like the upper envelope of the spectrum.

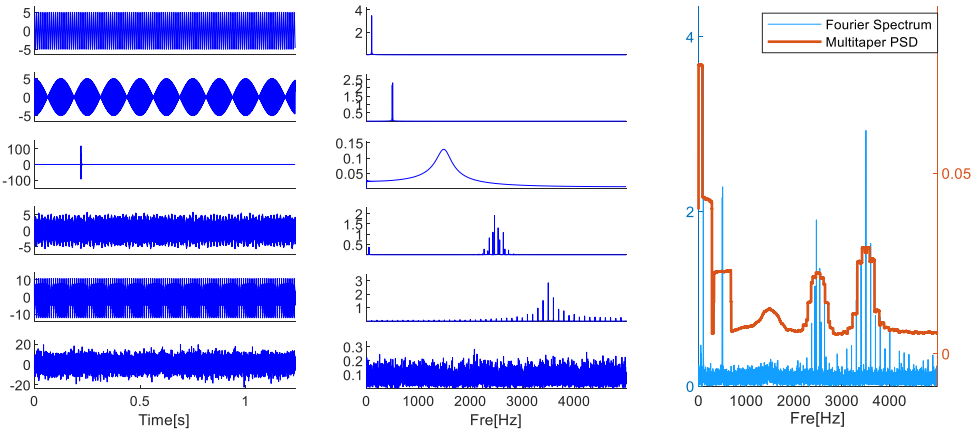

(a) Five signals (b) Five spectra (c) Multitaper PSD

Fig.4.3 Fourier spectrum and Multitaper PSD representation

4.3.2 Bandwidth estimation method based on the extended algorithm of Levenberg-Marquardt-Fletcher (LMF)

In EWT, the scale-space representation is used to divide the Fourier spectrum. The essence of this method is to obtain bandwidth. When the signal does not contain noise, the error tolerance rate of the obtained boundary position is higher. When the signal contains noise, the frequency bands obtained by EWT sometimes contain a lot of noise, because the position of boundaries directly determines the quality of the empirical modes. Fig.4.4a is a cosine signal. After adding the noise shown in Fig.4.4b to it, the waveform is shown in Fig.4.4c.

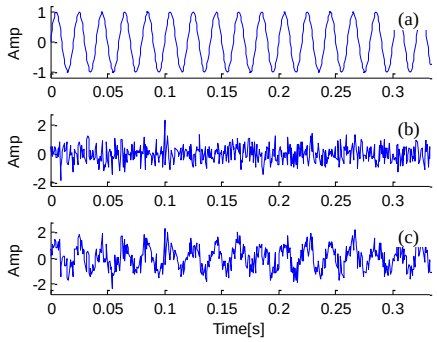

Fig.4.4 (a) The cosine signal; (b) noise; (c) the signal added noise.

The spectrum of the noise-added cosine signal is relatively simple: there is higher amplitude at 50 Hz, and the other positions are noise. Three pairs of boundaries (Fig.4.5a) are set up among which group A has the largest bandwidth. A: [6 Hz, 378 Hz], B: [15 Hz, 165 Hz], C: [42 Hz, 57 Hz]. The components obtained from these three sets of boundaries are processed by EWT, and the results can be observed in Fig.4.5. The noise in Component A with the largest bandwidth seriously affects the waveform. Component B contains a small amount of noise, and the waveform is distorted. The bandwidth of component C is the narrowest and its waveform recovery is higher. The width of the frequency band is related to the amount of noise in the component, and the way of calculating the bandwidth may contain less noise than the way of dividing the spectrum. Therefore, this section proposes a bandwidth estimation method based on the extended algorithm of LMF to identify the bandwidth of the component in MPSD.

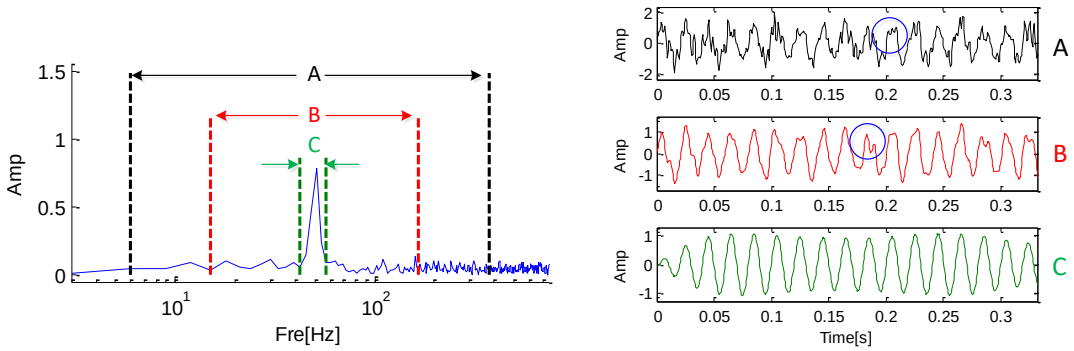

(a) Three different split modes

(b) Three components with different split modes

Fig.4.5 Three split modes and there components.

As a parameter recognition technology, LMF was introduced to assist in the design of extended algorithm [115]. A narrower bandwidth can be determined, and a smaller number of boundaries may be obtained. The steps of the bandwidth estimation method based on extended algorithm can be described as follows:

1. For the signal $s(t)$, its MPSD can be calculated as $\bar{S}(f)$. Then, the maximum sequence of MPSD can be expressed as P_{max}. The maximum value $\bar{S}(f(l_1))$ and the second largest value $\bar{S}(f(l_2))$ in the position of P_{max} can be represented by l_1 and l_2, the corresponding frequencies are $f(l_1)$ and $f(l_2)$.

2. Define the position of the frequency of 2/3 times the maximum value of $f(l_1)$ in the high−frequency direction as the initial half−value width b_1; Define the position 2/3 times of $f(l_2)$ as the initial half−value width b_2.

3. The initial half-band width $b_f^{(1)}$ of the maximum value and the initial half−band width

$b_f^{(2)}$ of the second largest value can be calculated:

$$\begin{cases} b_f^{(1)} = |f(l_1) - f(l_1 + b_1)| \\ b_f^{(2)} = |f(l_2) - f(l_2 + b_2)| \end{cases} \tag{4.12}$$

4. Calculate the negative difference between the frequency $f_x(k)$ and the specific frequency, $k \in [0, \pi]$:

$$\begin{cases} r_1 = -|f_x(k) - f(l_1)|^2 \\ r_2 = -|f_x(k) - f(l_2)|^2 \\ r_3 = -\left|f_x(k) - \frac{f(l_1)+f(l_2)}{2}\right|^2 \end{cases} \tag{4.13}$$

5. Define the formula:

$$\text{Phi} = (x)\left\{\bar{S}(f) - \left[x(1)e^{\frac{r_1}{2(x(4))^2}} + x(2)e^{\frac{r_2}{2(x(5))^2}} + x(3)e^{\frac{r_3}{2(x(6))^2}}\right]\right\} \tag{4.14}$$

Define the array:

$$X_0 = \left[\frac{\bar{S}(f(l_1))}{2}, \frac{\bar{S}(f(l_2))}{2}, \frac{\bar{S}(f(l_1))+\bar{S}(f(l_2))}{4}, b_f^{(1)}, b_f^{(2)}, 4(f(l_1) - f(l_2))\right] \tag{4.15}$$

6. After solving a set of nonlinear equations in the least square sense through the LMF algorithm, a new array X_1 will be obtained. The new bandwidth is defined as $2.5 \cdot X_1(4)$. For specific steps, please refer to [115].

4.3.3 Simulation signal verification

4.3.3.1 Case study 1

The second signal contains a periodic high frequency component and a cosine:

$$\begin{cases} s_{c1} = \sin(2\pi \cdot f_1 t) \times (u(t - 0.09) \\ \quad -u(t - 0.15) + u(t - 0.34) \\ \quad -u(t - 0.4) + u(t - 0.59) \\ \quad -u(t - 0.65) + u(t - 0.84) \\ \quad -u(t - 0.9)) \\ s_{c2} = \cos(2\pi \cdot f_2 t) \\ s_2 = s_{c1} + s_{c2} + \eta \end{cases} \tag{4.16}$$

where $f_1 = 200$ Hz; $f_2 = 2$ Hz; and $\eta = \text{SNR}(-2\text{ dB})$, $u(t)$ is the step signal, the sampling frequency is 2 kHz, collection time $t = 1$ s. The first component has high frequency information in the four time periods [0.09s-0.15s] [0.34s-0.4s] [0.59s-0.65s] [0.84s-0.9s], and these high frequency information is periodic. The center frequency is located at 200 Hz. The second component is the cosine signal at 2 Hz. Other frequency bands are filled with noise. The waveform and Fourier spectrum of this signal are shown in Fig.4.6a. Signal s_2 will be decomposed into several parts by EWT, and noise will affect the results. The details of the boundary distribution of this noisy signal after being processed by EWT are shown in Fig.4.6b. Due to the complexity of the signal, the spectrum is divided into 12 parts. Too many boundaries are obtained, and more workloads arises. Due to the existence of noise, the process of obtaining the boundary of EWT is disturbed or even invalid, which brings great trouble to digital signal processing. This is the second disadvantage of EWT in processing noise-containing signals: many invalid boundaries and components. Although the spectrum is divided into many parts, the cosine component and periodic high frequency components are successfully distinguished. Component 1 is where the 2 Hz cosine component exists; Component 3 is where the periodic high-frequency component exists. Because EWT obtains too many components, Fig.4.6c only shows EM-1 to EM-4 of all results. EM-1 is a cosine component and contains too much noise

and is not smooth. EM-3 is a high-frequency shock component, but it is difficult to identify these characteristics in the waveform. In this example, although EWT successfully separates the two components, it also contains a lot of noise. If there is no further noise reduction operation, the results obtained by EWT will cause confusion for signal analysis.

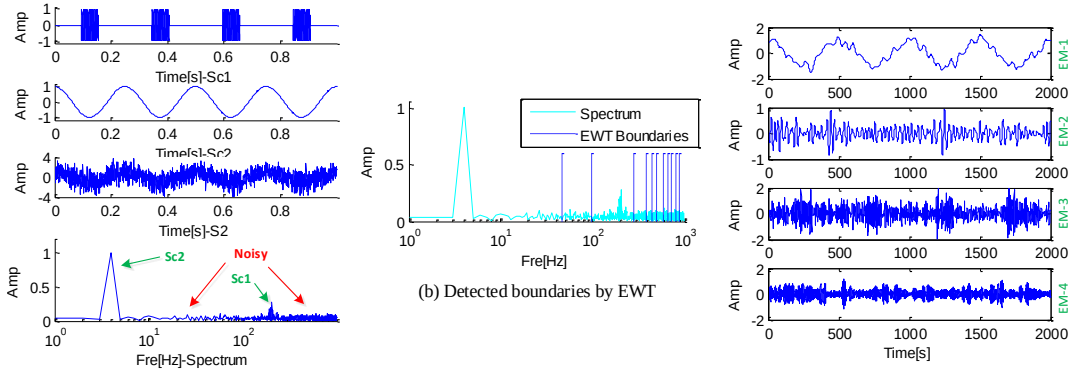

(a) Signal and its spectrum

(b) Detected boundaries by EWT

(c) Components decomposed by EWT

Fig.4.6 The results decomposed by EWT

Fig.4.7a shows the boundary distribution of the signal processed by VEWT. In order to compare with EWT, this figure uses Fourier spectrum to show the location of boundaries. The spectrum is divided into four parts which is only 1/3 of EWT. The bandwidth of Part A is 12.55 Hz, and the bandwidth of Part C is 19.2 Hz. Narrow bandwidth means less noise, so in Fig.4.7b, Part A is as smooth as the original signal, which is different from EWT. The periodic high-frequency components with a center frequency of 200 Hz are not divided into incoherent parts.

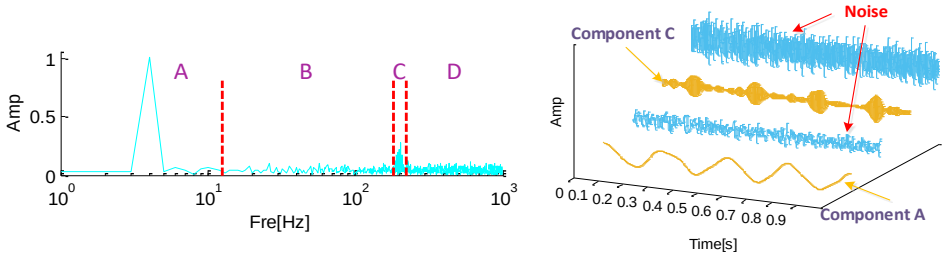

(a) Detected boundaries by VEWT

(b) Components decomposed by VEWT

Fig.4.7 The results decomposed by VEWT.

4.3.3.2 Case study 2

The signal is made with three distinct components.

$$\begin{cases} s_{c1} = \frac{1}{1.2+\cos(2\pi t)} \quad s_{c2_1} = \frac{2}{1.5+\sin(2\pi t)} \\ s_{c2_2} = 2\cos\left(2\pi \cdot f_1 t + \cos(2\pi \cdot f_2 t)\right) \\ s_{c2} = s_{c2_1} s_{c2_2} \\ s_4 = s_{c1} + s_{c2} + \eta \end{cases} \tag{4.17}$$

where $f_1 = 16$ Hz, $f_2 = 32$ Hz, and $\eta = -5$ dB. The sampling frequency is 8192 Hz, collection time $t = 1$ s. The waveform of the signal and its components are shown in Fig.4.8a. The first component increases monotonically before 0.5s, and decreases monotonously after 0.5s. The second component is more complicated; its amplitude is modulated and changes over time.

The boundaries obtained by traditional EWT and VEWT can be found in Fig.4.8b. The frequency of s_{c1} is 1Hz, and the 32Hz component should be part of s_{c2}. But the component A1 obtained by EWT does not separate the above two components, which causes serious modal aliasing. In addition, the high frequency part still contains too much noise. Unlike the above

results, VEWT has fewer boundaries. The four parts with higher peaks are separated. Among them, A2 is s_{c1} and B2 is s_{c2}. Fig.4.9 shows the results of the two methods. The modal aliasing in EWT is serious, and VEWT can better extract and restore the components in the signal.

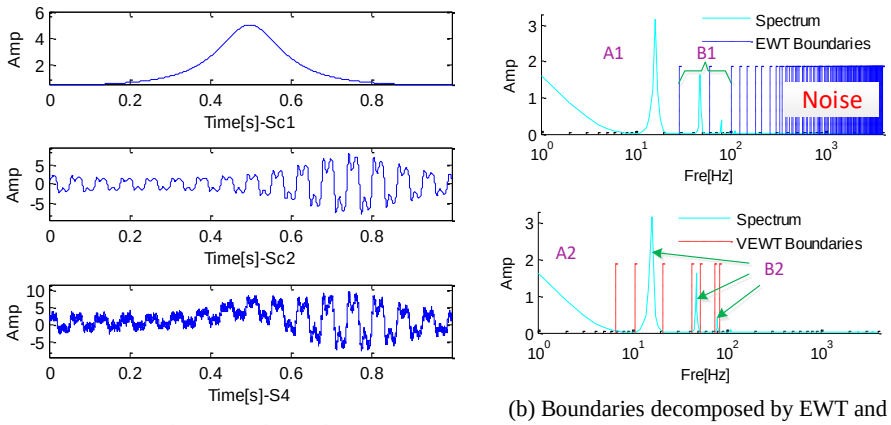

(a) The original signal

(b) Boundaries decomposed by EWT and VEWT

Fig.4.8 The signal and the boundaries obtained by EWT and VEWT.

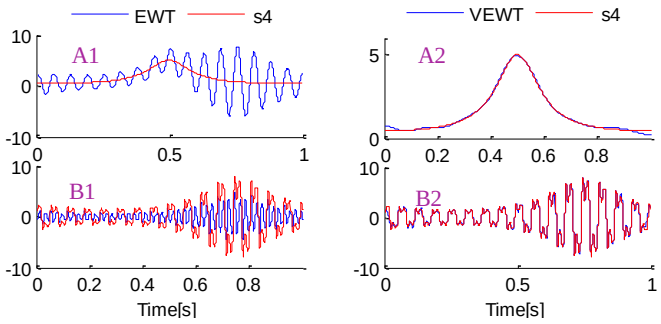

Fig.4.9 The results obtained by EWT and VEWT.

4.3.4 Applications of MIT-BIH Arrhythmia Database

MIT-BIH Arrhythmia Database is data collected and published with the support of the Beth Israel Deaconess Medical Center and Massachusetts Institute of Technology [116,117]. The database was the first generally available set of standard test material for evaluation of arrhythmia detectors, and has been used for that purpose as well as for basic research into cardiac dynamics at more than 500 sites worldwide (https://www.physionet.org/content/mitdb/1.0.0/). The MIT-BIH Arrhythmia Database contains 48 half-hour excerpts of two-channel ambulatory ECG recordings. The recordings were digitized at 360 samples per second per channel with 11-bit resolution over a 10 mV range. 20dB noise was added to verify the ability of EWT, EEWT and VEWT to extract main information. The aim of this part is to separate original signal from noise. The original signal, the noisy signal and the spectrum are shown in Fig.4.10.

EWT, EEWT and VEWT are used to process the signal separately. EWT can decompose the signal into 21 components (see in Fig.4.10b). The higher frequency part can be considered as noise, so the number of components obtained by EWT will increase the workload. The part below 60 Hz was divided into 5 parts. When the OSF window width is 123, EEWT divides the spectrum into 11 parts, and the high complexity of the low frequency part affects the segmentation process. VEWT only obtains four components in total. The part below 60 Hz is determined as one component, and the part above 60 Hz is divided into three components.

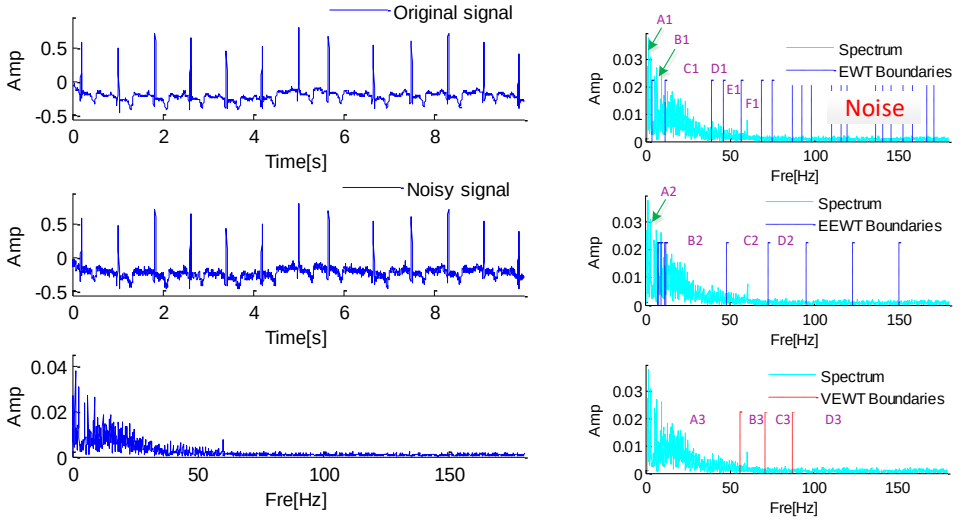

(a) The signal and its spectrum (b) Boundaries distribution

Fig.4.10 The signal and boundaries obtained by EWT, EEWT and VEWT.

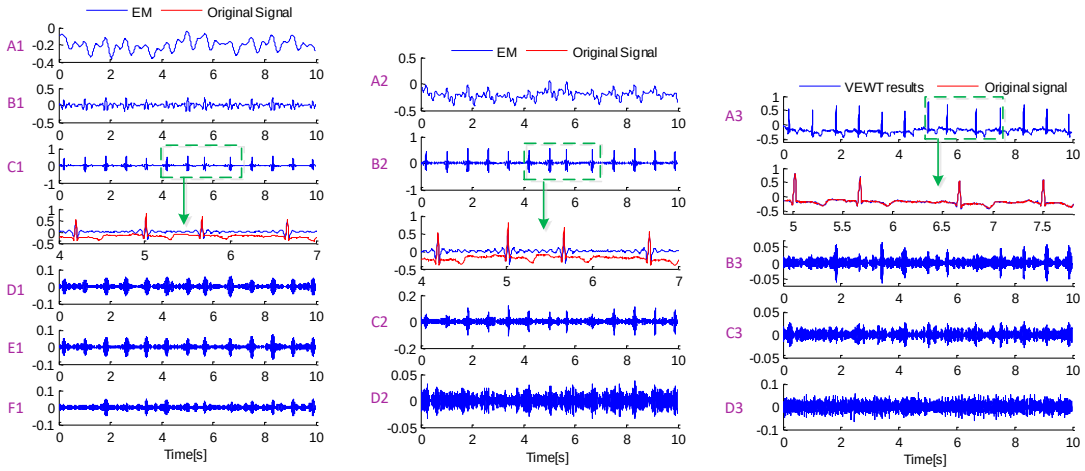

(a) EWT (b) EEWT (c) VEWT

Fig.4.11 The results decomposed by EWT, EEWT and VEWT.

Fig.4.11a shows the waveforms of EM-A1 to EM-F1 of the EWT. Show the waveform of [4s,7s] in EM-B2 and compare it with the original signal. The solid red line is the original signal. Although there are periodic pulses in EM-C1, there is also periodic information in EM-D1, EM-E1 and EM-F1. The pulse position and time interval are the same as EM-C1. Therefore, EM-D1, EM-E1 and EM-F1 contain the same information and may be one main component. In addition, EM-C1 loses many details, which contain main information about heart disease, which is important for medical analysis. EWT's meticulous segmentation method resulted in the loss of details. Extract the EM-A2 to EM-D2 marked in Fig.4.11b. Four components will be obtained. EM-B2 and EM-C2 contain periodic pulses, and EM-B2 has higher amplitude. EM-C2 contains a lot of noise, and the pulse amplitude is low. Show the waveform of [4s,7s] in EM-B2 and compare it with the original signal. The solid red line is the original signal. The average value of the obtained EM-B2 is near 0, and the low frequency information is lost. The lower frequency A2 may be useful information. There is a big error between the result of EEWT and the original signal. Fig.4.11c shows the results of VEWT. EM-A3 contains most of the energy in the original signal. There is not much periodic impact information in EM-B3. EM-C3 and EM-D3 are noise. The figure shows the details of [4.9s, 6.4s]. The red line is the original signal, and the blue line

is EM-A3. The error between the red line and the blue line is small, and Em-A3 basically matches the original signal.

Calculate the SNR and RMS of EM-C1, EM-B2 and EM-A3. The details are shown in Table 2. EEWT has the weakest noise reduction ability and VEWT has the strongest. The components obtained by EWT and EEWT are similar to the original signal, and the error of VEWT is the smallest.

Table 2 SNR and RMS of the component obtained by three methods

Index	EWT	EEWT	VEWT
SNR(dB)	0.17936	-0.11117	3.8094
RMS	0.23241	0.24031	0.15302

Since the SNR of EWT and EEWT is much smaller than that of VEWT, and the error of VEWT is only half of that of EWT and EEWT, the ratio of SNR to RMS shown in Fig.4.12 is obviously different. The ratio of the components obtained by VEWT is larger. Therefore, it can be determined that the proposed VEWT method has advantages over the original method in processing the details of the signal containing noise.

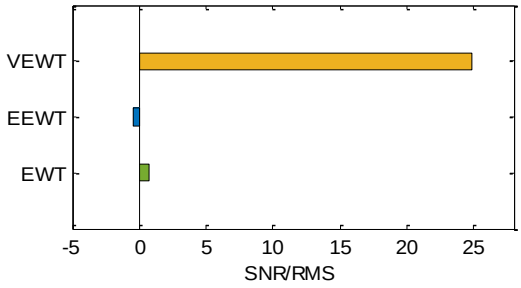

Fig.4.12 Decomposition efficiency

4.4 Proposed adaptive multilevel spectral segmentation framework

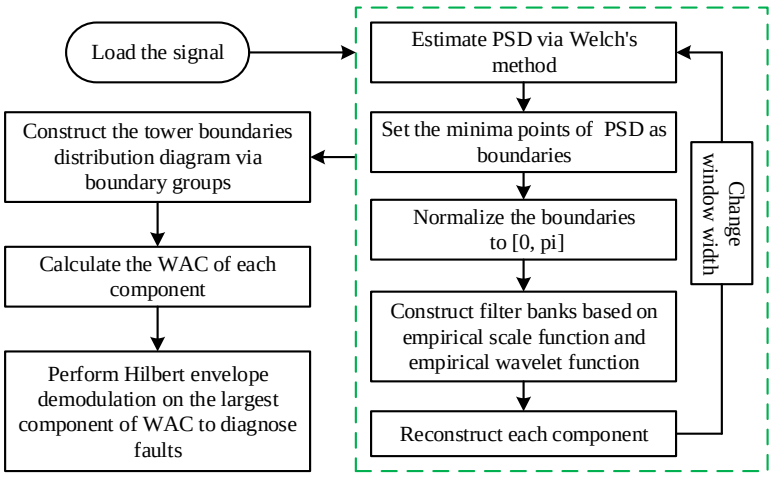

Fig.4.13 The flowcharts of the proposed methods.

In the process of calculating the modes, the most critical step is to obtain the boundaries. The number and location of the boundaries determine the number and quality of the modes. In order to improve EWT, we proposes a mode decomposition method based on PSD. Its flowchart is shown in Fig.4.13. In order to expand the application of ACEWT, we propose a new indicator. After weighting the unbiased autocorrelation, this indicator becomes more sensitive to periodic

pulse information. Further, by combining ACEWT and Weighted unbiased autocorrelation, a tower boundaries distribution diagram (W-Autogram) which can be used to extract specific information is proposed.

4.4.1 Mode estimation method based on power spectral density

This section uses PSD to replace the complex Fourier spectrum to show the distribution of components. PSD actually represents the distribution of power with frequency. For the signal $y(t)$, the Fourier transform is $\hat{y}(f)$, and its average power P can be expressed as:

$$P = \lim_{T\to\infty} \frac{1}{2T} \int_{-T}^{T} y(t)^2 dt \tag{4.18}$$

Provided that the Fourier transform of the signal in the interval $[0, T]$ is:

$$\hat{y}_T(f) = \frac{1}{\sqrt{T}} \int_0^T y(t) e^{-i2\pi ft} dt \tag{4.19}$$

Then the power spectral density can be defined as:

$$S_{yy}(f) = \lim_{T\to\infty} E[|\hat{y}_T(f)|^2] \tag{4.20}$$

It can be found from Eq.4.20 that PSD is a positive number greater than zero and is a frequency-dependent spectrum. There are several sets of simulation signals showing the relationship between the PSD and the fluctuation trend of the spectrum.

The first component is a modulation signal: $f_1 = 10$ Hz, $f_2 = 100$ Hz. The second component is a cosine: $f_3 = 400$ Hz. The third component is the periodic pulses. The natural frequency of the pulse is $f_n = 1600$ Hz, the sampling frequency $f_s = 10000$ Hz, the damping coefficient $g = 0.02$ and the repetition period $T = 0.03$ s. The simulated signal and its components are shown in Fig.4.14a. The modulation characteristics and periodic pulse information in the composed new signal are masked.

$$\begin{cases} s_{c1} = 3\cos(2\pi \cdot f_1 t) \times \cos(2\pi \cdot f_2 t) \\ s_{c2} = 3\cos(2\pi \cdot f_3 t) \\ s_{c3} = \sum_{i=1}^{M} 4e^{-g\times 2\pi f_n^i t} \times \sin\left(2\pi f_n^i t \times \sqrt{1-g^2}\right) \\ s_1 = s_{c1} + s_{c2} + s_{c3} \end{cases} \tag{4.21}$$

The simulated signal contains three components. If the modulation signal and cosine are combined into one signal, then the Fourier spectrum of the new signal has high amplitude in two frequency bands within 1000 Hz. The energy of the Fourier spectrum of the third component is concentrated around 1600 Hz. The same situation occurs in the Fourier spectrum of the signal with three components superimposed. Fig.4.14b shows the Fourier spectrum and PSD of the signal.

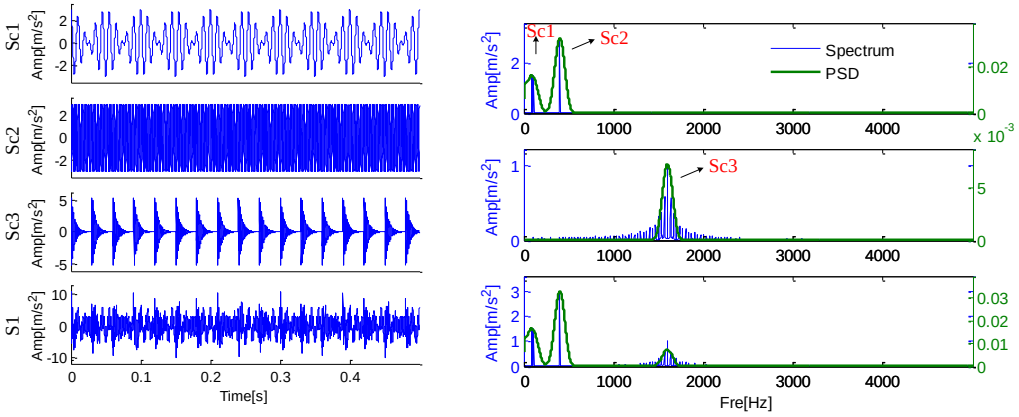

(a) Signals (b) Spectrum and PSD

Fig.4.14 (a) Three components and synthesized simulation signal; (b) Spectrum and PSD representation

The Fourier spectrum can accurately represent the details of the frequency components in the signal, which provides great convenience for the analysis process, but also brings difficulties to the most critical step in EWT. The simulated signal does not contain noise, but there are many extreme points in the Fourier spectrum. The number of extreme points affects the scale space representation method, which is the main factor that causes invalid components and modal aliasing. It can be found that PSD is smoother and contains fewer extreme points than Fourier spectrum; the modulation signal and cosine signal can be separated; for periodic pulse information, PSD contains most of the energy. When all the components are superimposed, they can also be separated. As the number of extreme points of the PSD decreases, the part with lower energy would be suppressed, and the part with higher energy would be retained. The PSD-based method can obtain fewer and more reasonable boundaries.

Add 5dB Gaussian noise to the signal. Due to the increased noise in the signal, 835 extreme points appear in the Fourier spectrum. These extreme points will interfere with the calculation process of EWT, affect the judgment of the segmentation method and shift the position of the boundaries. The PSD used in this section only obtains 19 minimum values, retains the larger amplitude components in the original signal, and suppresses noise. Therefore, this section proposes an adaptive spectral segmentation method and names it as the adaptive and concise empirical wavelet transform. The steps can be described as follows:

1. Estimate the PSD of the signal based on Welch's method.

2. Normalize the PSD of the signal to the frequency range $[0, \pi]$. There are fewer extreme points in the PSD. This paper uses the minimum value in the PSD to obtain the boundaries.

3. Construct filter bank based on empirical scale function and empirical wavelet function. Each individual filter in the filter bank represents an independent component. All components make up the original signal.

4. Reconstruct the information in each filter. The original signal will be decomposed into several components located in different frequency bands.

Use the method just mentioned to process the signal that containing noise. It can be found from Fig.4.15 that ACEWT can separate the modulated signal (A) and the cosine signal (B), and the integrity of the periodic pulse information (C) could be preserved. If the original EWT method is used to process the signal, the modulation information and cosine may not be separated (D). The frequency band representing the periodic pulses (E) contains more noise.

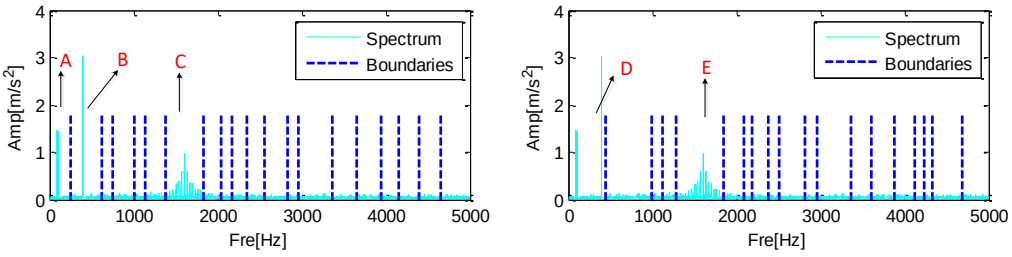

(a) Boundaries processed by ACEWT (b) Boundaries processed by EWT

Fig.4.15 The comparison of two spectral segmentation methods.

In order to verify the accuracy of ACEWT's results, component A and B representing the modulation signal and cosine signal are used to compare with the original components. Fig.4.16 shows the results of ACEWT: component A and component B are extracted. Component A and B are similar to Sc1 and Sc2 in Fig.4.14a. After amplifying the component A for 0.13s-0.28s, it can be known that they have a high degree of fit. After amplifying the component B for 0.21s-0.25s, it can be known that it is similar to Sc2. Therefore, the decomposition results of ACEWT

are effective. Since component D obtained by EWT does not separate the modulated signal from the cosine signal, it will not be further analyzed.

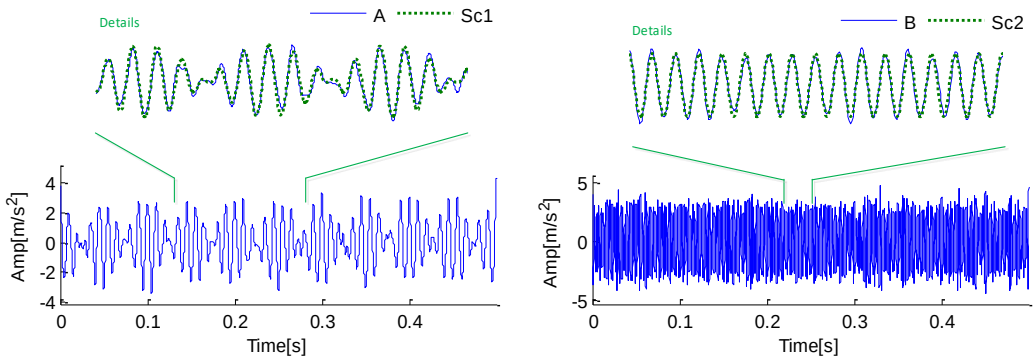

(a) Component A and its details (b) Component B and its details

Fig.4.16 The results decomposed by ACEWT.

4.4.2 Weighted unbiased autocorrelation

ACEWT proposed in this paper will obtain a set of empirical modes when processing noise and non-stationary signals. Natural frequencies and their side bands are treated as the same component. Therefore, it is necessary to automatically identify the cyclostationary information in the results. The unbiased autocorrelation of the squared envelope of the demodulated signal proposed by Moshrefzadeh is sensitive to the periodic pulse characteristics, but the single pulse can also affect the sensitivity of AC. For the collected signals, noise cannot be completely avoided. Random pulses in noise are a test for AC. During the processing of noise and non-stationary signals, ACEWT may obtain components with a narrow frequency band and containing single pulses, which may make it difficult to screen for fault information. Even if the narrow frequency band contains the natural frequency (center frequency), it cannot contain more side bands, which would cause harmonics to not appear in the process of Hilbert envelope demodulation. The extreme points obtained by the PSD-based mode decomposition method proposed will accommodate more periodic pulse information, which means that there will be almost no narrow frequency band near the center frequency. So the width of the frequency band can be used as one of the references for determining how much fault information is contained in each frequency band. This section proposes weighted unbiased autocorrelation (WAC) to screen fault information in empirical modes. It could combine the advantages of frequency bandwidth and unbiased autocorrelation to weaken non-stationary interference such as noise and single pulses that are not related to periodic pulse information influences.

For the signal $y(t)$, the n-th signal within the frequency band: $y_n(t)$. The n-th frequency band is $\Lambda_n = [\omega_{n-1}, \omega_n]$, $n = 1,2, \dots, N$, $\omega_0 = 0$, $\omega_N = \pi$. Therefore, the width of the frequency band after normalization can be expressed as: $\eta_n = \omega_n - \omega_{n-1}$. The weight of this band is:

$$\delta_n = \frac{\eta_n}{\pi} \tag{4.22}$$

The square envelope within Λ_n is $|y_n(t)|^2$, the square envelope is autocorrelated:

$$\widehat{R}_{yy}(\tau) = \frac{1}{L-q}\sum_{i=1}^{L-q}|y_n(t_i)|^2 \cdot |y_n(t_i+\tau)|^2 \tag{4.23}$$

where $\tau = q/f_s$ represents the delay factor, $q = 0,1, \dots, L-1$, f_s is the sampling frequency, and L is the length of the signal.

The kurtosis of unbiased Autocorrelation in frequency band $\Lambda_n = [\omega_{n-1}, \omega_n]$ can be defined as:

$$\kappa_n = \frac{\sum_{i=1}^{L/2}[\hat{R}_{yy}(i) - \min(\hat{R}_{yy}(\tau))]^4}{[\sum_{i=1}^{L/2}[\hat{R}_{yy}(i) - \min(\hat{R}_{yy}(\tau))]^2]^2} \tag{4.24}$$

The definition of weighted unbiased Autocorrelation (WAC) is as follows:

$$WAC_n = \delta_n \cdot \kappa_n = \frac{\eta_n}{\pi} \cdot \frac{\sum_{i=1}^{L/2}[\hat{R}_{yy}(i) - \min(\hat{R}_{yy}(\tau))]^4}{[\sum_{i=1}^{L/2}[\hat{R}_{yy}(i) - \min(\hat{R}_{yy}(\tau))]^2]^2} \tag{4.25}$$

4.4.3 Introduction to Adaptive Multilevel Spectral Segmentation Framework

ACEWT calculates the PSD of the discrete-time signal vector via Welch's method. Hamming window would be used to estimate the final spectral. After research, the width of the Hamming window is related to the fineness of PSD.

Taking the signal shown in Eq.4.21 as an example, the method proposed in this section is used to calculate PSD. If the window width is set to 5, PSD is a monotonically decreasing curve. The curve shows that the amplitude of the spectrum decreases with increasing frequency. If the window width is set to 20, the initial amplitude of the PSD is high, but two peaks and two troughs appear in the curve. The curve shows that the amplitude of the spectrum does not decrease continuously as the frequency increases. There are two parts of the energy in the spectrum that are concentrated, and the two parts of the energy are bounded by the first trough. If the window width is set to 100 or higher, the PSD becomes a more complex curve with more peaks and valleys. The curve separates the modulated signal, the cosine signal, and the frequency band containing the periodic pulse information with several troughs. The above situation is shown in Fig.4.17. It can be see that the choice of the window width directly affects the fineness of the PSD, the number of boundaries and the quality of the final empirical modes.

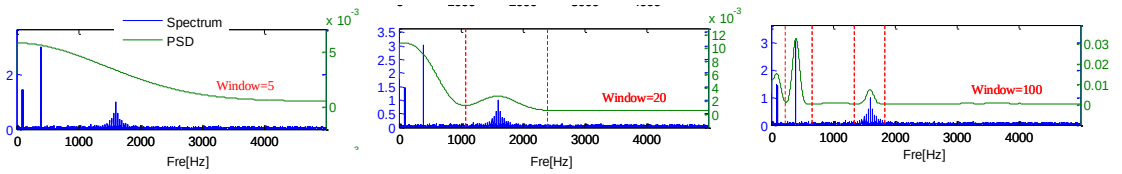

Fig.4.17 The relationship between PSD and window width.

The method proposed in this section treats the minimum points in the PSD as boundaries to distinguish different empirical modes, and the size of the window width is related to the number and position of the boundaries. This section proposes to obtain different boundary groups by changing the window width, and combines all the boundary groups into a tower boundaries distribution diagram (W-Autogram). This section proposed W-Autogram based on ACEWT and WAC. The segmentation method is related to the signal, so there is no fixed boundary position. The number of boundaries is proportional to the window width.

4.4.4 Application

The experimental data used in this paper comes from the bearing failure test bench of Mie University, Japan, as shown in Fig.2.21. The type of the bearing is NU204. The inner ring of the bearing has a width of 0.5 mm and a depth of 0.15 mm. The outer ring of the bearing has a width of 0.3 mm and a depth of 0.05 mm. A static load of 150 kg was used in the experiment. The speed of shaft rotation is: 1500 rpm/s, the sampling frequency $f_s = 100$ kHz. After calculation, the bearing inner ring fault characteristic frequency is $f_I = 170$ Hz, the period $T_I = 0.0059$ s. The bearing outer ring fault characteristic frequency is $f_O = 100$ Hz, the period $T_O = 0.01$ s.

4.4.4.1 Analysis of Bearing inner Ring Fault Data

The bearing inner ring fault data, its spectrum and its envelope spectrum are shown in Fig.4.18. There are noticeable pulses in the waveform. After observation, it can be found that the interval of the distribution of these pulses is longer, and the interval between different pulses is different. It is unrealistic to calculate the period of the signal. Filtering this signal can reduce the interference of noise on the fault information, which is equivalent to amplifying the periodic pulse information. For the spectrum, it can be seen that the frequency band with a frequency lower than 3 kHz has high amplitude. However, the actual situation is complicated; this part may not contain more failure information. The frequency band containing the most fault information may be masked by noise.

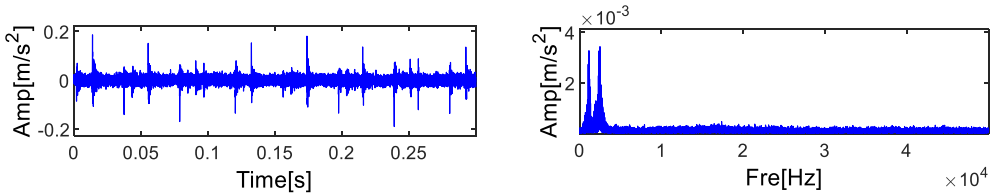

Fig.4.18 The inner ring fault data and its spectrum.

The results decomposed by Fast Kurtogram can be found in Fig.4.19. The width of the frequency band decreases as the number of the level increases. The narrow frequency band is only related to the number of division levels, and has nothing to do with all characteristics of the signal. The highest kurtosis is located in the third band in Level 5.6. The center frequency of this band is 2604 Hz, the bandwidth is 1042 Hz, and the kurtosis is 1.8.

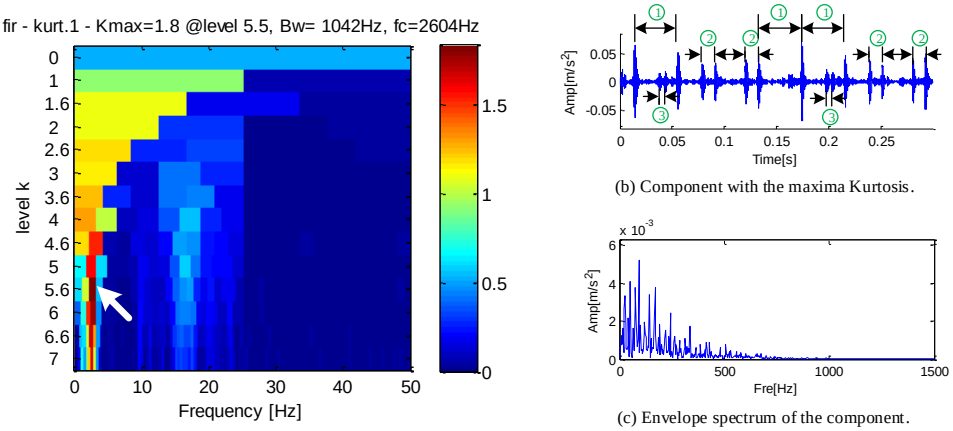

(a) Fast Kurtogram

(b) Component with the maxima Kurtosis.

(c) Envelope spectrum of the component.

Fig.4.19 The results decomposed by Fast Kurtogram.

Table 3 Time interval between pulses

Unit: s

Order	1	2	3	4
①	0.0415	0.0415	0.0416	—
②	0.0122	0.0118	0.0121	0.0118
③	0.0056	0.0060	—	—

Observe the waveform after extracting this band. There are pulses in the waveform, but there are several groups of pulses with the same period. The time interval of the marked interval in the figure can be searched in Table 3. It can be found that only the third type of time interval is the same as the fault period of the bearing inner ring. The number of pulses with the same time interval as the third type is small and the amplitude is low. Therefore, the fault information

in the extracted components is still strongly disturbed and difficult to be identified.

W-Autogram is used to process the bearing inner ring fault data. From Fig.4.20, the part with frequency less than 10 kHz is regarded as one component in the window width variation range (17-69). The WAC in this band is less than 10 and is not the maximum at any window width. It can be judged that the fault data contained in it is not as much as Kurtogram. Although the amplitude of the spectrum between 10 k-30 kHz is low, W-Autogram still treats this frequency band as a component. In Fig.4.20a, the largest WAC appears at Level 3, with a window width of 25, a center frequency of 21.6 kHz, and a bandwidth of 24.95 kHz. Fig.4.20b displays the relationship between the spectrum and PSD when the window width is 25. There is a maximum near 17000 Hz. Since WAC in this band is the largest, it is likely to contain a sideband near the maximum value representing the bearing inner ring fault information. Extract the largest WAC component and display it in Fig.4.20c. The number of pulses in the signal is large and it is easy to discern periodicity. In order to show the periodicity of the pulses, the signal between 0.3s and 0.11s can be taken out and observed separately. Although there are no obvious pulses between 0.58s and 0.78s, four consecutive equally spaced pulses can be found before 0.058s and after 0.078s. The time interval is 0.006s, which is equal to the failure of the bearing inner ring. Therefore, it can be judged that the signal contains the bearing inner ring fault information, and the bearing inner ring may be faulty.

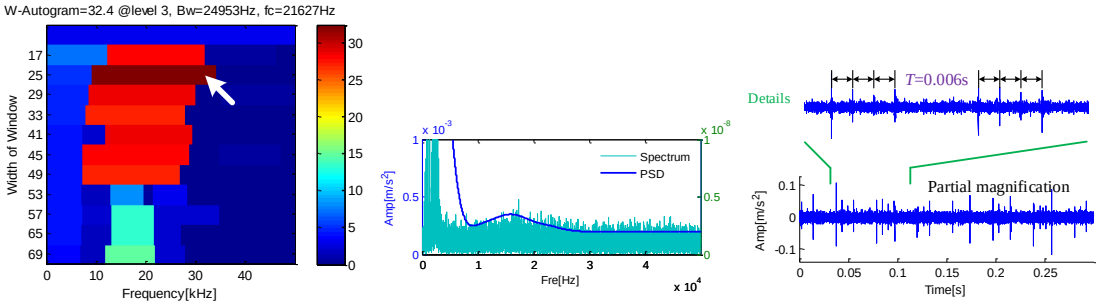

(a) W-Autogram (b) PSD (c) The component with maximum WAC

Fig.4.20 The results decomposed by W-Autogram.

Finally, the computational efficiency of EWT, Fast Kurtogram and W-Autogram is calculated. Fig.4.21 shows that Fast Kurtogram is very fast. The W-Autogram proposed in this article takes 19.9425s, which is far lower than the original EWT method.

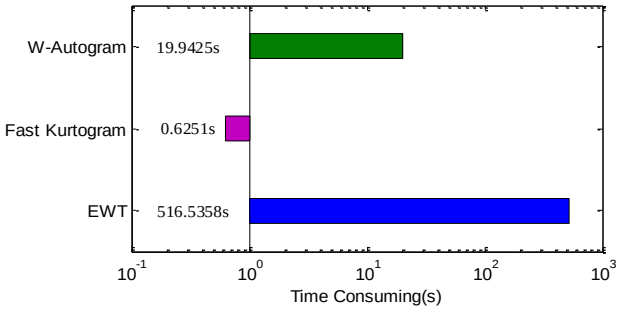

Fig.4.21 Time consuming of EWT, Fast Kurtogram and W-Autogram.

4.4.4.2 Analysis of Bearing inner Ring Fault Data

The bearing outer ring fault data and its Fourier spectrum are shown in Fig.4.22. The interference such as noise is strong, and there is no obvious pulse in the waveform. In the Fourier spectrum, the amplitudes of the signals in the entire frequency band are similar. There are no significant harmonics in the envelope spectrum. The frequency band containing the fault

information is masked by strong noise.

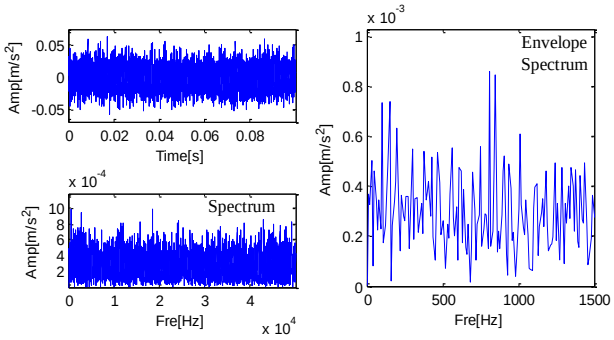

Fig.4.22 The outer ring fault data, its spectrum and its envelope spectrum.

The signal is processed by Fast Kurtogram, the results are shown in Fig.4.23a. The component with the highest kurtosis is located at Level 5, the seventh component from the left. The center frequency is 10156 Hz and the bandwidth is 1563. Fig.4.23b is the waveform of this component, and Fig.4.23c is the envelope spectrum of the component. The width of the frequency band is small, and the extracted components exhibit the characteristics of an AM signal. 100 Hz can be found in the envelope spectrum, but there are no harmonics.

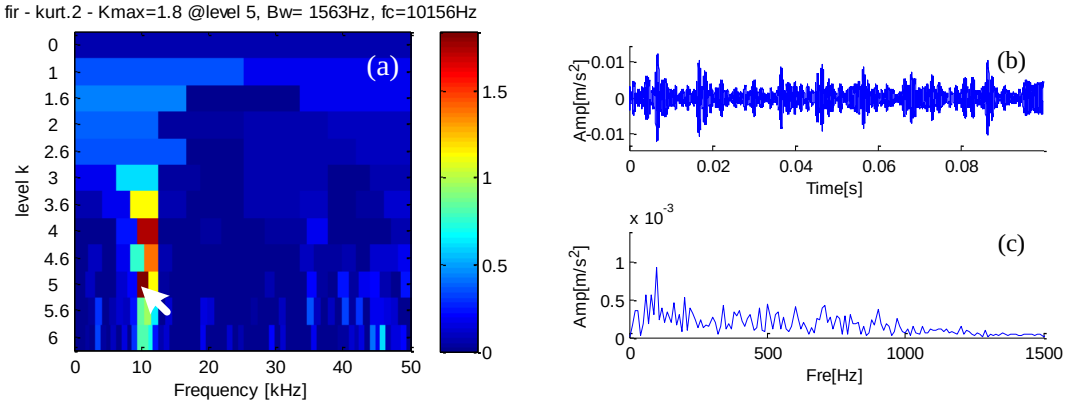

Fig.4.23 The results decomposed by Fast Kurtogram: (a) Fast Kurtogram; (b) The component with maximum Kurtosis; (c) Envelope spectrum of the component.

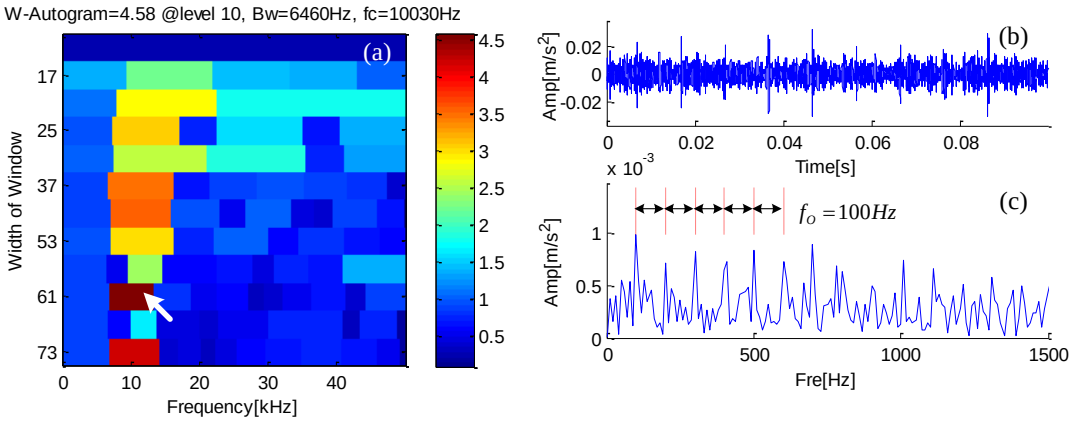

Fig.4.24 The results decomposed by W-Autogram: (a) W-Autogram; (b) The component with maximum WAC; (c) Envelope spectrum of the component.

The signal was processed by W-Autogram; the results are shown in Fig.4.24a. The component with the largest WAC is located at Level 10, the window width is 61, the center frequency is 10030 Hz, and the bandwidth is 6460 Hz. Fig. 4.24b is the waveform of this

component. There are periodic pulses in the waveform of the component, and the period of the pulses is 0.01s, which is the same as the failure period of the bearing outer ring. Fig. 4.24c is its envelope spectrum. There is obvious fault characteristic frequency and harmonics in the envelope spectrum. The method proposed in this paper can effectively extract the fault information in the signal of the bearing outer ring. Compared with Fast Kurtogram, the W-Autogram method proposed in this paper can collect more fault information.

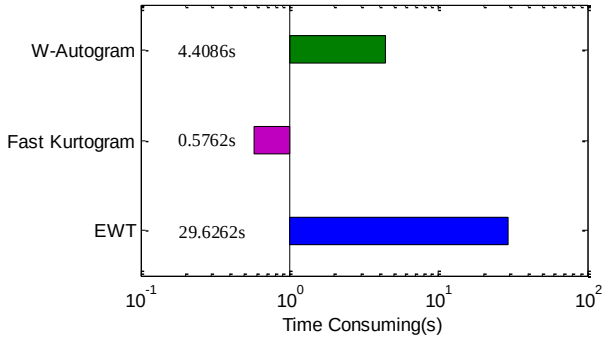

Fig.4.25 Time consuming of EWT, Fast Kurtogram and W-Autogram.

Finally, the computational efficiency of EWT, Fast Kurtogram and W-Autogram is calculated. Fig. 4.25 shows W-Autogram proposed in this article takes 4.4086s, which is far lower than the original EWT method.

4.5 The proposed Harmonic spectral kurtosis and its application in the multilevel spectral segmentation framework

When rotating machinery, especially bearings or gears, are damaged, periodic pulse signals will appear, which is the most important basis for detecting faults. In a noise-free or weak noise environment, the time-domain waveform characteristics of the fault signal include pulses and their periodicity, which are easy to be visually recognized. When the fault signal contains noise or other interference, the pulse in the fault signal is buried, and scholars can find the fault characteristics in the frequency domain. Although the fault information of the bearing inner ring or outer ring exists in the full spectrum, most of the energy is concentrated near the natural frequency. Noise is likely to conceal fault information far away from the natural frequency. Ideally, the single-level decomposition method can divide the signal into several uncorrelated components, and one of them may contain the most fault information. Envelope analysis of this component may realize the visual display of the fault information in the envelope spectrum. In order to quantify the fault information in the envelope spectrum, this section proposed Harmonic spectral kurtosis, which is sensitive to periodic pulse information, based on the theory of Spectral kurtosis.

4.5.1 Theory of harmonic spectral kurtosis

The stationary process described in Frequency domain Wold-Cramer decomposition is:

$$y(t) = \int_{-\infty}^{+\infty} e^{j2\pi ft} G(f) d_{X(f)} \tag{4.26}$$

where $G(f)$ is the Hilbert transform of $g(t)$, $d_{X(f)}$ is the spectral process of signal $x(t)$:

$$x(t) = \int_{-\infty}^{+\infty} e^{j2\pi ft} d_{X(f)} \tag{4.27}$$

Antoni summarizes the non-stationary signal by adding time-varying information:

$$y(t) = \int_{-\infty}^{t} g(t, t-\tau) x(\tau) d_{\tau} \tag{4.28}$$

Its frequency counterpart is:

$$y(t) = \int_{-\infty}^{+\infty} e^{j2\pi ft} P(t,f) d_{X(f)} \tag{4.29}$$

where $P(t,f)$ can be interpreted as the complex envelope or complex demodulate of $y(t)$ at f.

Subsequently, the randomized cyclostationary processes can be described as:

$$g(t,s) = g(t+T,s) = \sum_k g_k(s) e^{j2\pi kt/T} \tag{4.30}$$

where $g(t,s)$ is the periodic function of time.

Define the 2n-order instantaneous moment as:

$$S_{2nY}(t,f) = E\left\{\left|P(t,f)d_{X(f)}\right|^{2n}\right\}/d_f = |P(t,f)|^{2n} \cdot S_{2nX} \tag{4.31}$$

2n-order instantaneous moment can measure the energy intensity of the complex envelope at t and f. $S_{2nY}(t,f)$ can also be called the instantaneous spectrum or time-frequency energy density of $y(t)$. Let $n = 1$, its spectral moments are:

$$S_{2Y}(f) = E\{S_{2Y}(t,f)\} = E\left\{\left|P(t,f)d_{X(f)}\right|^{2}\right\}/d_f = E\{|P(t,f)|^2\} \cdot S_{2X} \tag{4.32}$$

When characterizing the conditionally non-stationary process, define 2n-order average moment:

$$\langle S_{2Y}(t,f)\rangle_t = \lim_{T\to\infty} 1/T \int_{-T/2}^{T/2} S_{2Y}(t,f) d_t = S_{2Y}(f) \tag{4.33}$$

Similarly, instantaneous moment of characteristic time can be defined:

$$g_0(t,\Delta t) = \sum_n g_n(nt) e^{j2\pi nt/T} \tag{4.34}$$

where $g_0(t,\Delta t)$ is a function that may have periodic instantaneous pulses intercepted in the area $(-\Delta t, \Delta t)$ near nt of $g(t,s)$. Define the 2n-order harmonic instantaneous moment as:

$$S_{2HY}(t,f) = E\left\{\left|P_n(t,f)d_{X(f)}\right|^{2}\right\}/d_f = |P_n(t,f)|^2 \cdot S_{2X} \tag{4.35}$$

$S_{2HY}(t,f)$ can measure the local energy intensity of the complex envelope at t and f. Its spectral moments are:

$$S_{2HY}(f) = E\{S_{2HY}(t,f)\} = E\left\{\left|P_n(t,f)d_{X(f)}\right|^{2}\right\}/d_f = E\{|P_n(t,f)|^2\} \cdot S_{2X} \tag{4.36}$$

2n-order harmonic average moment can be described as:

$$\langle S_{2HY}(t,f)\rangle_t = \lim_{T\to\infty} 1/T \int_{-T/2}^{T/2} S_{2HY}(t,f) d_t = S_{2HY}(f) \tag{4.37}$$

The normalized fourth-order harmonic spectral moment of $y(t)$ can be defined as:

$$C_{4HY}(f) = S_{4HY}(f); f \neq 0 \tag{4.38}$$

Harmonic Spectral Kurtosis (HSK) is defined as the energy-normalised fourth-order harmonic spectral cumulant:

$$HSK_Y(f) = \frac{C_{4HY}(f)}{S_{2Y}^2(f)} = \frac{S_{4HY}(f)}{S_{2Y}^2(f)}; f \neq 0 \tag{4.39}$$

HSK can not only suppress the interference of single pulse, random noise, and modulation information, but also is sensitive to the fault information of the bearing inner ring and outer ring. If the bearing of the equipment is damaged, the fault characteristic frequency of the bearing inner ring or outer ring and its harmonics may appear in the envelope spectrum of the vibration signal, which can be found in Fig.4.26. There are periodic pulses of similar amplitude in the waveform of the fault signal of the outer ring of the bearing, and periodic pulses of amplitude modulation in the fault signal of the inner ring. This is the biggest difference between the two fault characteristics in the time domain waveform. The spectrum of the two types of fault signals includes the center frequency and bandwidth, and the fault information covers the entire spectrum. In general, the fault characteristic frequency of the inner ring of the bearing is higher than that of the outer ring. The envelope spectrum of the outer ring fault signal has outer

ring fault characteristic frequencies and harmonics; the inner ring fault signal has characteristic frequencies, harmonics and sidebands.

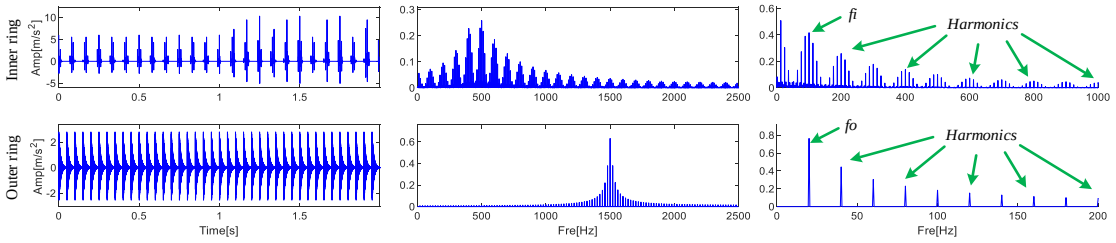

(a) Signal (b) Spectra (c) Envelope spectra

Fig.4.26 The fault simulation signal, spectra and envelope spectra of the inner ring and outer ring of the rolling bearing.

Commonly used envelope demodulation diagnosis methods need to observe whether there are fault characteristics and harmonics in the envelope spectrum, which means that the observed results will be affected by their amplitudes. For the multi-level decomposition method, the signal is usually accumulatively decomposed into dozens of components. It is time-consuming and unreasonable to judge each envelope spectrum by observation. If a certain frequency and its possible harmonics are superimposed or multiplied, the total energy of the characteristic frequency and its harmonics will appear in the new spectrum. Fig.4.27 extracts 62.5Hz, 90Hz and 100Hz and their several multiples from the envelope spectrum of the above-mentioned inner circle signal and displays them in the new spectrum. Obviously, when the extracted frequency is related to fault information, the energy of the new spectrum is higher. When the extracted frequency is related to noise, the energy is lower. When processing signals containing noise or other interference, the above-mentioned precise extraction methods are difficult to achieve the desired effect. The characteristic frequency of the bearing inner ring or outer ring fault may be deviated during the calculation process, and even a small deviation may cause the final energy to be weakened, as shown in the green part in Fig.4.27.

HSK extracts the instantaneous moment of characteristic of the envelope spectrum as shown in Fig.4.28. The preset characteristic frequency range and its harmonics are extracted and formed into new samples, the fault information is retained, and the noise part is discarded. It can be theoretically said that useful information will be amplified and useless information such as noise will be suppressed, which means that the proposed HSK is insensitive to interference information that does not have periodic pulse characteristics such as noise. For the envelope spectrum of noise, the difference between the mean value and the peak value of the instantaneous moment of characteristic obtained by HSK is very small, and there will be no periodic pulses. Similarly, there is no similar bearing fault information in the envelope spectrum of single pulse and modulation information.

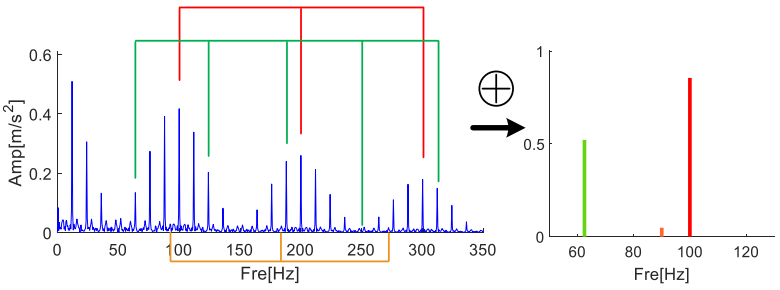

Fig.4.27 Extract 62.5Hz, 90Hz, 100Hz and several harmonics of the envelope spectrum of the signal, show their energy in the new spectrum

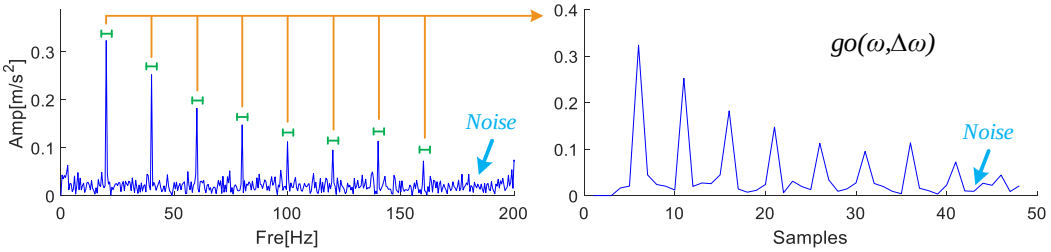

(a) Envelope spectrum of bearing outer ring fault data (b) Instantaneous moment of characteristic

Fig.4.28 Instantaneous moment of characteristic of envelope spectrum obtained by HSK

If the above-mentioned bearing inner ring and outer ring fault simulation data are combined, the waveform, spectrum and envelope spectrum can be found in Fig.4.29. The envelope spectrum of the compound faults is complex, which may include the rotation frequency, the characteristic frequency of the outer ring fault and its harmonics, the characteristic frequency of the inner ring fault and its harmonics and sidebands. The fusion of all frequency information will bring difficulties to visual discrimination. HSK can separate the instantaneous moment of characteristics of the inner ring and outer ring in the envelope spectrum.

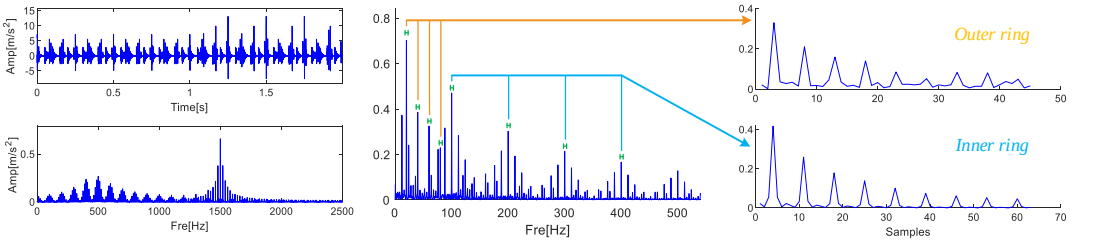

(a) Superimposed signal and its spectrum (b) Envelope spectrum (c) Instantaneous moment of characteristic of inner/outer ring

Fig.4.29 Separate the inner ring and outer ring fault information in compound faults by HSK

4.5.2 Basic properties of harmonic spectral kurtosis

It is difficult to predict whether the collected signal contains fault information or the type of interference information. The characteristic information of the equipment during normal operation, the characteristic information of faulty components, and strong environmental noise are likely to be hidden in the signal. Even if the device is not damaged, it may be severely disturbed by the outside world. For example, the collision between materials and the device, and the contact between tools and the device may be collected and recorded by the sensor. Random single pulses will bring great trouble to fault diagnosis, especially in the current index system even if the pulse energy is very weak. In order to simulate several of information that may exist in the normal operation of the equipment, several simulation signals are designed in this section.

$$\begin{cases} s_A = 5\cos(2\pi \cdot 100t) \\ s_B = 5\cos(2\pi \cdot 4t) \times \cos(2\pi \cdot 500t) \\ s_C = 150e^{-g_1 \times 2\pi f_{n1}^i t} \times \sin\left(2\pi f_{n1}^i t \times \sqrt{1-g_1{}^2}\right) \\ s_D = 5\sin(2\pi \cdot 35t) \times \sin(2\pi \cdot 2500t + \sin(2\pi \cdot 100t)) \\ \quad +0.8\cos(2\pi \cdot 2t) \times \cos(2\pi \cdot 50t) \\ s_E = \sum_{i=1}^{M} 14e^{-g_2 \times 2\pi f_{n2}^i t} \times \sin\left(2\pi f_{n2}^i t \times \sqrt{1-g_2{}^2}\right) \\ s_F = \text{Noise}(SNR = 10dB) \\ s = s_A + s_B + s_C + s_D + s_E + s_F \end{cases} \tag{4.40}$$

where the nature frequency is $f_{n1} = 1500$ Hz, $f_{n2} = 3500$ Hz. The damping coefficient $g_1 = 0.1$, $g_2 = 0.02$, the repetition period of the periodic pulses is $T = 0.01$ s. Component A is a

cosine at 100 Hz with amplitude of 5; Component B is a modulation signal; Component C is a single pulse with a center frequency of 1500 Hz; Component D is interference information with a center frequency of 2500 Hz and a bandwidth of 35 Hz; Component E is the periodic pulses with a center frequency of 3500 Hz and a bandwidth of 100 Hz; Component F is random noise. The waveforms, spectra and envelope spectra are shown in Fig.4.30.

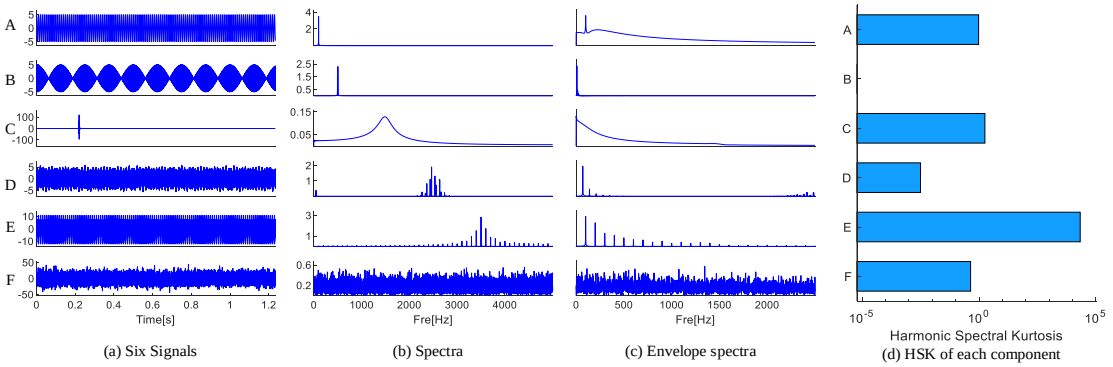

Fig.4.30 Sensitivity of harmonic spectrum kurtosis to different components

The spectrum of A is a single pulse, so that the kurtosis of A calculated from the frequency domain may be similar to the result of C calculated from the time domain. The energy in the envelope spectrum is so low that it can hardly display any useful information. The spectrum of B is two single pulses close to each other, which will have a higher amplitude component in the envelope spectrum, but there is no frequency doubling information. The spectrum of single pulse C is a curve with very low amplitude, which is difficult to find in the superimposed signal but exists. There are no characteristic frequencies or harmonics in the envelope spectrum of C, and it is an attenuation curve. C is sensitive to many indicators. The spectrum of D is similar to that of periodic pulses, but the center frequency is missing, and there may be fault characteristic frequencies in the envelope spectrum. These contents may bring troubles to the direct observation method, but its frequency is often smaller than the fault characteristic frequency, and the harmonic information is weak. There are center frequencies and several sidebands in the spectrum of E, and there are characteristic frequencies and harmonics in the envelope spectrum. The SNR of the noise F is -5dB, and there may be random pulses in the time domain. The noise is all over the whole spectrum, and there is no obvious characteristic on the envelope spectrum. To calculate the HSK of these six components, please pay attention to the abscissa of Fig.4.30. When the signal has periodic pulse characteristics, the value of HSK will be very high, and the HSK of the other components will be very small.

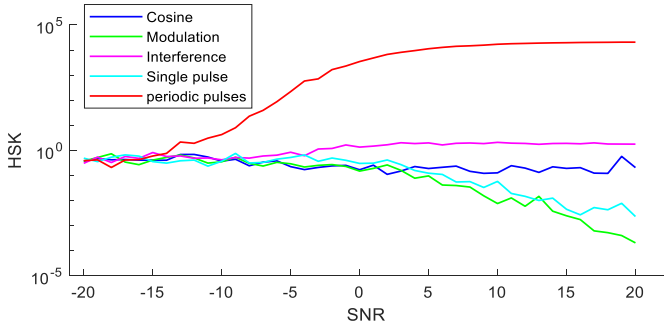

Fig.4.31 Add different intensities of noise to the components

In order to verify the HSK anti-noise ability, we added noise with a SNR of [-20dB, 20dB] to the above five simulated signals. Fig.4.31 shows the HSK of the five components in different

SNR situations. When SNR is higher than -14 dB, HSK is more sensitive to periodic pulses than other interferences. When the SNR is lower than -14dB, the sensitivity of the HSK is reduced or even failure information may not be extracted. Of course, the environmental noise is difficult to reach -14 dB, this extreme environment needs to be discussed in follow-up research. Therefore, it can be concluded that the HSK's anti-noise ability is excellent, and theoretically it can realize the fault feature extraction in the application.

4.5.3 Multi-level spectral segmentation method: Harmogram

The signal usually contains lots of unknown information, and the fault information is also hidden in it. The multi-level spectral segmentation method can freely divide the spectrum according to the characteristics of the signal and obtain the corresponding center frequency and bandwidth. The core of the multi-level decomposition method is to find a resonant frequency band for the band-pass filtering process to enhance the weak bearing fault signal in the envelope spectrum. Since it is inevitable that the signal contains interference or noise, and both noise and fault information exist in the high frequency and low frequency bands at the same time, it is the core of Harmogram to extract the frequency band that contains more fault information and less noise through a band-pass filter. Therefore, the multi-level decomposition method has become the main direction of the application of HSK in this article. In this paper, the Fourier transform function of the spectrum is used to extract the trend component inversely as the basis for separating the spectrum. By changing the conditions of the inverse transformation, the trend components of different fluctuation levels can be stacked to form a tower-shaped boundary distribution diagram, which is the basic content of Harmogram. Fig.4.32 shows the flowchart of Harmogram.

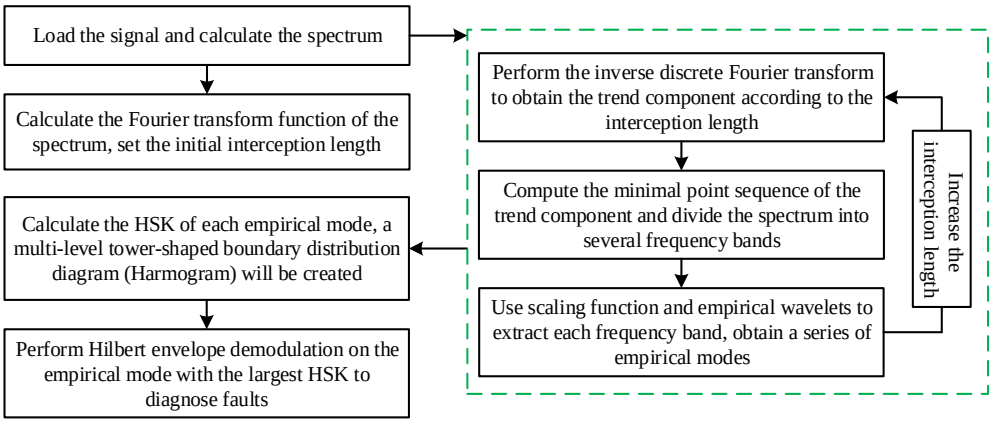

Fig.4.32 The flowcharts of Harmogram.

The main steps of Harmogram are shown as follows:

Step 1: Collect the fault data and calculate the Fourier transform of the spectrum, set the initial interception length.

Step 2: Perform the inverse discrete Fourier transform on the intercepted Fourier transform function of the spectrum according to the interception length; the trend component will be obtained which would be used to calculate the minimum sequence that are regarded as boundaries used to divide the spectrum.

Step 3: Applying scaling function and empirical wavelets to process the center frequency and bandwidth of each frequency band, a low-pass filter and a set of band-pass filters will be obtained, and each filter will extract a component.

Step 4: Increase the interception length and repeat steps 2 to 3. A multi-level tower-shaped boundary distribution diagram will be created.

Step 5: Harmonic spectral kurtosis will be calculated for the envelope spectrum of each empirical mode. A new Harmogram can be constructed to identify periodic pulse information in the signal.

4.5.4 Comparison of index performance in multi-level decomposition methods

The multi-level decomposition method can provide more choices for the screening process of various indicators, noise and interference have the opportunity to be discarded, and useful information can be retained with greater probability. This section uses the Harmogram to obtain the tower-shaped boundary distribution diagram and verify the advantages of HSK. Superimpose the components A-E into a new signal and add three levels of noise to it: -3dB/-5dB/-7dB. When the noise intensity is -3dB, the time-domain waveform and spectrum can be found in Fig.10. There is a single pulse with very high amplitude in the waveform, which is located at 1500Hz on the spectrum. The periodic pulse information representing the fault is located at 3500 Hz on the spectrum. The core and purpose of the multi-level decomposition method is to successfully extract Part E in Fig.4.33.

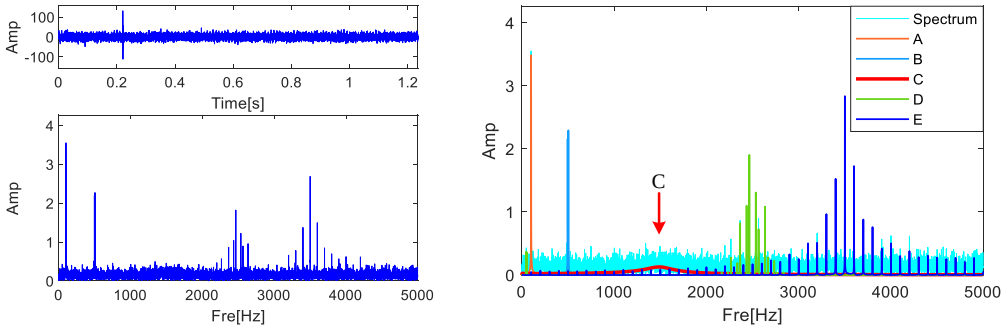

(a)Signal and its spectrum (b) The spectrum of each component

Fig.4.33 Superimposed signal and spectrum

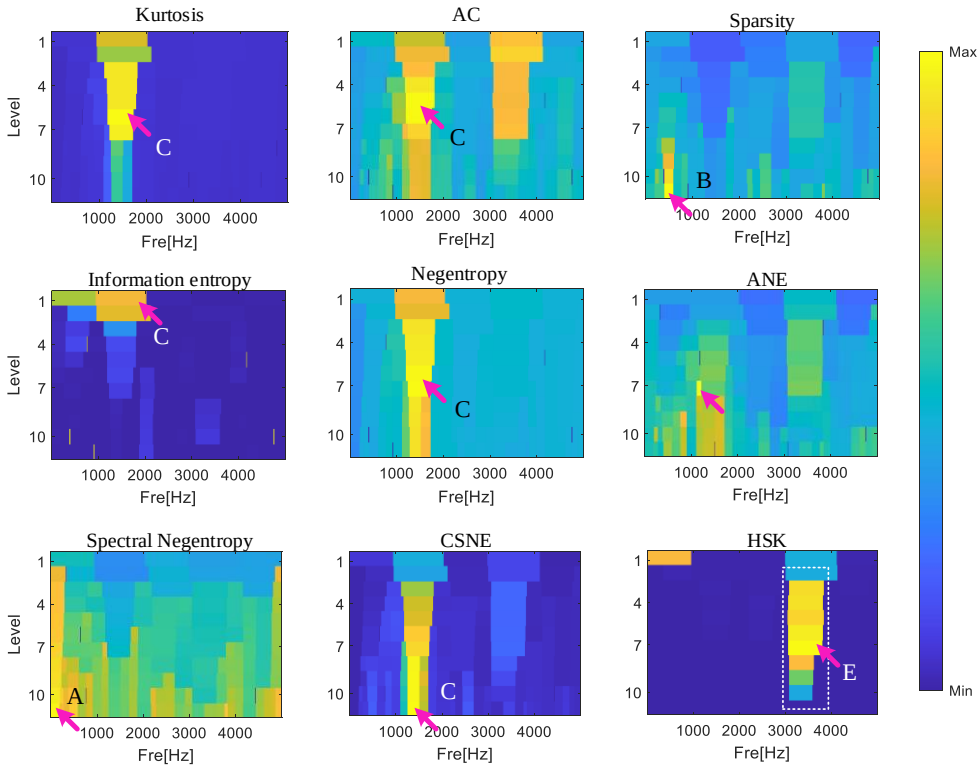

Fig.4.34 Results of screening using different indicators under the Harmogram framework

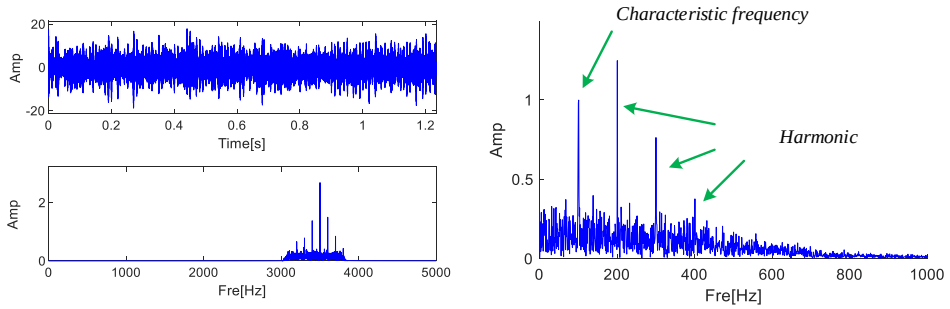

(a)Component of the frequency band selected by HSK and its spectrum (b)Envelope spectrum

Fig.4.35 Component of the frequency band selected by HSK

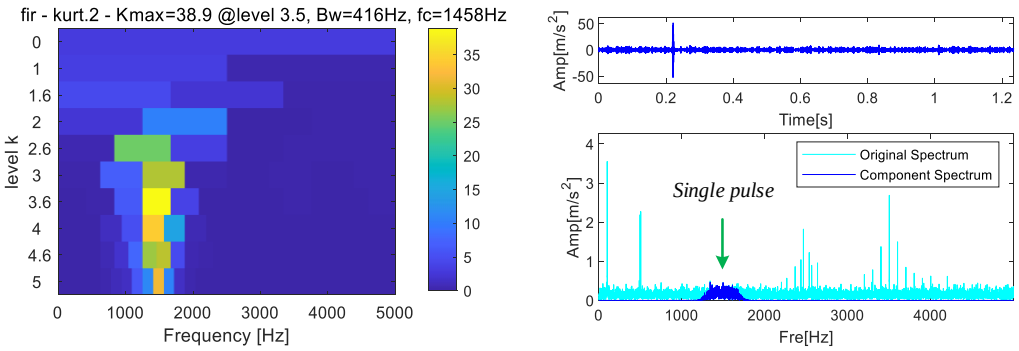

(a) FIR based Fast Kurtogram (b) Spectrum

Fig.4.36 Results decomposed by Fast Kurtogram

Some excellent indicators are used to verify the superiority of HSK: Kurtosis, the kurtosis of the unbiased Autocorrelation of the squared envelope of the demodulated signal (AC), Sparsity, Information Entropy (IE), Negentropy (NE), AC×NE (ANE), Spectral Negentropy (SNE) and Correlation SNE (CSNE) are used to calculate the components in the Harmogram. Fig.4.34 shows the results of screening using different indicators under the Harmogram framework. Kurtosis is sensitive to the single pulse at 1500 Hz, and other components are almost ignored. AC can resist the interference of a single pulse in the case of weak noise, but cannot resist the temptation of a single pulse in the case of strong noise. Sparsity focuses on the location of the modulation information. Both IE and NE are more sensitive to single pulses. ANE cannot resist interference in narrow frequency bands. Although SNE avoids the pulse in the time domain, it cannot avoid the interference of the information of "pulse in the frequency domain and cosine in the time domain". CSNE still does not solve the interference of single pulse to the indicator. The screening results of 9 indicators show that only HSK successfully locates the center frequency near 3500 Hz. The maximum HSK of Level 3-8 is in this frequency band. HSK=759.1, the bandwidth is 730Hz. In theory, 7 sidebands can be intercepted, which is helpful for subsequent envelope analysis. The waveform, spectrum, and envelope spectrum of this component are shown in Fig.4.35. The envelope spectrum contains characteristic frequencies with higher peaks and their harmonics.

If Fast Kurtogram is used to process the signal, the result is shown in Fig.4.36a. The signal is decomposed into 9 levels. The component with the largest Kurtosis is located at the center frequency of 1458 Hz and the bandwidth is 416 Hz. Because Kurtosis is sensitive to single pulses, periodic pulse information at 3500 Hz cannot be located. Although the energy of a single pulse in the frequency spectrum is very low, the result is still disturbed by it. Fig.4.36b shows the comparison between the spectrum of the component with the greatest kurtosis and the original spectrum. The four visually distinguishable components are not recognized, and the

visually difficult single pulse is recognized. Since the 3500Hz component has not been extracted, the envelope spectrum is not shown here because it is meaningless. Fast Kurtogram may recognize a signal containing only a single pulse as a fault.

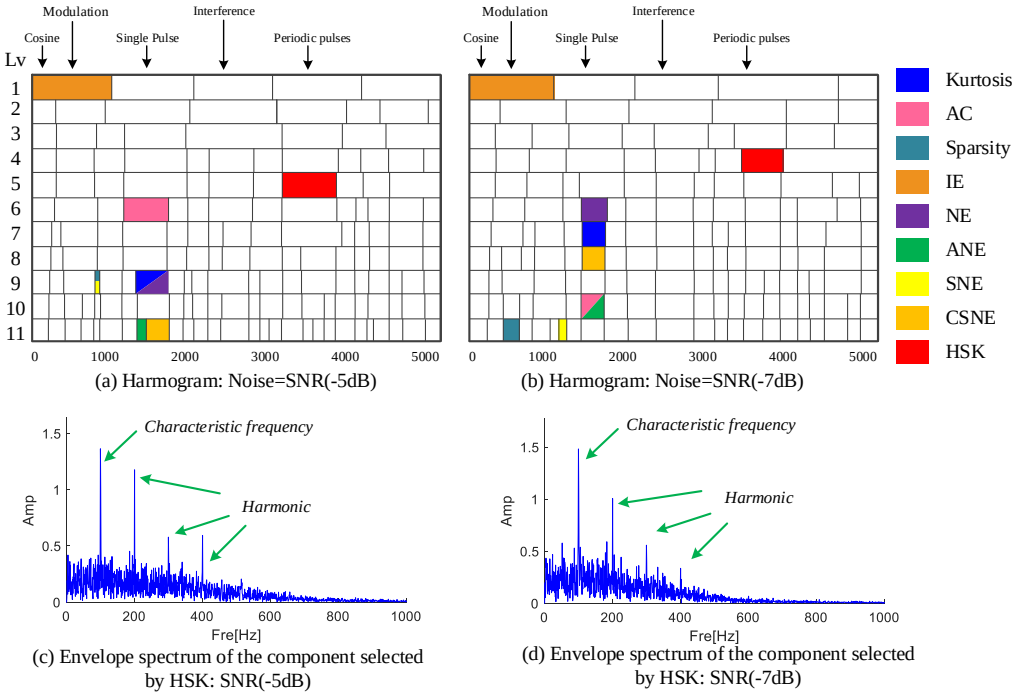

(a) Harmogram: Noise=SNR(-5dB)

(b) Harmogram: Noise=SNR(-7dB)

(c) Envelope spectrum of the component selected by HSK: SNR(-5dB)

(d) Envelope spectrum of the component selected by HSK: SNR(-7dB)

Fig.4.37 Results of screening using different indicators under the Harmogram framework with Noise=SNR(-5dB or -7dB)

Increase the noise intensity and repeat the above experiment. The Harmogram-based decomposition method divides the signal into 11 groups. In order to show the processing results of each indicator under two noise intensities of -5dB and -7dB, Fig.4.37a-b uses different colors to mark the location of the maximum value of each indicator. Among them, Kurtosis is blue and HSK is red. When the noise intensity is SNR=-5dB, Kurtosis/AC/NE/ANE/CSNE all recognize the single pulse, and only HSK recognizes the periodic pulse. When the noise intensity is SNR=-7dB, the same five indicators as before can identify single pulses, and only HSK can identify periodic pulses. Calculate the envelope spectrum of the frequency band obtained by HSK. When the noise intensity is -5dB, the characteristic frequency and its harmonics can be found from Fig.4.37c, and the fault characteristics are obvious. When the noise intensity is -7dB, the characteristic frequency and its harmonics can be found from Fig.4.37d, and the fault characteristics are obvious.

Fig.4.38a is the processing result of Fast Kurtogram; the signal is decomposed into 9 levels. The component with the largest Kurtosis is located at the center frequency of 1458 Hz and the bandwidth is 416 Hz. The multi-level decomposition process is concentrated around 1500 Hz where there is a single pulse. Even if the noise intensity has increased to -5dB, the single pulse still has a great influence on the results of Fast Kurtogram. Fig.4.38c is the processing result of Fast Kurtogram; the signal is decomposed into 9 levels. The component with the largest Kurtosis is located at the center frequency of 1484 Hz and the bandwidth is 156 Hz. The multi-level decomposition process is also concentrated around 1500 Hz where there is a single pulse. When the noise intensity is -7dB, the single pulse still has a great influence on the result of Fast Kurtogram. Therefore, the HSK proposed in this paper can avoid the interference of single pulse and modulation information in both strong and weak noise conditions. The more

reasonable multi-level decomposition results obtained by the Harmogram proposed in this paper also provide convenience for noise reduction.

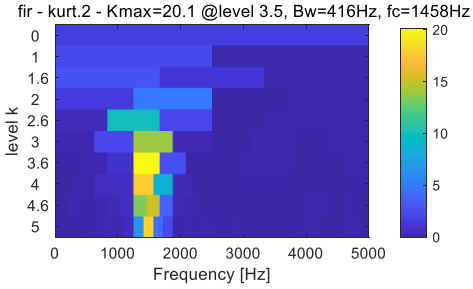

(a) FIR based Fast Kurtogram

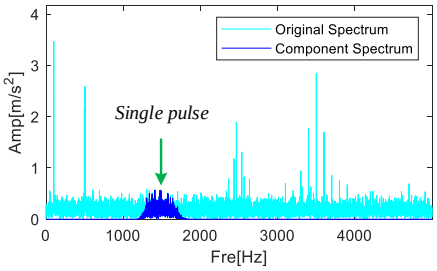

(b) Spectrum

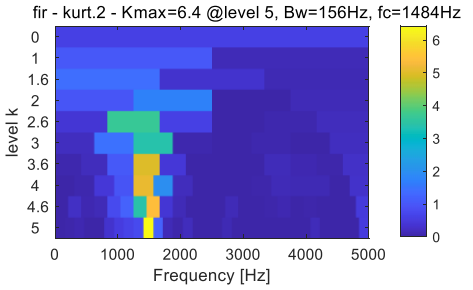

(c) FIR based Fast Kurtogram

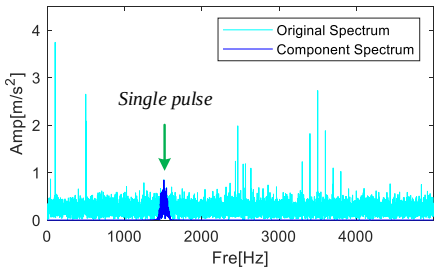

(d) Spectrum

Fig.4.38 Results decomposed by Fast Kurtogram with Noise=SNR(-5dB or -7dB)

4.5.5 Application

4.5.5.1 Bearing outer ring fault data

This experiment uses the fault bearing test data collected by the laboratory of Xi'an Jiaotong University. The Spectra Quest, Inc test bench is shown in Fig.4.39a. The rated speed of the motor is 2850r/min, the number of rotor slots is 34, and the number of stator slots is 24. After calculation, the fault characteristic frequency of the outer ring of the bearing is $f_q = 76$ Hz. Fig.4.39b shows the collected signal and its spectrum. There are many pulses in the waveform but its periodicity cannot be judged. In the spectrum, the amplitude of the part whose frequency is lower than 1000 Hz is large, and the amplitude of other frequency bands is very low. It is difficult to find the center frequency and sidebands of the fault information from it. In addition, there is no obvious characteristic frequency of bearing outer ring fault or inner ring fault characteristic frequency in the envelope spectrum.

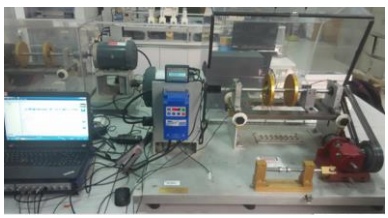

(a) The Spectra Quest, Inc test bench

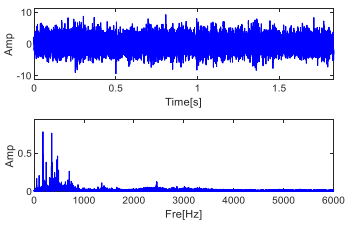

(b) Signal and Spectrum

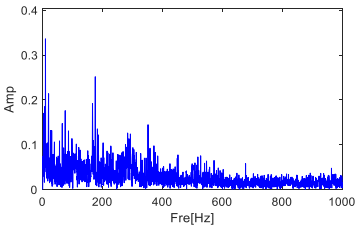

(c) Envelope Spectrum

Fig.4.39 The Spectra Quest, Inc test bench.

Using Harmogram to process the signal, 11 sets of signals will be obtained by the multi-level decomposition method. After calculating the HSK of each component, the tower-shaped boundary distribution diagram is drawn as shown in Fig.4.40a. The component with the largest HSK is located at Level 3, with a center frequency of 5341.5 Hz and a bandwidth of 599 Hz. The HSK changes of all the components of Level 3 are shown in Fig.4.40b. The spectrum is

divided into 7 frequency bands at Level 3, of which the 6th frequency band has the largest HSK. The components of this frequency band are extracted, and the waveform and envelope spectrum are shown in Fig.4.40c. The characteristic frequency and harmonics can be found, which means that there is a bearing outer ring fault in the signal. The proposed HSK is sensitive to periodic pulses, and Harmogram can be applied to the fault diagnosis of the bearing outer ring.

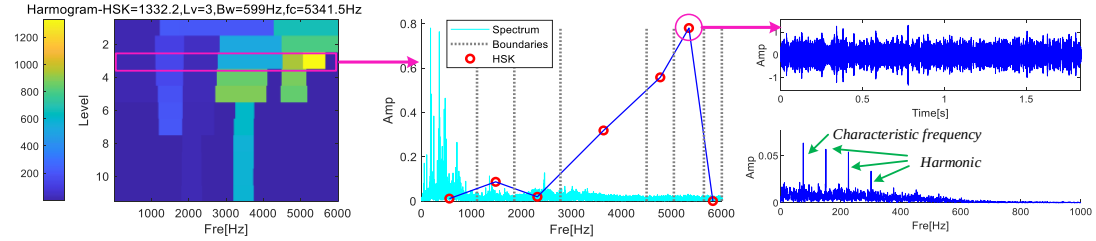

(a) Harmogram (b) The distribution of Boundaries and HSK (c) Component and its envelope spectrum

Fig.4.40 The boundaries distribution and envelope spectrum corresponding to the component with the largest HSK in the Harmogram

Fast Kurtogram based on FIR and Fast Kurtogram based on STFT are used to process the signal. The center frequency of both methods is around 1500 Hz. Fast Kurtogram based on FIR has obtained 9 levels, the component with the largest kurtosis is located in the 9th frequency band of Level 5, Kurtosis=2.5. The center frequency is 1593 Hz, and the bandwidth is 187 Hz. Due to the narrow bandwidth, even if the position of the center frequency is correct, the narrow frequency band cannot contain more than 3 sidebands, which means that it is difficult to obtain more periodic pulse information, and there are almost no harmonics in the envelope spectrum. A similar situation also appears in the STFT-based Fast Kurtogram. 7 Levels will be obtained, the component with the largest kurtosis is located in the 9th band of Level 6, Kurtosis=2.6. The center frequency is 1500Hz. The same narrow bandwidth will result in the absence of harmonics in the envelope spectrum, which can be observed in Fig.4.41b.

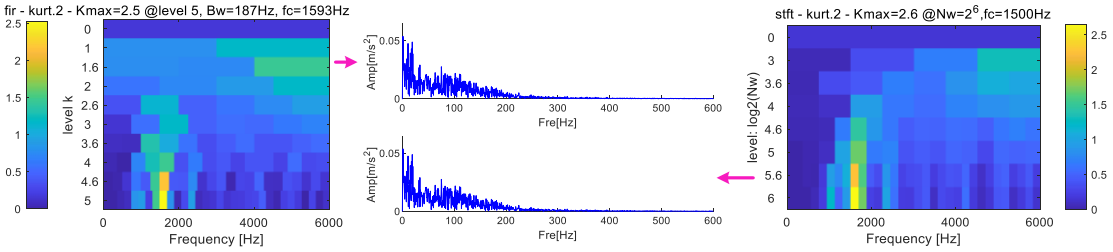

(a) Fast Kurtogram-FIR (b) Envelope spectra (c) Fast Kurtogram-STFT

Fig.4.41 Fast Kurtogram processing results based on FIR and STFT and the envelope spectrum of the component with the largest Kurtosis

4.5.5.2 Bearing inner ring fault data

This section adopts the signal of the inner ring fault of the cement mill main motor bearing. The cement tube mill is fed at a rate of 200 tons/hour, and a JS150B reducer is used between the motor and the mill, as shown in Fig.4.42. The bearing on the load side of the motor is SKF 23048CC.C3W33.

The number of rollers is 27, the characteristic frequency of cage failure is f_{ca}=5.64Hz, the characteristic frequency of roller failure is f_b=62.886Hz; the characteristic frequency of outer ring failure is f_o=152.31Hz; the characteristic frequency of loop fault is f_i=185.19Hz. The rotation frequency is 12.5 Hz, and the sampling frequency is 22050 Hz. There is a characteristic frequency of the inner ring fault in the envelope spectrum, but there is only one harmonic(Fig.4.43).

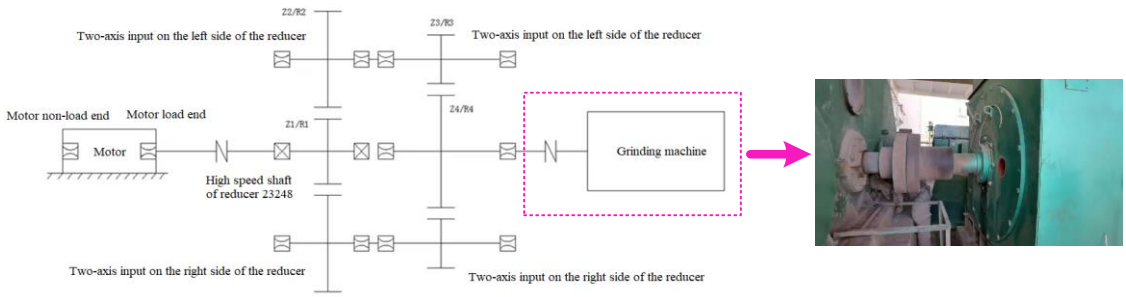

Fig.4.42 JS150B reducer structure diagram

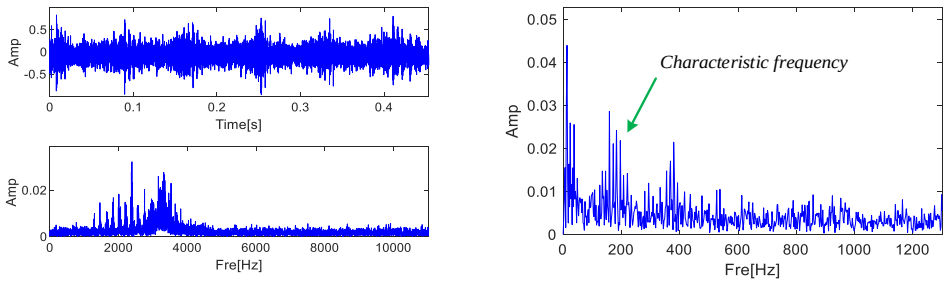

(a) Signal and Spectrum (b) Envelope Spectrum

Fig.4.43 Waveform, spectrum and envelope spectrum of the collected signal

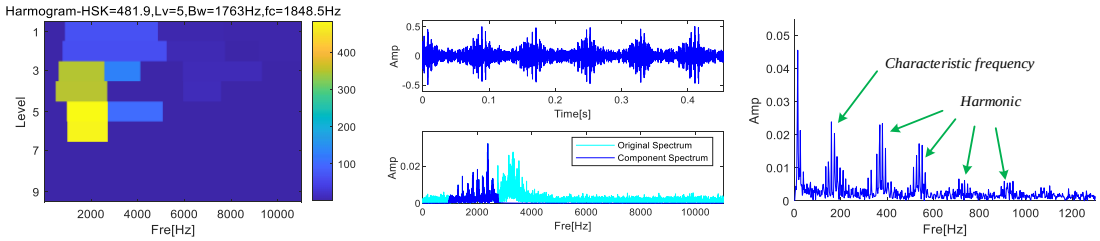

(a) Harmogram (b) Component and its spectrum (c) Envelope spectrum

Fig.4.44 Harmogram processing results and the component with the largest HSK, its spectrum and envelope spectrum

Using Harmogram to process the signal, 9 groups of signals will be obtained. After calculating the HSK of each component, the tower-shaped boundary distribution diagram is drawn as shown in Fig.4.44a. The component with the largest HSK is located at Level 5; with a center frequency of 1848.5 Hz and a bandwidth of 1763 Hz. Fig.4.44b shows the waveform and spectrum of the component corresponding to the largest HSK. Six periodic pulse information and modulation information appear in the waveform. The intercepted part may not contain all the fault information, but it contains a lot of fault information. Therefore, the characteristic frequency and harmonics can be found in the envelope spectrum of Fig.4.44c, which means that there is a bearing inner ring fault in the signal. HSK is sensitive to periodic pulses, and the proposed Harmogram can be applied to the fault diagnosis of the bearing inner ring.

Fast Kurtogram based on FIR and Fast Kurtogram based on STFT was used to process the signal. The center frequency of both methods is located near 2067 Hz. The Fast Kurtogram based on FIR has obtained 11 levels, and the component with the largest kurtosis is located in the fifth frequency band of Level 4.6, Kurtosis=0.4. The bandwidth is 459Hz. There are fault characteristic frequencies and a harmonic in the envelope spectrum. In the STFT-based Fast Kurtogram, 11 Levels will be obtained, and the component with the largest kurtosis is located in the 7th band of Level 5.6, Kurtosis=0.5. The center frequency is 2067Hz. There are fault characteristic frequencies in the envelope spectrum, which can be observed in Fig.4.45b.

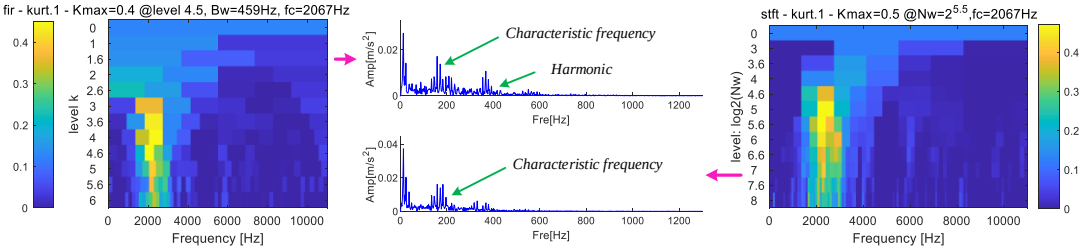

(a) Fast Kurtogram-FIR (b) Envelope spectra (c) Fast Kurtogram-STFT

Fig.4.45 The envelope spectra of the components with the largest Kurtosis among the two Fast Kurtogram processing results

An excellent algorithm called Autogram will be used to process this complex signal. Autogram uses the characteristics of wavelet transform, and its spectrum segmentation framework is similar to Fast Kurtogram. At the same time, Autogram applies the maximal overlap discrete wavelet packet transform to make the result have a good filtering effect. Autogram can decompose the signal into 5 levels. The largest value was obtained in the 4th level. Extracting the information in this frequency band, the waveform and envelope spectrum are shown in Fig.4.46. It can be found that the envelope spectrum is almost the same as Fig.4.45b, and cannot reach the energy intensity of Fig.4.44c.

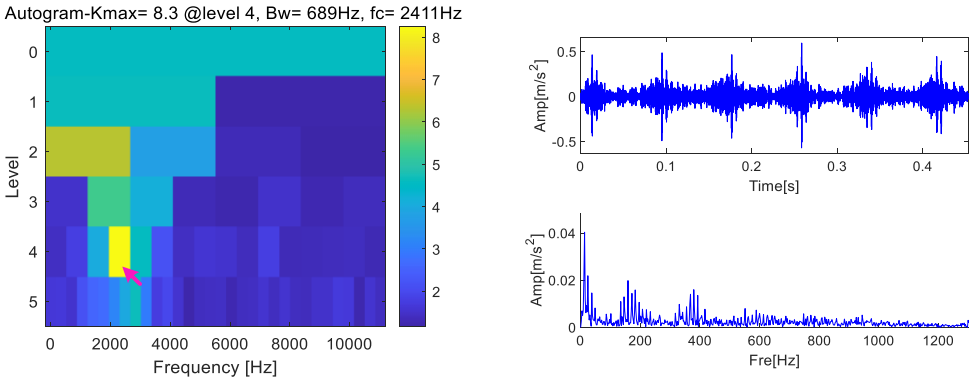

(a) Autogram (b) Component and its envelope spectrum

Fig.4.46 The 5-level spectral segmentation results obtained by Autogram and the obtained component and its envelope spectrum

4.5.5.3 Bearing compound fault data

The experimental data used in this experiment are from Shanghai Jiao Tong University. The bearing fault simulator is shown in Fig.2.28. Fig.4.47 shows the waveform, frequency spectrum and envelope spectrum of the signal. Due to the actual length of the acquisition, the components in the waveform are more complicated. Because the bearing is predicted to be a compound fault, there are bearing inner ring fault information and outer ring fault information in the signal. In addition, there is a strong pulse at 16s. After calculating the envelope spectrum of the signal, it can be found that although the noise intensity is very weak, the amplitude of the rotation frequency is very high. The rotation frequency and its multiplication bring difficulties to the judgment of the fault. Even if the characteristic frequency of the bearing inner ring fault and its harmonics can be found, the frequency is equal to the multiplier of the rotating frequency. It is impossible to determine whether the frequency is a continuation of the multiplier of the rotating frequency, and it is not certain that the bearing inner ring is faulty. In addition, the fault characteristics of the outer ring of the bearing are difficult to find, and the fault information is hidden.

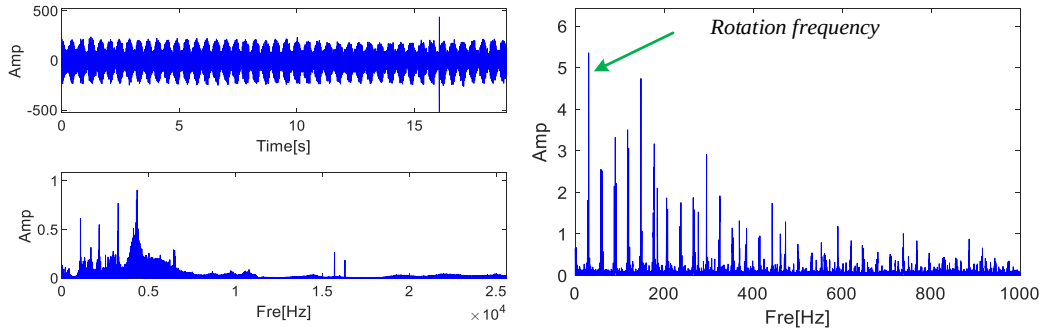

(a) Signal and spectrum (b) Envelope spectrum

Fig.4.47 Waveform, spectrum and envelope spectrum of the collected signal

Processing the signal under the framework of Harmogram and decomposing it in multiple levels, 9 sets of boundary distribution patterns can be obtained. In order to diagnose whether there is a bearing inner ring or outer ring fault in the signal, the HSK can be calculated on the basis of f_o and f_i to draw the distribution of two HSKs, which is shown in Fig.4.48. Extract the component corresponding to the largest HSK and perform envelope demodulation on it, and the fault information can be judged. When f_o is used to calculate HSK, the tower-shaped boundary distribution diagram drawn is shown in Fig.4.48a. Component with the largest HSK is located at Level 9; with a center frequency of 10877.5 Hz and a bandwidth of 1489 Hz. Fig.4.48b shows the waveform and spectrum of the component corresponding to the largest HSK. Although there is a single pulse in the waveform, its amplitude is lower than the original. It can be found from the spectrum that the energy of the extracted frequency band is lower. It can be found in the envelope spectrum of Fig.4.48c that the characteristic frequency of the bearing outer ring f_o=92Hz and its harmonics, which means that there is a bearing outer ring fault in the signal. When f_i is used to calculate HSK, the tower-shaped boundary distribution map drawn is as shown in Fig.4.48d. The component with the largest HSK is located at Level 4; with a center frequency of 22159 Hz and a bandwidth of 3020 Hz. Fig.4.48e shows the waveform and spectrum of the component corresponding to the largest HSK. This frequency band belongs to high frequency information, and the energy of the extracted frequency band is relatively low. It can be found in the envelope spectrum of Fig.4.48f that the characteristic frequency of the bearing inner ring is f_i=148.6Hz and harmonics, which means that there is a fault in the bearing inner ring in this signal. Although the rotation frequency exists in the two envelope spectra, its amplitude is very low and does not affect the fault diagnosis. There is also a single pulse in the waveform and its amplitude is high, indicating that the natural frequency of the pulse is very close to the natural frequency of the inner ring fault. The results show that the proposed HSK is sensitive to periodic pulses, and the proposed Harmogram can be applied to the compound fault diagnosis of the inner and outer rings of bearings.

Fast Kurtogram based on FIR and Fast Kurtogram based on STFT was used to process the signal (Fig.4.49). The Fast Kurtogram based on FIR has obtained 9 levels, and the component with the largest kurtosis is located in the fifth frequency band of Level 2.6, with a center frequency of 19200 Hz, Kurtosis=852.9, and a bandwidth of 4266 Hz. There are single pulses with higher amplitude in the extracted components, and the characteristic frequencies and harmonics of the bearing inner ring fault in the envelope spectrum, which are similar to Fig.4.48f. This method can successfully extract the inner ring fault in the signal, but cannot capture the outer ring fault information.

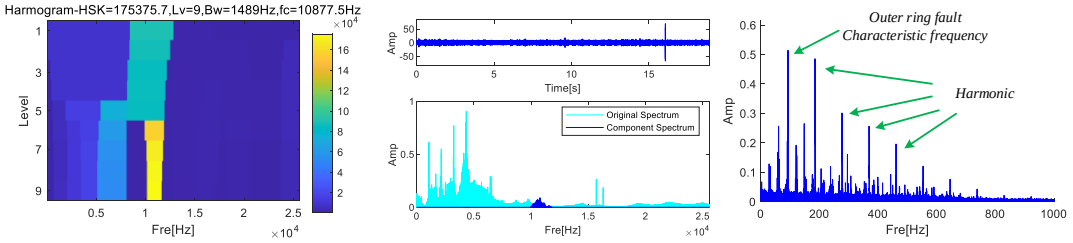

(a) Harmogram (b) Component and its spectrum (c) Envelope spectrum

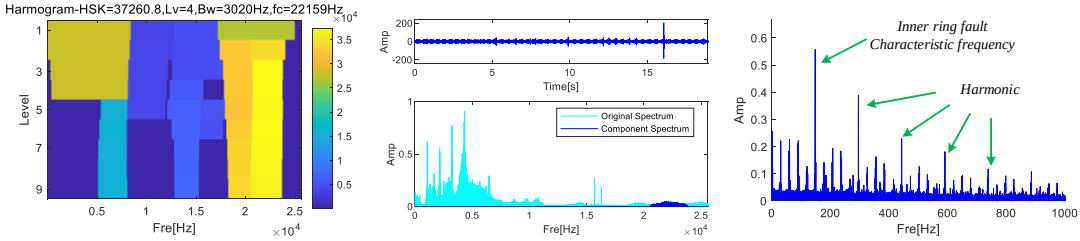

(d) Harmogram (e) Component and its spectrum (f) Envelope spectrum

Fig.4.48 The results obtained by Harmogram based on the characteristic frequencies of inner and outer ring faults respectively

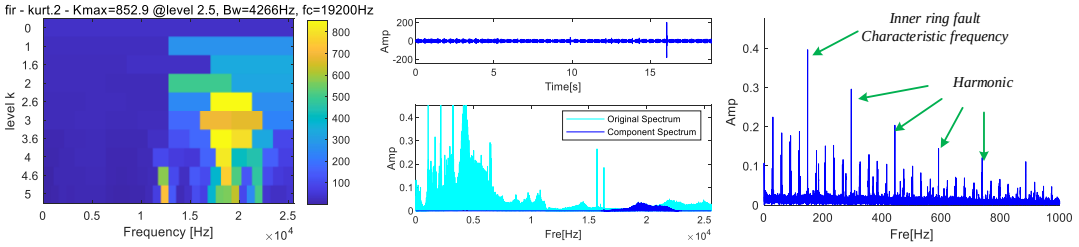

(a) Fast Kurtogram-FIR (b) Component and its spectrum (c) Envelope spectrum

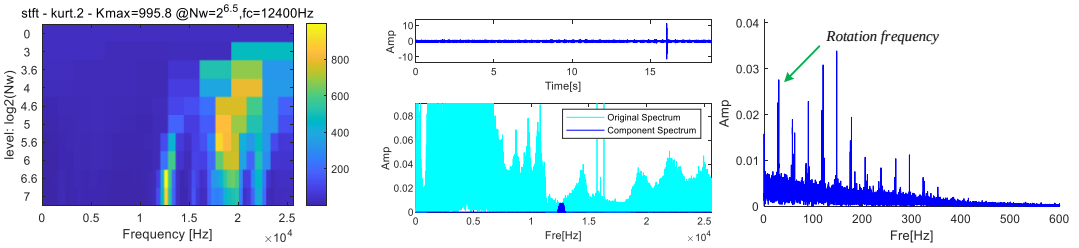

(d) Fast Kurtogram-STFT (e) Component and its spectrum (f) Envelope spectrum

Fig.4.49 The result obtained by Fast Kurtogram and the component with the maximum kurtosis, its spectrum and envelope spectrum

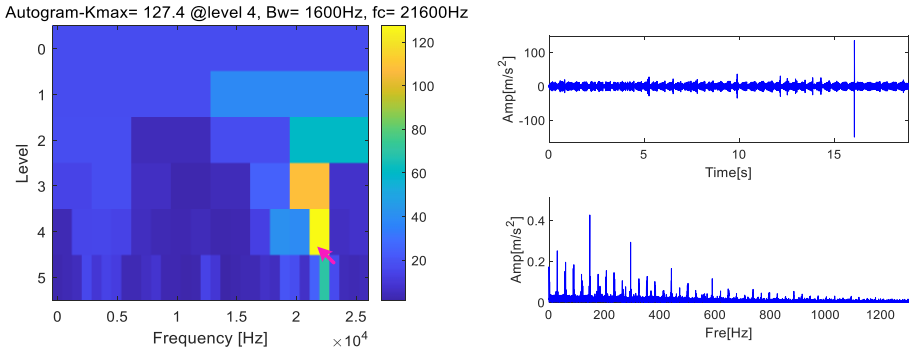

(a) Autogram (b) Component and its envelope spectrum

Fig.4.50 Autogram and the obtained component and its envelope spectrum

In the STFT-based Fast Kurtogram, 9 levels will be obtained, the component with the largest kurtosis is located at Level 6.6, the center frequency is 12400Hz, and Kurtosis=995.8. There is a single pulse in the extracted components, and there is a rotation frequency in the

envelope spectrum, but there is no fault characteristic of the bearing inner ring or outer ring. The results of Autogram are shown in Fig.4.50. It can be found that in the entire frame, only the frequency band around 21600 Hz has a larger value, and there is no distinctive value around 10877 Hz where the bearing outer ring fault exists. The frequency band with a center frequency of 21600 Hz and a bandwidth of 1600 Hz is extracted, and its time-domain waveform and envelope spectrum are shown as Fig.4.50b. The inner ring fault is easy to find, but the outer ring fault characteristics are still buried. In the process of bearing compound fault diagnosis, the proposed HSK and Harmogram are advantageous and effective.

4.6 Conclusion

In this chapter, two concise spectral segmentation methods based on power spectral density are proposed to optimize the empirical wavelet transform and improve the computational efficiency and accuracy.

(a) The method based on variable spectral segmentation empirical wavelet transform (VEWT) uses the extreme points of Multi-taper PSD to simplifies the Fourier spectrum and reduces the number of extreme points. The bandwidth obtained by the expansion algorithm designed on the basis of LMF contains less noise. VEWT is more advantageous for the decomposition of signals containing noise. At last, the MIT-BIH Arrhythmia Database is used to verify that VEWT is effective.

(b) The adaptive and concise empirical wavelet transform (ACEWT) that used to reduces the original method's excessive dependence on extreme points was proposed. Simulated signals verified that the proposed method can extract different components in complex signals. The proposed weight unbiased autocorrelation was significantly better than other indicators in a strong noise environment, and the resistance to random pulses in noise was greatly increased. So it is more sensitive to periodic pulses that represent faults in rotating machinery. In order to expand the application of ACEWT, W-Autogram is proposed. The impact of narrow bandwidth bands on indicators was reduced. The fault data of bearing inner and outer rings verified the effectiveness of the proposed method.

(c) Harmonic spectral kurtosis (HSK) with strong anti-noise ability and anti-single pulse interference to detect periodic pulses was proposed. HSK can accurately extract the harmonic information in the envelope spectrum, quantify the periodic pulses, and suppress the influence of interference such as random pulses. Harmogram with HSK not only optimizes the spectral segmentation method, but also obtains a better center frequency and bandwidth. The filtered frequency band can contain more periodic pulse information. The proposed method has greater advantages in decomposing signals containing noise. The simulation signal shows that the proposed method is accurate and effective. The data of bearing inner ring, outer ring and compound faults prove that the method can be applied to bearing fault diagnosis.

Chapter 5
Quaternion-based multi-channel signal fusion method and its application in bearing fault diagnosis[113]

5.1 Introduction

In this chapter, quaternion analytical mode decomposition (QAMD) method is proposed to process multiple acoustic signals and extract fault information in industrial machinery systems with high sampling frequency, low speed, and heavy load. QAMD can separate characteristic information from frequency domain and extend it to the fault diagnosis of rotating industrial machinery. The multi-signal fusion method based on quaternion can process multiple sets of longer digital signals at the same time, which provides a new idea for the synchronous processing of big data. The proposed quaternion Fourier trend spectral segmentation method can not only automatically obtain bisecting frequencies and divide the signal into several frequency bands, but also realize the fusion and modal decomposition of multiple sets of digital signals in frequency domain. Experimental results show that the proposed method can effectively extract useful information from acoustic signals and apply it to bearing fault diagnosis.

5.2 Proposed quaternion analytical mode decomposition

Since time domain decomposition methods are prone to modal aliasing or end effects, frequency domain decomposition methods have gained more and more development. This paper proposes the Spectrum segmentation method based on quaternion Fourier spectrum trend on the basis of previous research. The quaternion analytical mode decomposition (QAMD) proposed in this chapter is dedicated to the simultaneous analysis and frequency domain fusion of multiple sets of acoustic signals to finally achieve modal decomposition. First, a multi-group signals fusion method based on quaternion is proposed, which realizes the synchronous analysis of three groups of related signals. Secondly, a spectral segmentation method based on quaternion Fourier spectral trend is proposed, which realizes the adaptive acquisition of the bisection frequency. For the calculation method of trend spectrum, please refer to Eq.3.3-3.5. For the extraction of analytical mode, please refer to Eq.2.10-2.18.

5.2.1 Multiple signal fusion method based on quaternion

With the development of sensors, multi-channel data synchronous acquisition technology and multi-group signal asynchronous acquisition technology have been developed. Relevant big data storage technology enables signals to be stored in large quantities and for a long time. As the sensitivity of the collector is increased, a large amount of detailed information is stored in the signal. This information may be useless noise, or it may contain details of the fault information. The length of the weak fault of low-speed and heavy-duty data is very long, and the periodic vibration details are hidden in it. Therefore, multi-data or multi-sensor signal fusion is helpful to extract weak fault information in the signal. This section uses a quaternion method to fuse multiple sets of data signals.

Hamiltonian [118] proposed a complex number containing one real part and three imaginary parts and named it a quaternion. Quaternion is a four-dimensional normed division algebra belonging to hyper-complex subgroup which can be described as [119]:

$$Q = a + bi + cj + dk \in \mathbb{H} \tag{5.1}$$

where $\mathrm{a}, \mathrm{b}, \mathrm{c}, \mathrm{d} \in \mathbb{R}$ and $\mathrm{i}, \mathrm{j}, \mathrm{k}$ are imaginary units which have special properties such as the

multiplication rules among them:

$$i^2 = j^2 = k^2 = ijk = -1 \tag{5.2}$$

$$ij = -ji = k, jk = -kj = i, ki = -ik = j \tag{5.3}$$

Since the product of quaternions is non-commutative, it is difficult to calculate using quaternions. In order to achieve the fusion of quaternion signals, this method uses the quaternion Fourier transform proposed by Ell [120]. QFT is an extension of classical Fourier transform which can be used to process signals with three or four-dimensional samples. The 1D right-sided QFT of a quaternion-valued signal f(t) is:

$$F^R(\omega) = \kappa_1 \int_{-\infty}^{\infty} f(t) e^{\mp \mu \omega t} dt \tag{5.4}$$

where $-\mu$ represents the forward transform, on the contrary, $+\mu$ is the reverse transform, which is distinct from their inverse transforms given by Eq.5.5:

$$f(t) = \kappa_2 \int_{-\infty}^{\infty} F^R(\omega) e^{\pm \mu \omega t} d\omega \tag{5.5}$$

where $F^R(\omega)$ is spectrum of f(t) which are functions of quaternion value. μ is a unit pure quaternion and it is not only a norm version of quaternion, but also can be described as the rotating axis of quaternion:

$$\mu = \frac{a}{\sqrt{a^2+b^2+c^2}} i + \frac{b}{\sqrt{a^2+b^2+c^2}} j + \frac{c}{\sqrt{a^2+b^2+c^2}} k \tag{5.6}$$

The scale coefficient satisfies: $\kappa_1 \kappa_2 = (2\pi)^{-1}$. When $\kappa_1 = \kappa_2$, this transformation is a unitary transformation. The 1D left-sided QFT and its inverse of a quaternion-valued signal f(t) can be given by:

$$F^L(\omega) = \kappa_- \int_{-\infty}^{\infty} e^{\mp \mu \omega t} f(t) dt \tag{5.7}$$

$$f(t) = \kappa_+ \int_{-\infty}^{\infty} e^{\pm \mu \omega t} F^L(\omega) d\omega \tag{5.8}$$

Due to the particularity of quaternion, the fusion among the imaginary parts is very difficult. To solve this problem, Sangwine [121] proposed discrete quaternion Fourier transform (DQFT) and applied it to color image processing and treat the color space of a point in color image as a whole vector with quaternion. However, it is not only enormous but also inconvenient to compute according to the formula of DQFT due to the non-commutatively of quaternion product. So quaternion fast Fourier transform (QFFT) [122] was proposed to take advantage of decomposing the original operation into two traditional complex Fourier transforms and use the existing fast Fourier transform to compute QFT.

Assuming that the quaternion represented in the standard basis $\{1, i, j, k\}$ is $q = a + bi + cj + dk$, then a new basis $B = \{1, \mu_1, \mu_2, \mu_1\mu_2\}$ was given which can be expressed as:.

$$B = \begin{pmatrix} \mu_{1i} & \mu_{1j} & \mu_{1k} \\ \mu_{2i} & \mu_{2j} & \mu_{2k} \\ \mu_{3i} & \mu_{3j} & \mu_{3k} \end{pmatrix} \tag{5.9}$$

The four numerical components of the quaternion represented on the new basis are:

$$\begin{cases} a' = a \\ b' = \langle a + bi + cj + dk, \mu_1 \rangle \\ c' = \langle a + bi + cj + dk, \mu_2 \rangle \\ d' = \langle a + bi + cj + dk, \mu_3 \rangle \end{cases} \tag{5.10}$$

where $\langle \cdot \rangle$ represents the scalar product and $\mu_3 = \mu_1\mu_2 = V(\mu_1) \times V(\mu_2)$.

After changing the basis, the quaternion signal can be used as two complex signals:

$$\begin{cases} z_1 = a' + b'I \\ z_2 = c' + d'I \end{cases} \tag{5.11}$$

where I represents complex root of -1. Thanks to the linear properties of Fourier transform, QFT can be decomposed into the sum of two complex Fourier transforms:

$$F(u) = \sum_{n=1}^{N} e^{-\mu 2\pi \frac{nu}{N}}(a' + b'\mu_1 + c'\mu_2 + d'\mu_3)$$
$$= \sum_{n=1}^{N} e^{-\mu 2\pi \frac{nu}{N}}(a' + b'\mu_1) + \sum_{n=1}^{N} e^{-\mu 2\pi \frac{nu}{N}}(c' + d'\mu_1)\mu_2 \quad (5.12)$$

The core of this section is to fuse multi-channel signals or multiple sets of related signals into the same quaternion signal. Constructing quaternion Fourier spectrum on the basis of QFT can provide a more concise objective function for spectrum segmentation. In order to demonstrate the multiple signal fusion method based on quaternion, this section constructs a simulated signal that has three channels. X-channel and Z-channel are interferences that contain modulation information. The center frequency of X-channel is 1000Hz, and the center frequency of Z-channel is 4000Hz. Y-channel is a periodic pulse that simulates the failure of the outer ring of a bearing, with a center frequency of 2500 Hz.

$$\begin{cases} X(t) = 2\sin(2\pi \cdot 50t) \times \sin(2\pi \cdot 1000t + \sin(2\pi \cdot 100t)) \\ Y(t) = \sum_{i=1}^{M} 6e^{-g \times 2\pi f_n^i t} \times \sin\left(2\pi f_n^i t \times \sqrt{1-g^2}\right) \\ Z(t) = 2\sin(2\pi \cdot 50t) \times \sin(2\pi \cdot 4000t + \sin(2\pi \cdot 100t)) \end{cases} \quad (5.13)$$

where $M = 10$, damping coefficient $g = 0.07$, the period of the pulse is 0.01s. In addition, the signals of the three channels have been added with noise with a signal-to-noise ratio of 10dB.

In order to demonstrate the characteristics of the quaternion Fourier transform, the center frequencies of the three channel signals in the frequency domain are set to be far away from each other. It can be seen from Fig.5.1 that the signals are successfully fused in the frequency domain. The details of each signal are preserved in the new quaternion Fourier spectrum.

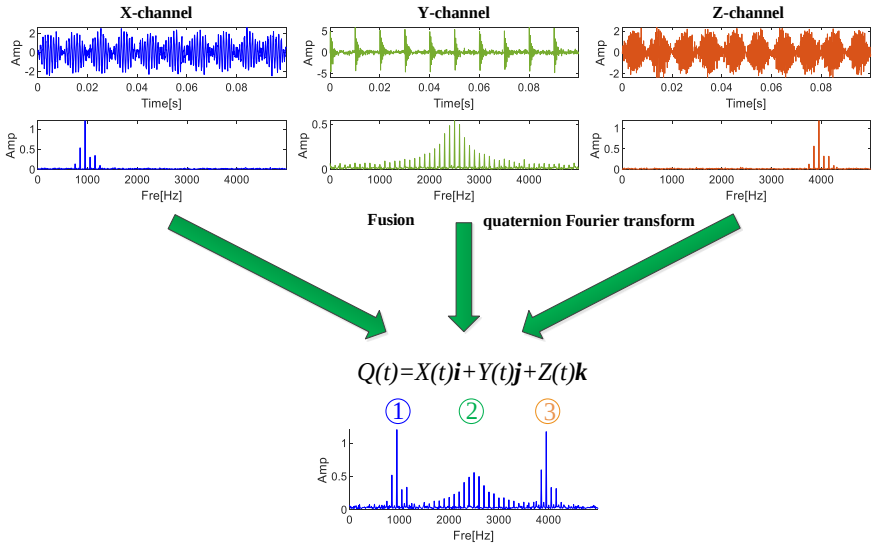

Fig.5.1 Multiple signal fusion method based on quaternion

5.2.2 The calculation process of the QAMD algorithm

The flowcharts are shown in Fig.5.2 and the steps of QAMD are shown as follows:

i. Collect signals through multiple or multi-channel synchronization
ii. Fuse multiple sets of data into a set of quaternion signal
iii. Perform the quaternion Fourier transform to calculate the Fourier spectrum of the fused quaternion signal
iv. Calculate the trend component of the quaternion Fourier spectrum by the Fourier transform of the spectrum
v. Define the minimum points of the trend spectrum as boundaries to divide the quaternion Fourier spectrum
vi. Set the boundary to the bisecting frequency, and perform modal decomposition

iteratively to obtain several components

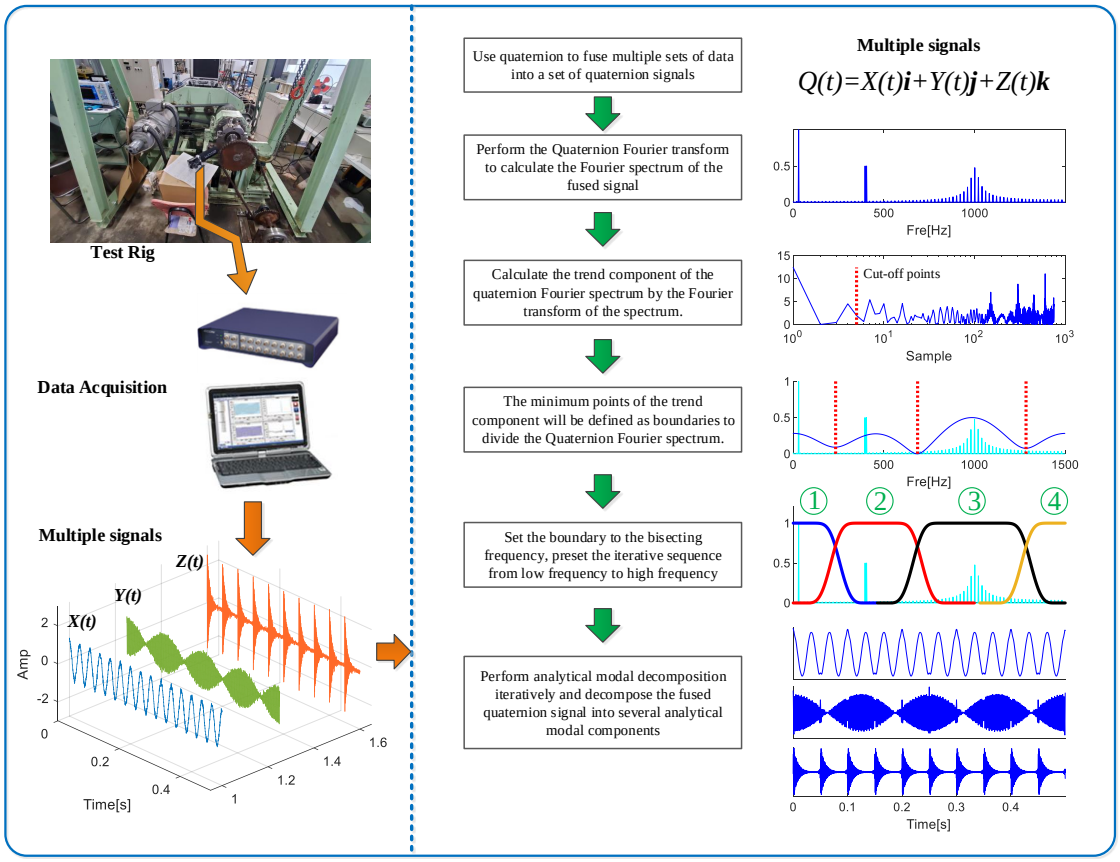

Fig.5.2 The flowcharts of QAMD.

5.3 Verification

5.3.1 Simulation signal verification

In order to show the details and advantages of the multi-channel/multi-group acoustic signal decomposition method proposed in this article, this section designs a set of three-channel simulation signals. It is assumed that the signal contains low-frequency or high-frequency modulation information for normal bearing operation. At the same time, assume that some other interference and noise exist. Fig.5.3a shows the four components mentioned above with different amplitudes, different center frequencies, and different frequency bands. Due to the high frequency of the signal, [0.1s-0.15s] is intercepted here to show the details of each component. Fig.5.3b is the Fourier spectrum of each component. The center frequency of S1 is 1000 Hz, S2 is 4000 Hz, S3 is 2400 Hz, and S4 is 2500 Hz.

It is worth mentioning that in some cases, not all three channels have obvious fault characteristics. Some channels or time-collected signals contain a small amount of fault information, and some channels contain a large amount of fault information. In some special cases, there is almost no fault information. In view of this, this section constructs three-channel simulation based on these components. X-Channel contains a large amount of S1 and a small amount of S4; Y-Channel contains a small amount of S4 and a large amount of S2; Z-Channel contains S1 and S3, which means there is no fault information.

$$\begin{cases} s_X = 6\sin(2\pi\cdot 40t)\times\sin(2\pi\cdot 1000t+\sin(2\pi\cdot 100t)) \\ \quad +\sum_{i=1}^{M} 6e^{-g\times 2\pi f_n^i t}\times\sin\left(2\pi f_n^i t\times\sqrt{1-g^2}\right) \\ s_Y = 4.5\sin(2\pi\cdot 40t)\times\sin(2\pi\cdot 4000t+\sin(2\pi\cdot 100t)) \\ \quad +\sum_{i=1}^{M} 6e^{-g\times 2\pi f_n^i t}\times\sin\left(2\pi f_n^i t\times\sqrt{1-g^2}\right) \\ s_Z = 2\sin(2\pi\cdot 40t)\times\sin(2\pi\cdot 1000t+\sin(2\pi\cdot 100t)) \\ \quad +\cos(2\pi\cdot 2400t) \end{cases} \tag{5.14}$$

where the nature frequency $f_n = 2400$ Hz. The damping coefficient $g = 0.07$, the repetition period of the periodic pulses is $T = 0.01$ s.

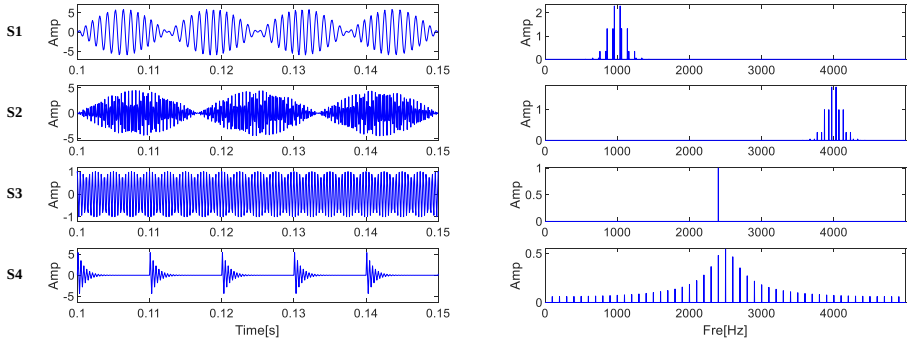

(a) Waveforms of four components (b) Fourier spectrum of each component

Fig.5.3 Four basic components used to construct three-channel signals

The waveforms contain a lot of noise, and the periodicity of the fault is difficult to recognize. It can be vaguely determined from the Fourier spectrum that the fault information may exist at 1000Hz, 2500Hz or 4000Hz, because there are center frequencies and sidebands in them, and its shape is similar to S4 in Fig.5.3b. According to Eq.5.14, the fault information is actually located at 2500 Hz, the sideband is 100 Hz, and the characteristic frequency is 100 Hz. The other two frequency bands are interference information. Directly calculate the envelope spectrum of the three sets of data as shown in Fig.5.4c. The characteristic frequency of X-Channel and Z-Channel is 80Hz, and the characteristic frequency of Y-Channel is 60Hz, both of which are different from the fault characteristic frequency. Therefore, the preset modulation information successfully concealed the fault information in the signal. Fig.5.5 shows the details of X-Channel and Y-Channel. The frequency band [2000Hz-3000Hz] is amplified. In the Fourier spectrum of these two channels, several pulses with an interval of 100 Hz can be found, which contains faults. In order to strip the fault information in the signal from the interference and noise, the common method is to divide the spectrum, and then calculate the envelope spectrum of the components in each frequency band.

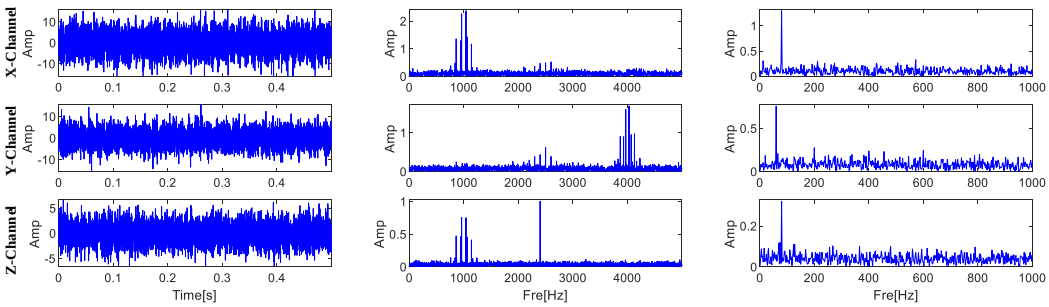

(a) Signals of three channels (b) Spectra of three signals (c) Envelope spectra of three signals

Fig.5.4 Waveform, Fourier spectrum and envelope spectrum of the three-channel signal

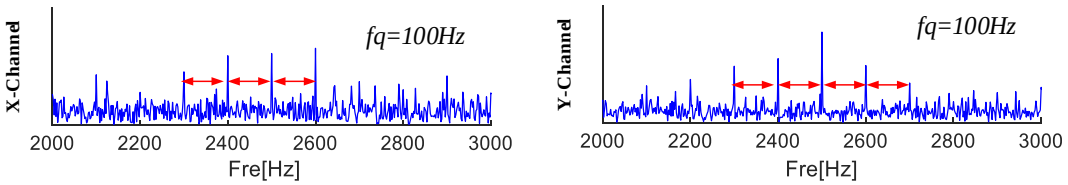

Fig.5.5 Spectra of X-Channel and Y-Channel

Fig.5.6 shows the boundary distribution obtained after EWT processes the spectra of the three channels separately. It can be found that EWT has obtained a large number of tight boundaries. In the frequency band [2000Hz-3000Hz], EWT cuts X-Channel into 7 parts and Y-Channel into 5 parts. If the fault information contained in each frequency band is too little, the harmonic information of the characteristic frequency cannot appear in the envelope spectrum, which is contrary to expectations. In Fig.5.6, the orange border is the situation where the mentioned frequency band is divided.

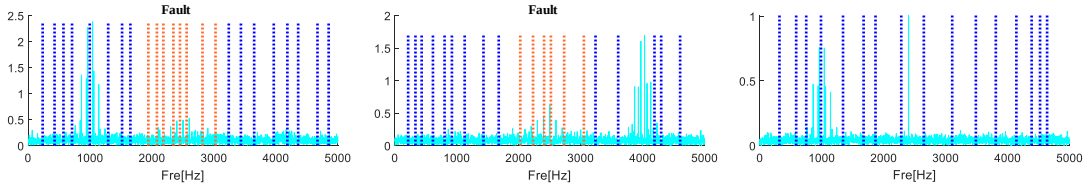

(a) Boundaries decomposed by EWT of X-Channel (b) Boundaries decomposed by EWT of Y-Channel (c) Boundaries decomposed by EWT of Z-Channel

Fig.5.6 Boundary distribution obtained by EWT processing multi-channel signals.

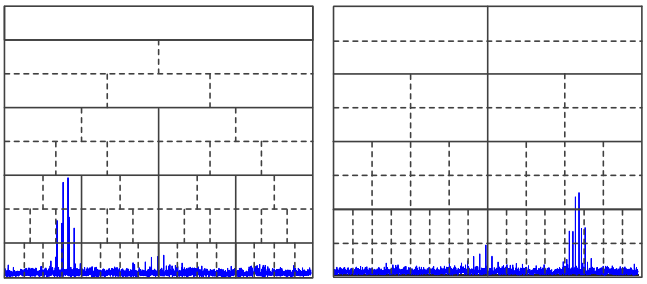

(a) FIR based Fast Kurtogram (b) STFT based Fast Kurtogram

Fig.5.7 Fast Kurtogram segmentation frame

Fig.5.7 shows the specific segmentation method. It can be found that when the number of decomposition level increases, the number of boundaries increases exponentially. The fault frequency band is easily divided into several frequency bands. In addition, this segmentation framework is fixed and cannot be adaptively matched to the specific fluctuations of the spectrum. In this example, the center frequency of the fault information is 2500 Hz, which is exactly the same as the center line of the FK segmentation frame. The above situation means that the fault information will inevitably be divided into several parts.

Different from EWT or Fast Kurtogram, the QAMD proposed in this chapter can obtain a trend spectrum similar to the fluctuation trend of quaternion Fourier spectrum. Fig.5.8a shows the correspondence between the trend spectrum obtained by QAMD and quaternion Fourier spectrum. The fluctuation of the trend spectrum is smoother and has fewer extreme points. The boundary distribution is shown in Fig.5.8b. The signal is divided into 8 parts in total. The frequency band [2000Hz-3000Hz] is hardly cut. Although some noise is contained, at least 6 pulses are retained. The waveform information of each frequency band is reconstructed and their kurtosis is calculated. The result is shown in Fig.5.8b. Extract the component corresponding to the largest kurtosis and shown its waveform, Fourier spectrum, and envelope spectrum in Fig.5.8c. Pulses appear in the waveform, indicating that there is an abnormality in

the signal. The quaternion Fourier spectrum is concentrated in the selected frequency band, with less energy leakage. The fault characteristic frequency and its harmonics appear in the envelope spectrum.

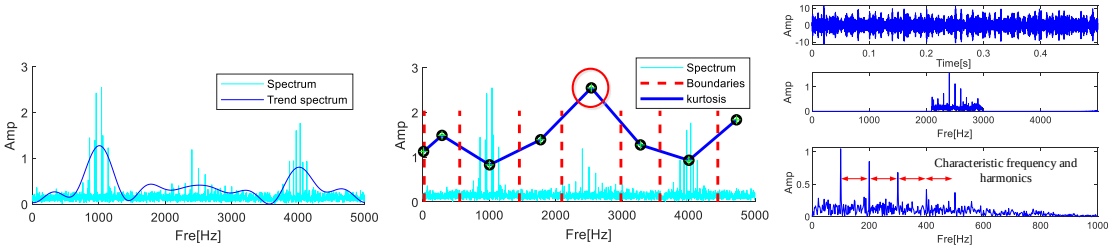

(a) Trend spectrum obtained by QAMD (b) Boundaries and kurtosis decomposed by QAMD (c) Component and its envelope spectrum

Fig.5.8 The results processed by QAMD

In order to quantify the effectiveness of the boundary distribution, Fig.5.9 shows the number of boundaries obtained by EWT processing three signals, FK fourth level and QAMD. QAMD has the least boundaries and the highest efficiency.

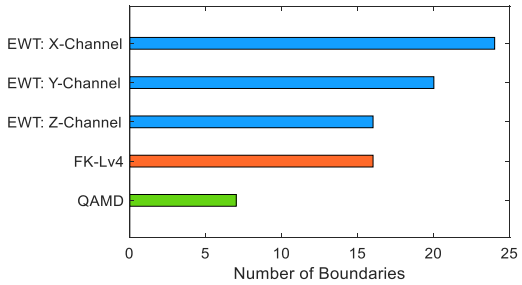

Fig.5.9 The number of boundaries obtained by five methods.

The total number of boundaries usually affects the running speed of the algorithm, and the number and position of the effective boundaries are the most important factors affecting the decomposition results. The fault information exists around 2500Hz, and the sideband is 100Hz. This section sets [2000Hz-3000Hz] as the best extraction frequency band. Among them, there can be 8 side frequency impacts under ideal conditions. Table 4 shows the number of boundaries and effective impacts included in this frequency band. QAMD has the least number of boundaries and the most effective impacts.

Table 4 The number of boundaries and effective impacts included in the frequency band [2kHz-3kHz]

Number	EWT X-Channel	EWT Y-Channel	EWT Z-Channel	FK Lv4	QAMD
Total Boundaries	6	5	2	3	2
Effective impact	1	1	1	0	6

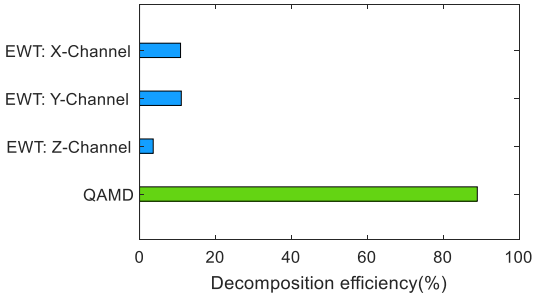

Fig.5.10 Decomposition efficiency of EWT and QAMD

In addition, the number of boundaries in this frequency band is not the only criterion for measuring efficiency. The ratio of the frequency range spanning the boundary around 2500 Hz to the entire frequency band is the most important factor for verifying the extraction efficiency. Fig.5.6 and Fig.5.8 show the number and position of the boundaries. In order to quantify the efficiency, Fig.5.10 is drawn. The decomposition efficiency of the three results obtained by EWT is less than 20%, and the QAMD reaches 89%. The above situation shows that QAMD can fuse the signal and extract the fault information, and its segmentation method is better than EWT and Fast Kurtogram.

5.3.2 Bearing fault signal verification

The acoustic signal experimental data used in this section comes from Mie University. The bearing fault simulator is shown in Fig.3.21. The drive end and the bearing part are connected with a pulley. The part where the bearing is installed is very heavy and also bears a load of about 500 kg. The rotation speed of the shaft is 70 rpm. At the same time, this experiment uses rusty chains to add noise to the system. During the experiment, the vibration acceleration sensor, acoustic emission sensor, and Microphone collected signals synchronously. This article uses the experimental field signal collected by Microphone. The sampling frequency of Microphone is 96 kHz, the acquisition time is about 20 s, and the number of acquisitions is 3. The interval between each collection is 1 minute to ensure that the environmental noise is different from the previous one.

5.3.2.1 Analysis of bearing inner ring fault data

In this experiment, a rolling bearing model NTN NU312 was used. The diameter of the inner ring is 60mm, the diameter of the outer ring is 130mm, the width is 31mm, and the number of rollers is 12. The outer ring of the bearing has been manually processed with linear damage with a width of 2.0mm and a depth of 0.3mm. The specific details are shown in Fig.5.11.

(a) Healthy Bearing (b) Faulty Bearing

Fig.5.11 Healthy bearing and faulty bearing

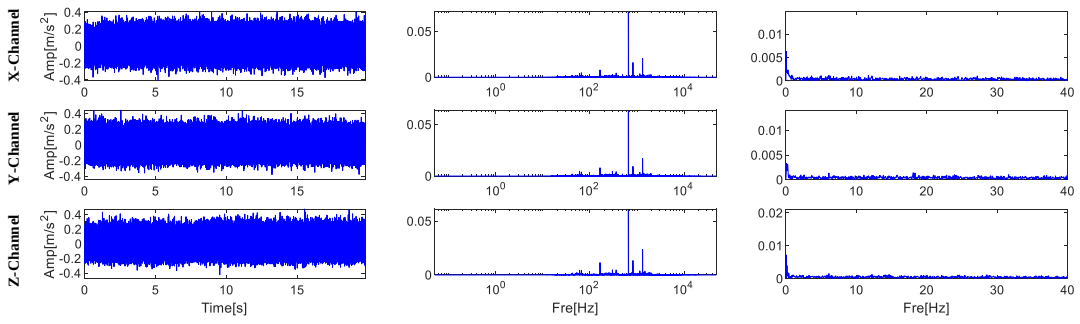

(a) Signals of three channels (b) Spectra of three signals (c) Envelope spectra of three signals

Fig.5.12 Waveform, Fourier spectrum and envelope spectrum of bearing outer fault data

In this section, three sets of acoustic signals collected by the microphone are treated as three channels. Waveforms, Fourier spectra and envelope spectra of three channel signals are shown in Fig.5.12. Since the acoustic signal is characterized by low sensitivity and strong noise, it is difficult to find periodic pulses in the waveform of Fig.5.12a. In addition, due to the low speed, it is also difficult to find fault information within 20s. After studying the Fourier spectrum, it can be found that the information with higher amplitude exists in the frequency band below 10 kHz. The amplitude of the high frequency band is low. After calculating the envelope spectrum of the signals, it is impossible to observe the characteristic frequency or harmonics of the outer ring fault. It is difficult to diagnose faults in this group of signals by means of direct analysis.

First, Fast Kurtogram is used to process the data of the three channels. Since the Fast Kurtogram of three sets of data are similar, Fig.5.13a only shows one of them. The component with the greatest kurtosis is located in the 15th frequency band of level 5, with a center frequency of 21750 Hz and a bandwidth of 1500 Hz. Ideally, this frequency band may contain at least 14 sets of sideband frequency pulse information, thereby generating fault characteristic frequencies and harmonics in the envelope spectrum. Fig.5.13b-d shows the reconstructed components of this frequency band and their envelope spectra of the three channels. There is an obvious single pulse in the waveform, but there is no period information. In the envelope spectrum, only the Z-Channel has the outer ring fault characteristic frequency, but there are no harmonics.

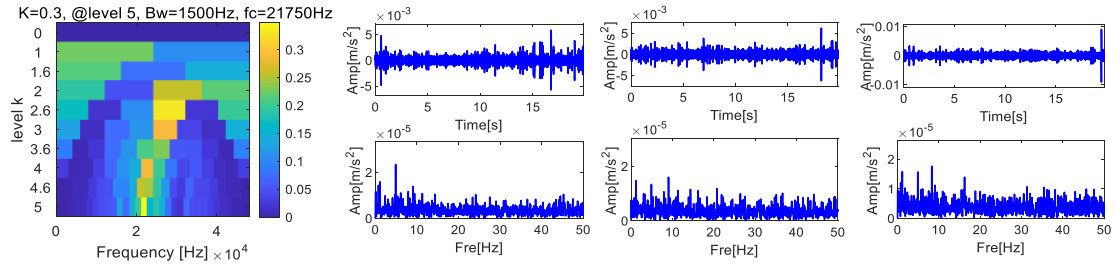

(a) Fast Kurtogram (b) EWT: X-Channel (c) EWT: Y-Channel (d) EWT: Z-Channel

Fig.5.13 Results decomposed by Fast Kurtogram

Traditional AMD needs to manually set important frequencies representing useful information and obtain bisecting frequencies after calculation to distinguish different components. In this section, the important frequencies are obtained by observation based on the amplitude in the Fourier spectrum. It can be found from Fig.5.12b that the spectra of the three channels are similar, and the amplitude information exists within 10 kHz. The important frequencies of the three signals can be found in Table 5.

Table 5 Important frequencies of AMD

Channel	Important frequencies (Hz)		
X	653.912	817.415	1307.870
Y	653.760	817.112	1307.520
Z	653.608	816.960	1307.170

Since the signals of the three channels are similar, the important frequencies obtained by observation are also almost equal. After calculation, the boundaries of three channels are almost equal: [327Hz, 736Hz, 1062Hz] This is shown in Fig.5.14 with the abscissa enlarged to within 5 kHz.

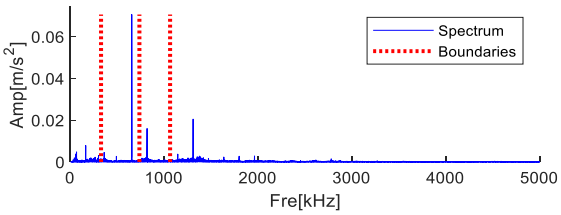

Fig.5.14 Bisecting frequencies obtained by AMD

After extracting each component of the three channels, the envelope spectrum of each component is calculated, and the result is shown in Fig.5.15. Each channel obtains four components, and there is no obvious fault characteristic frequency or harmonic in the envelope spectrum. The way of distinguishing modes based on observation is not the mainstream of signal decomposition. This low-efficiency and low-success rate approach requires finding new alternatives.

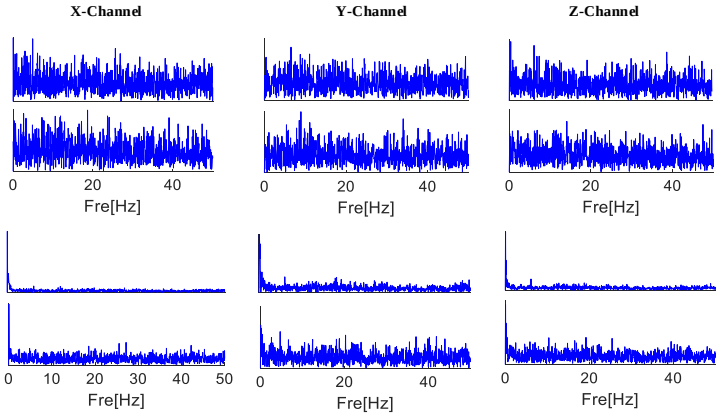

Fig.5.15 Envelope spectrum of each component decomposed by AMD

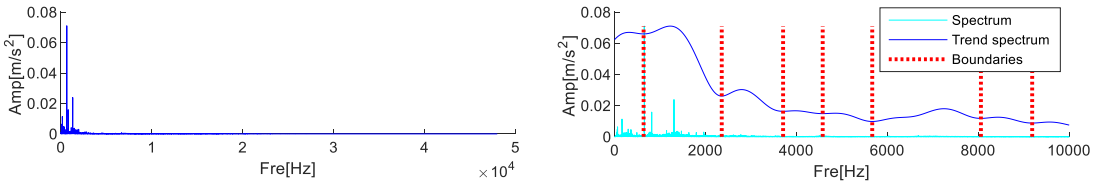

(a) Quaternion Fourier spectrum (b) Trend spectrum and boundaries obtained by QAMD

Fig.5.16 Quaternion-based fusion method and spectrum segmentation results

The QAMD designed in this paper can optimize AMD's modal selection process. QAMD first integrated the three-channel signal into a quaternion. The signal fusion method based on quaternion Fourier transform can gather useful information together on the one hand, and can provide more consistent objects for spectrum segmentation on the other hand. The Fourier spectrum of the quaternion is shown in Fig.5.16. Due to the high sampling frequency, there is a large gap between the amplitude of the high frequency part and the low frequency part of the quaternion Fourier spectrum. The high-amplitude frequency components are concentrated within 10 kHz. The spectrum segmentation method proposed in this paper is used to process the signal. The part whose frequency is lower than 10 kHz is divided into 8 parts, which can be found in Fig.5.16b.

Extract the information in each frequency band, which will be reconstructed into a time-domain waveform (Fig.5.17a). A lot of noise still exists in the components, and periodic pulses are difficult to identify from the waveform. The envelope spectrum of each component is shown in Fig.5.17b, where the characteristic frequency of the bearing outer ring fault and its harmonics

appear. The amplitude of the harmonics shows a decreasing trend. These results indicate that there is a bearing outer ring fault in the collected signals, and the proposed method can effectively extract the fault information in the acoustic signal.

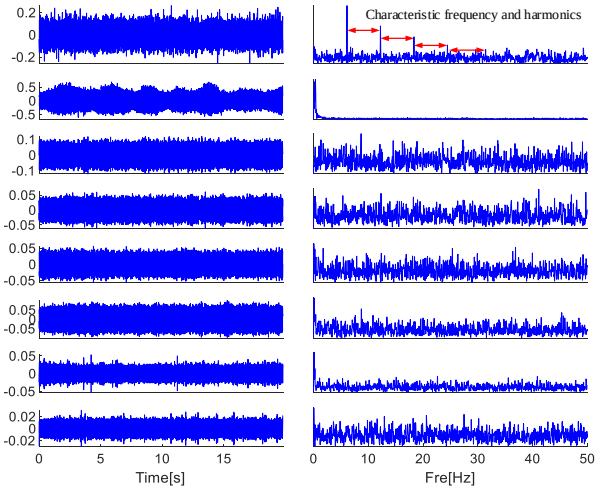

(a) Waveforms of components (b) Envelope spectra

Fig.5.17 Results decomposed by QAMD

5.3.2.2 Analysis of bearing inner ring fault data

The faulty inner ring bearing used in this experiment was manually processed with linear damage with a width of 5.0mm and a depth of 0.3mm. The specific details of the inner ring of the bearing are shown in Fig.5.18.

Fig.5.18 Inner ring faulty bearing

Fig.5.19a shows the waveform of the signal collected three times, and several periodic pulses appear. After measurement, the period is about 0.85s and the frequency is about 1.176 Hz, which is different from the characteristic frequency of the inner ring fault. The shape of the spectrum is similar to that of the outer ring, and information with large amplitudes is concentrated within 10 kHz. There are no obvious fault characteristic frequencies or harmonics in the envelope spectrum.

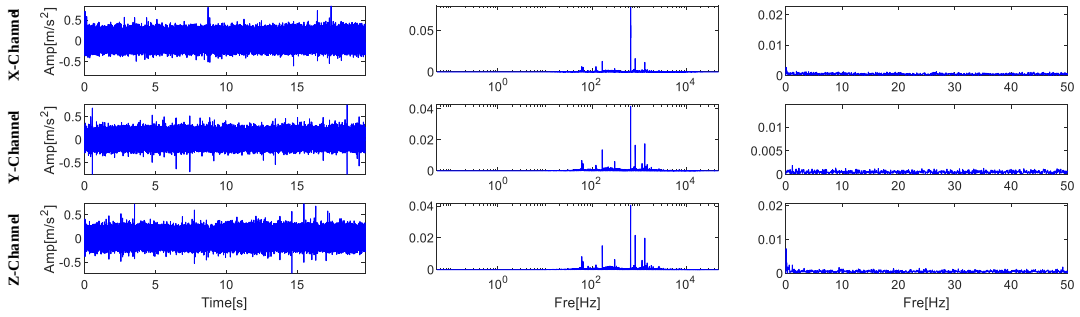

(a) Signals of three channels (b) Spectra of three signals (c) Envelope spectra of three signals

Fig.5.19 Waveform, Fourier spectrum and envelope spectrum of bearing inner fault data

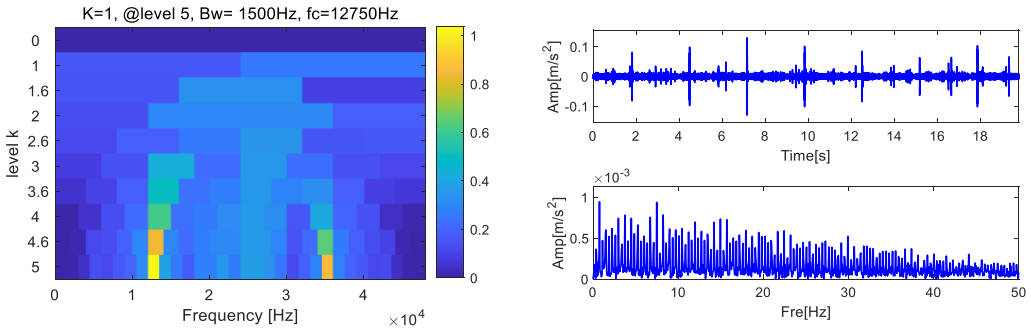

(a) Fast Kurtogram (b) Component and envelope spectrum by EWT of X-Channel

Fig.5.20 Results decomposed by Fast Kurtogram of X-Channel

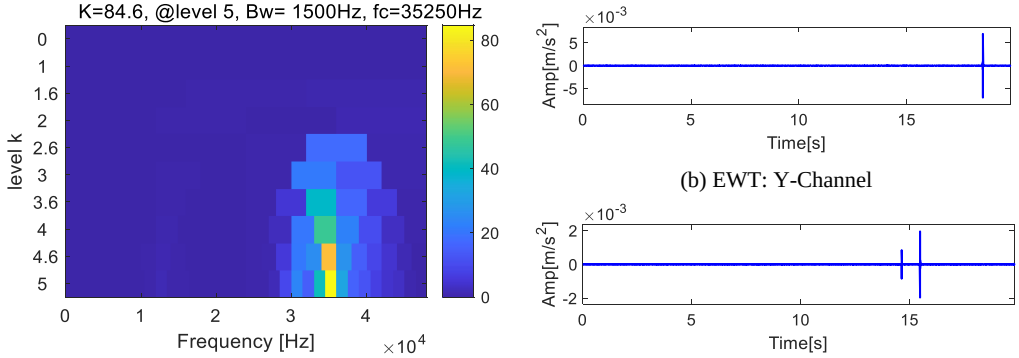

(a) Fast Kurtogram

(b) EWT: Y-Channel

(c) EWT: Z-Channel

Fig.5.21 Results decomposed by Fast Kurtogram of Y or Z-Channel

The result of Fast Kurtogram processing X-Channel is shown in Fig.5.20a. The greatest kurtosis occurred in the frequency band with a center frequency of 12750 Hz should be extracted and calculated its envelope spectrum. There are periodic pulses in the waveform of Fig.5.20b, with a period of 2.671 s and a characteristic frequency of 0.374 Hz, which has nothing to do with the inner ring fault. The results obtained by Fast Kurtogram processing Y-Channel and Z-Channel are similar, and only one of them is shown in Fig.5.21a. The component with the greatest kurtosis is located in the 24th band of level 5, with a center frequency of 35250 Hz and a bandwidth of 1500 Hz. At the same time, this frequency band in Fig.5.20a also has larger kurtosis. Fig.5.20b-c shows the reconstructed components of the frequency band of the two channels. There are obvious pulses in both waveforms, but there is no period information.

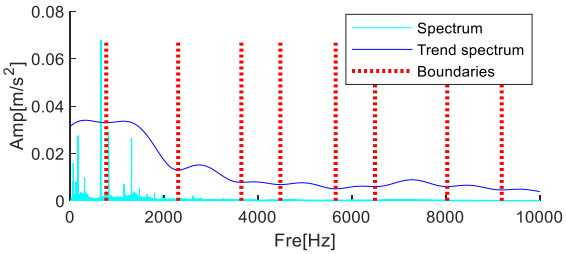

Fig.5.22 Trend spectrum and boundaries obtained by QAMD

The QAMD designed in this paper is used to process the signal. Similar to Section 4.1, this section only shows frequency bands within 10 kHz. The high-amplitude frequency components are concentrated within 10 kHz. The spectrum segmentation method proposed in this paper is used to process the signal. The part whose frequency is lower than 10 kHz is divided into 9 parts, which can be found in Fig.5.22.

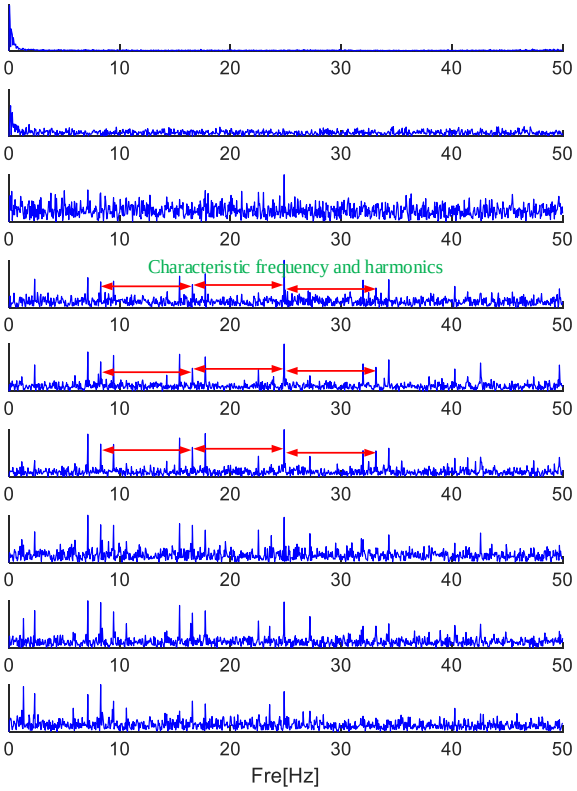

Fig.5.23 Results decomposed by QAMD

Extracting the information in each frequency band, several time-domain waveforms are reconstructed and their envelope spectra are shown in Fig.5.23. The characteristic frequency of the bearing inner ring fault and its harmonics appear in the envelope spectra of components 4-8. The results show that there is a fault in the bearing inner ring in the collected signals, and the proposed method can effectively extract the fault information in the acoustic signal.

5.4 Conclusion

This chapter proposed a new quaternion analytical mode decomposition (QAMD) method to process multiple acoustic signals and identify the fault information hidden in it. The proposed quaternion-based multiple signal fusion method can make AMD suitable for simultaneous processing of several sets of long acoustic signals. After the multi-channel acoustic signal is constructed as a quaternion signal, the fault information will be gathered and enhanced. The proposed quaternion Fourier spectrum trend segmentation method can automatically obtain bisecting frequencies and divide the signal into several frequency bands, and realize the fusion and modal decomposition of multiple sets of acoustic signals in the frequency domain. The simulation signal verifies that QAMD can capture more sideband frequency shocks representing fault information while obtaining fewer boundaries, and has the highest decomposition efficiency. Experimental results show that the proposed method can effectively extract useful information from acoustic signals and apply it to bearing fault diagnosis.

Chapter 6
Conclusions and Further Work

6.1 Conclusions

This paper introduces several optimization methods based on analytic mode decomposition, frequency slice wavelet transform, empirical wavelet transform and quaternion and their application in bearing fault diagnosis under high-speed dynamic load, low-speed heavy load and other working conditions. Finally, the conclusions of this paper can be summarized as follows:

(1) A novel framework of multi-level spectral segmentation (Ailinggram) were proposed. Ailinggram relies on OSF's window width variability and envelope estimation characteristics to achieve multi-level spectral segmentation, which replaces the manual selection of bisecting frequency and provides adaptability for AMD. The new framework increases the diversity of the center frequency and bandwidth, and suppresses the noise and interference in the reconstructed component. In order to filter the feature from the analytical modes of each level, this chapter proposes harmonic correlation index (HCI) for feature recognition and improves the usability of Ailinggram in the field of non-stationary signal processing and mechanical equipment fault diagnosis. The simulated and experimental signal proved that the proposed method is effective and can successfully extract the bearing faults. Compared with Kurtogram, Ailinggram is more practical for rotating machinery. Experiments proved that when the frequency band with the largest HCI is extracted, the probability of fault information in the envelope spectrum is greater than that of spectral kurtosis.

(2) A new Fast Entrogram method for segmenting the spectrum and extracting periodic pulse information from the frequency domain was proposed in this chapter. Fast Entrogram obtains different trend spectrum and boundary positions by changing the number of reconstructed points. Then, the frequency slice wavelet transform with better filtering effect than the FIR filter and WPT was used to extract the components in each frequency band. In order to filter fault information from the components, a novel indicator named correlation spectral negentropy that could suppress random pulse and noise and could amplify periodic information was proposed. The research proves that the proposed method not only increases the adaptability of the frequency slice wavelet transform, but also optimizes and improves the boundary segmentation method, component filtering effect and feature screening indicator of Fast Kurtogram. The simulation signal verifies that the proposed correlation spectral negentropy is sensitive to periodic pulses and is not sensitive to random pulse. The experimental signal also proves that Fast Entrogram can be effectively applied to the fault diagnosis of the inner and outer rings of rolling bearings.

(3) The method based on variable spectral segmentation empirical wavelet transform (VEWT) uses the extreme points of Multi-taper PSD to simplifies the Fourier spectrum and reduces the number of extreme points. The bandwidth obtained by the expansion algorithm designed on the basis of LMF contains less noise. VEWT is more advantageous for the decomposition of signals containing noise. At last, the MIT-BIH Arrhythmia Database is used to verify that VEWT is effective.

(4) The adaptive and concise empirical wavelet transform (ACEWT) that used to reduces the original method's excessive dependence on extreme points was proposed. Simulated signals verified that the proposed method can extract different components in complex signals. The

proposed weight unbiased autocorrelation was significantly better than other indicators in a strong noise environment, and the resistance to random pulses in noise was greatly increased. So it is more sensitive to periodic pulses that represent faults in rotating machinery. In order to expand the application of ACEWT, W-Autogram is proposed. The impact of narrow bandwidth bands on indicators was reduced. The fault data of bearing inner and outer rings verified the effectiveness of the proposed method.

(5) Harmonic spectral kurtosis (HSK) with strong anti-noise ability and anti-single pulse interference to detect periodic pulses was proposed. HSK can accurately extract the harmonic information in the envelope spectrum, quantify the periodic pulses, and suppress the influence of interference such as random pulses. Harmogram with HSK not only optimizes the spectral segmentation method, but also obtains a better center frequency and bandwidth. The filtered frequency band can contain more periodic pulse information. The proposed method has greater advantages in decomposing signals containing noise. The simulation signal shows that the proposed method is accurate and effective. The data of bearing inner ring, outer ring and compound faults prove that the method can be applied to bearing fault diagnosis.

(6) Quaternion analytical mode decomposition (QAMD) was proposed to process multiple acoustic signals and identify the fault information hidden in it. Quaternion-based multiple signal fusion method can make AMD suitable for simultaneous processing of several sets of long acoustic signals. After the multi-channel acoustic signal is constructed as a quaternion signal, the fault information will be gathered and enhanced. Quaternion Fourier spectrum trend segmentation method can automatically obtain bisecting frequencies and divide the signal into several frequency bands, and realize the fusion and modal decomposition of multiple sets of acoustic signals in the frequency domain. The simulation signal verifies that QAMD can capture more sideband frequency shocks representing fault information while obtaining fewer boundaries, and has the highest decomposition efficiency. Experimental results show that the proposed method can effectively extract useful information from acoustic signals and apply it to bearing fault diagnosis.

Through the optimization of the single-level spectral segmentation method, this paper attempts multi-level spectral segmentation in each chapter and successfully constructs the corresponding tower-shaped boundary distribution diagram, showing the upgrade process and application value of the fixed frame to the dynamic frame.

6.2 The Future Work

Based on the characteristics of quaternions, we look forward to conducting in-depth research on this basis:

(1) Analysis and diagnosis based on current characteristics can not only avoid many inconveniences of the sensor, but also avoid the influence of environmental noise on the measurement results. Applying the three phases of the current to the imaginary part of the quaternion may enhance weak fault signatures.

(2) Although the multi-level spectral segmentation method brings more possible results to the diagnosis process, it increases the time-consuming. Therefore, it is necessary to design the initial and termination conditions of the framework in terms of sampling frequency or computational bandwidth.

References

[1] A. Rai, S.H. Upadhyay, A review on signal processing techniques utilized in the fault diagnosis of rolling element bearings, Tribology International, 2016, 96: 289-306.

[2] H. Hasheminasab, S. H. Zolfani, M. Kharrazi, D. Streimikiene, Combination of sustainability and circular economy to develop a cleaner building industry, Energy and Buildings, 2022, 258: 111838.

[3] G. Beier, M. Matthess, T. Guan, D. I. de O. P. Grudzien, Impact of Industry 4.0 on corporate environmental sustainability: Comparing practitioners' perceptions from China, Brazil and Germany, Sustainable Production and Consumption, 2022, 31: 287-300.

[4] P. Toktaş-Palut, Analyzing the effects of Industry 4.0 technologies and coordination on the sustainability of supply chains, Sustainable Production and Consumption, 2022, 30: 341-358.

[5] S. Jayashree, M. N. H. Reza, C. A. N. Malarvizhi, A. Gunasekaran, Md Abdur Rauf, Testing an adoption model for Industry 4.0 and sustainability: A Malaysian scenario, Sustainable Production and Consumption, 2022, 31: 313-330.

[6] A. Espín-Delgado, S. Rnnberg, S. S. Letha, Diagnosis of supraharmonics-related problems based on the effects on electrical equipment, Electric Power Systems Research, 2021, 195(4): 107179.

[7] T. N. Kruglova, Intelligent Diagnosis of the Electrical Equipment Technical Condition, Procedia Engineering, 2015, 129: 219-224.

[8] S. Gad, M. Laskawski, G. Sloń, Symptom Models of Diagnostic of Motor-Car Electrical Equipment, IFAC Proceedings Volumes, 2004, 37(22): 409-414.

[9] D. Zhou, M. Chi, Pulse-coupled neural network and its optimization for segmentation of electrical faults with infrared thermography, Applied Soft Computing, 2019, 77: 252-260.

[10] I. Ahmad, L. M. Hee, A. M. Abdelrhman, S. A. Imam, M.S. Leong, Scopes, challenges and approaches of energy harvesting for wireless sensor nodes in machine condition monitoring systems: A review, Measurement, 2021, 183: 109856.

[11] J. Zhong, D. Wang, C. Li, A nonparametric health index and its statistical threshold for machine condition monitoring, Measurement, 2021, 167: 108290.

[12] F. Assad, S. Konstantinov, H. Nureldin, Maintenance and digital health control in smart manufacturing based on condition monitoring, Procedia CIRP, 2021, 97: 142-147.

[13] L. Song, H. Wang, P. Chen. Vibration-based intelligent fault diagnosis for roller bearings in low-speed rotating machinery. IEEE Trans. Instrum. Meas. 2018, 67: 1887-1899.

[14] B. Hou, D. Wang, Y. Chen, H. Wang, Z. Peng, K. Tsui, Interpretable online updated weights: Optimized square envelope spectrum for machine condition monitoring and fault diagnosis, Mechanical Systems and Signal Processing, 2022, 169: 108779.

[15] X. Yu, Z. Feng, M. Liang, Analytical vibration signal model and signature analysis in resonance region for planetary gearbox fault diagnosis, Journal of Sound and Vibration, 2021, 498: 115962.

[16] Y. Cheng, N. Zhou, W. Zhang, Application of an improved minimum entropy deconvolution method for railway rolling element bearing fault diagnosis, Journal of sound and vibration, 2018, 425: 53-69.

[17] B. Zhang, Y. Miao, J. Lin, Adaptive maximum second-order cyclostationarity blind deconvolution and its application for locomotive bearing fault diagnosis, Mechanical Systems and Signal Processing, 2021, 158: 107736.

[18] F. Xiao F, J. Lin, High-speed rail and high-tech industry evolution: Empirical evidence from China, " Transportation Research Interdisciplinary Perspectives, 2021, 10: 100358.

[19] S.K. Nithin, K. Hemanth, V. Shamanth, A review on combustion and vibration condition monitoring of IC engine, Materials Today: Proceedings, 2021, 45: 65-70.

[20] M. Li, T. Wang, F. Chu, Component matching chirplet transform via frequency-dependent chirp rate for wind turbine planetary gearbox fault diagnostics under variable speed condition, Mechanical Systems and Signal Processing, 2021, 161: 107997.

[21] D. Wang, Y. Chen, C. Shen, J. Zhong, Z. Peng, C. Li, Fully interpretable neural network for locating resonance frequency bands for machine condition monitoring, Mechanical Systems and Signal Processing, 2022, 168: 108673.

[22] J. Zapoměl, P. Ferfecki, A new concept of a hydrodynamic bearing lubricated by composite magnetic fluid for controlling the bearing load capacity, Mechanical Systems and Signal Processing, 2022, 168: 108678.

[23] D. Wang, K. Tsui, Theoretical investigation of the upper and lower bounds of a generalized dimensionless bearing health indicator, Mechanical systems and signal processing, 2018, 98: 890-901.

[24] L. Cui, J. Huang, F. Zhang. Quantitative and localization diagnosis of a defective ball bearing based on vertical-horizontal synchronization signal analysis, IEEE Trans. Ind. Electron., 2017, 64(11): 8695-8705.

[25] C. Peeters, J. Antoni, J. Helsen, Blind filters based on envelope spectrum sparsity indicators for

bearing and gear vibration-based condition monitoring, Mechanical Systems and Signal Processing, 2020, 138: 106556.
[26] S.R. Qin, Y.M. Zhong. Research on the unified mathematical model for FT, STFT and WT and its applications. Mechanical Systems and Signal Processing, 2004, 18: 1335-1347.
[27] W. Zeng, H. Wang. Guiyun Tian, Application of laser ultrasound imaging technology in the frequency domain based on Wigner-Ville algorithm for detecting defect. Optics & Laser Technology, 2015, 74: 72-78.
[28] R. Yan, R. Gao, X. Chen. Wavelets for fault diagnosis of rotary machines: A review with applications. Signal Processing, 2014, 96: 1-15.
[29] N. Huang, Z. Shen, S. Long. The empirical mode decomposition and the Hilbert spectrum for nonlinear and nonstationary time series analysis. Proc. Roy. Soc. London, Ser. A., 1998, 454: 903-995.
[30] H. Tang, Z. Liao, P. Chen, A Robust Deep Learning Network for Low-speed Machinery Fault Diagnosis based on Multi-kernel and RPCA, IEEE-ASME Trans. Mech., DOI: 10.1109/TMECH.2021.3084956.
[31] H. Li, Y. Hu, F. Li. Succinct and fast empirical mode decomposition., Mechanical Systems and Signal Processing, 2017, 85: 879-895.
[32] G. Chen, and Z. Wang, A signal decomposition theorem with Hilbert transform and its application to narrowband time series with closely spaced frequency components, Mechanical Systems and Signal Processing, 2012, 28: 258-279.
[33] K. Zhang, Y. Xu, and P. Chen, "Feature extraction by enhanced analytical mode decomposition based on order statistics filter," Measurement, vol. 173, no.15, pp. 108620, Mar. 2021.
[34] K. Zhang, H. Tang, P. Chen, Y. Xu, A. Hu, A method for extracting fault features using variable multi-level spectral segmentation framework and harmonic correlation index, IEEE Transactions on Instrumentation and Measurement, 2022, 71: 3505109
[35] Z. Wang, W. Ren, and J. Liu, A synchrosqueezed wavelet transform enhanced by extended analytical mode decomposition method for dynamic signal reconstruction, J. Sound Vib., 2013, 332(22): 6016-6028.
[36] H. Qu, T. Li, and G. Chen, Multiple analytical mode decompositions (M-AMD) for high accuracy parameter identification of nonlinear oscillators from free vibration, Mech. Syst. Sig. Pr., 2019, 117(15): 483-497.
[37] X. Wu, M. Tian, and Y. Zhu, A time frequency domain digital implementation of flickermeter using analytical mode decomposition," International Transactions on Electrical Energy Systems, 2019, DOI: 10.1002/2050-7038.12016.
[38] Z. Wang, B. Ge, W. Ren, and J. Hou, Discrete analytical mode decomposition with automatic bisecting frequency selection for structural dynamic response analysis and modal identification, J. Sound Vib., 2020, 484: 115520.
[39] J. Gilles, Empirical wavelet transform, IEEE Trans. Signal Process., 2013, 61: 3999-4010.
[40] K. Zhang, L. Shi, Y. Hu, P. Chen, Y. Xu, Variable spectral segmentation empirical wavelet transform for noisy signal processing, Digital Signal Processing, 2021, 117: 103151.
[41] K. Zhang, C. Ma, Y. Xu, P. Chen, J. Du, Feature extraction method based on adaptive and concise empirical wavelet transform and its applications in bearing fault diagnosis, Measurement, 2021, 172: 108976.
[42] K. Zhang, P. Chen, M. Yang, L. Song, Y. Xu, The Harmogram: A periodic impulses detection method and its application in bearing fault diagnosis, Mechanical Systems and Signal Processing, 2022, 165: 108374.
[43] B. Premjith, M. Neethu, P. Prabaharan, K. Soman, Audio data Authentication with PMU data and EWT, Procedia Technology, 2015, 21: 596-603.
[44] Y. Jiang, H. Zhu, Z. Li, A new compound faults detection method for rolling bearings based on empirical wavelet transform and chaotic oscillator, Chaos Solitons Fractals, 2016, 89: 8-19.
[45] Maya P., S. Vidyashree, Roopasree K., K.P.Somanc, Discrimination of internal fault current and inrush current in a power transformer using empirical wavelet transform, Procedia Technology, 2015, 21: 514-519.
[46] W. Chen, H. Song, Automatic noise attenuation based on clustering and empirical wavelet transform, Journal of Applied Geophysics, 2018, 159: 649-665.
[47] T. Prabhakar, P.Geetha, Two-dimensional empirical wavelet transform based supervised hyperspectral image classification, ISPRS Journal of Photogrammetry and Remote Sensing, 2017, 133: 37-45.
[48] T. Liu, J. Li, X. Cai, S. Yan, A time-frequency analysis algorithm for ultrasonic waves generating from a debonding defect by using empirical wavelet transform, Applied Acoustics, 2018, 131: 16-27.
[49] J. Chen, J. Pan, Z. Li, Generator bearing fault diagnosis for wind turbine via empirical wavelet transform using measured vibration signals, Renew. Energy, 2015, 89: 80-92.

[50] W. Deng, S. Zhang, H. Zhao, X. Yang, A novel fault diagnosis method based on integrating empirical wavelet transform and fuzzy entropy for motor bearing, IEEE Access, 2018, 6: 35042-35056.
[51] Y. Hu, X. Tu, F. Li, An adaptive and tacholess order analysis method based on enhanced empirical wavelet transform for fault detection of bearings with varying speeds, J. Sound Vib., 2017, 409: 241-255.
[52] D. Wang, Y. Zhao, C. Yi, Sparsity guided empirical wavelet transform for fault diagnosis of rolling element bearings, Mech. Syst. Sig. Process., 2017, 101: 292-308.
[53] M. Kedadouche, M.Thomas, A. Tahan, A comparative study between empirical wavelet transforms and empirical mode decomposition methods: Application to bearing defect diagnosis, Mech. Syst. Sig. Process., 2016, 81: 88–107.
[54] Y. Xu, K. Zhang, C. Ma, Z. Sheng, H. Shen. An Adaptive spectrum segmentation method to optimize empirical wavelet transform for rolling bearings fault diagnosis, IEEE Access, 2019, 7: 30437-30456.
[55] J. Gilles, K. Heal, A parameterless scale-space approach to find meaningful modes in histograms - Application to image and spectrum segmentation, Int. J. Wavelets Multire solution Inf. Process., 2014, 12(6): 1-17.
[56] Y. Song, S. Zeng, J. Ma, A fault diagnosis method for roller bearing based on empirical wavelet transform decomposition with adaptive empirical mode segmentation, Measurement, 2018, 117: 266-276.
[57] J. Zheng, H. Pan, S. Yang, Adaptive parameterless empirical wavelet transform based time-frequency analysis method and its application to rotor rubbing fault diagnosis, Signal Process., 2017, 130: 305-314.
[58] J. Pan, J. Chen, Y. Zi, Mono-component feature extraction for mechanical fault diagnosis using modified empirical wavelet transform via data-driven adaptive Fourier spectrum segment, Mech. Syst. Sig. Process., 2015, 72: 160-183.
[59] J. Amezquita-Sanchez, H. Adeli, A new music-empirical wavelet transform methodology for time–frequency analysis of noisy nonlinear and non-stationary signals, Digit. Signal Process, 2015, 45: 55-68.
[60] Z. Yan, A. Miyamoto, Z. W. Jiang. Frequency slice wavelet transform for transient vibration response analysis, Mech. Syst. Signal Process., 2009, 23(5): 1474-1489
[61] Z. Yan, A. Miyamoto, Z. W. Jiang. An overall theoretical description of frequency slice wavelet transform, Mech. Syst. Signal Process., 2010, 24(2): 491-507
[62] K. Zhang, Y. Xu, Z. Liao, L. Song, and P. Chen, A novel Fast Entrogram and its applications in rolling bearing fault diagnosis, Mechanical Systems and Signal Processing, 2021, 154: 107582.
[63] X. Liu, Z. W. Jiang, Z. Yan. Improvement of accuracy in damage localization using frequency slice wavelet transform, Shock & Vibration, 2015, 19(4): 585-596
[64] C. Duan, P. Gao, X. Xu, Q. Gao. A ball defect diagnosis method using time-frequency kurtosis spectrum, Journal of mechanical engineering, 2015, 51(15): 78-83
[65] T. Guo, X. Fang, Q. M. Xie, Z. H. Yan, L. Fan. Application of FSWT in accurate extraction of time-frequency features for blasting vibration signals, Journal of Vibration and Shock, 2013, 32(22)
[66] Z. Yan, A. Miyamoto, Z. W. Jiang. Frequency slice algorithm for modal signal separation and damping identification. Computers & Structures., 2011, 89(1): 14-26.
[67] R. Dwyer, Use of the kurtosis statistic in the frequency domain as an aid in detecting random signals. IEEE Journal of Oceanic Engineering, 1984, 9(2):85-92.
[68] C. Ottonello, S. Pagnan, Modified frequency domain kurtosis for signal processing, Electronics Letters, 2002, 30(14):1117-1118.
[69] G.L. McDonald, Q. Zhao, M.J. Zuo, Maximum correlated Kurtosis deconvolution and application on gear tooth chip fault detection, Mechanical Systems and Signal Processing, 2012, 33: 237-255.
[70] V. Capdevielle, C. Serviere, and J. L. Lacoume. Blind separation of wide-band sources: Application to rotating machine signals. European Signal Processing Conference. 1996. Eusipco 1996. IEEE, 2015, 1-4.
[71] P. Borghesani, P. Pennacchi, S. Chatterton, The relationship between kurtosis-and envelope-based indexes for the diagnostic of rolling element bearings, Mechanical Systems and Signal Processing, 2014, 43(1-2): 25-43.
[72] D. He, X. Wang, S. L. Identification of multiple faults in rotating machinery based on minimum entropy deconvolution combined with spectral kurtosis. Mechanical Systems & Signal Processing, 2016, 81:235-249.
[73] N. Sawalhi, R.B. Randall, H. Endo. The enhancement of fault detection and diagnosis in rolling element bearings using minimum entropy deconvolution combined with spectral kurtosis. Mechanical Systems and Signal Processing, 2007, 21(6):2616-2633.
[74] J. Chen, Y. Zi, Z. He. Improved spectral kurtosis with adaptive redundant multiwavelet packet and its applications for rotating machinery fault detection. Measurement Science and Technology,

2012, 23(4):045608.
[75] J. Xiang, Y. Zhong, H. Gao. Rolling element bearing fault detection using PPCA and spectral kurtosi. Measurement, 2015, 75:180-191.
[76] F. Cong, J. Chen, G. Dong. Spectral kurtosis based on AR model for fault diagnosis and condition monitoring of rolling bearing. Journal of Mechanical Science & Technology, 2012, 26(2): 301-306.
[77] S. Arivazhagan, M. Rosaline, Optimal Gabor sub-band-based spectral kurtosis and Teager Kaiser energy for maritime target detection in SAR images, Signal, Image and Video Processing, 2022: 1-9.
[78] T. Barszcz, R. B. Randall. Application of spectral kurtosis for detection of a tooth crack in the planetary gear of a wind turbine. Mech. Syst. Signal Process., 2009 23: 1352-1365.
[79] H. Wang, Z. Lai, D. Wu, Investigation of the friction-induced vibration of a novel four-way reversing valve using spectral kurtosis and number of peaks spectrum, Mechanical Systems and Signal Processing, 2022, 166: 108425.
[80] J. Antoni, R.B. Randall. The spectral kurtosis: application to the vibratory surveillance and diagnostics of rotating machines[J]. Mech. Syst. Signal Process., 2006, 20(2): 308-331.
[81] J. Antoni. The spectral kurtosis: a useful tool for characterising non-stationary signals[J]. Mech. Syst. Signal Process., 2006, 20(2): 282-307.
[82] J. Antoni. Fast computation of the kurtogram for the detection of transient faults[J]. Mech. Syst. Signal Process., 2007, 21(1): 108-124.
[83] T. Wang, F. Chu, Z. Feng, Meshing frequency modulation (MFM) index-based kurtogram for planet bearing fault detection, Journal of Sound and Vibration, 2018, 432: 437-453.
[84] Y. Zhang, R. B. Randall. Rolling element bearing fault diagnosis based on the combination of genetic algorithms and fast kurtogram. Mech. Syst. Signal Process., 2009, 23(5):1509-1517.
[85] Y. Wang, Z. He, Y. Zi. Enhancement of signal denoising and multiple fault signatures detecting in rotating machinery using dual-tree complex wavelet transform[J]. Mech. Syst. Signal Process., 2010, 24(1): 119-137.
[86] Tse Peter W., D. Wang. The design of a new sparsogram for fast bearing fault diagnosis: Part 1 of the two related manuscripts that have a joint title as “Two automatic vibration-based fault diagnostic methods using the novel sparsity measurement - Parts 1 and 2”. Mech. Syst. Signal Process., 2013, 40(2): 499-519.
[87] Tse Peter W., D. Wang. The automatic selection of an optimal wavelet filter and its enhancement by the new sparsogram for bearing fault detection: Part 2 of the two related manuscripts that have a joint title as “Two automatic vibration-based fault diagnostic methods using the novel sparsity measurement-Parts 1 and 2”. Mech. Syst. Signal Process., 2013, 40(2): 520-544.
[88] A. Mauricio, W.A. Smith, R.B. Randall, Improved Envelope Spectrum via Feature Optimisation-gram (IESFOgram): A novel tool for rolling element bearing diagnostics under non-stationary operating conditions, Mechanical Systems and Signal Processing, 2020, 144: 106891.
[89] J. Antoni. The infogram: Entropic evidence of the signature of repetitive transients, Mech. Syst. & Signal Process., 2016, 74: 73-94.
[90] Z. Feng, H. Ma, M. Zuo. Spectral negentropy based sidebands and demodulation analysis for planet bearing fault diagnosis. J. Sound Vib., 2017, 410(8): 124-150.
[91] T. Wang, Q. Han, F. Chu, Z. Feng. A new SKRgram based demodulation technique for planet bearing fault detection. J. Sound Vib., 2016, 385(22): 330-349.
[92] A. Moshrefzadeh, A. Fasana. The Autogram: An effective approach for selecting the optimal demodulation band in rolling element bearings diagnosis, Mech. Syst. & Signal Process., 2018, 105: 294-318.
[93] Y. Wang, M. Liang. An adaptive SK technique and its application for fault detection of rolling element bearings, Mech. Syst. & Signal Process., 2011, 25(5):1750-1764.
[94] T. Barszcz, A. Jabłoński. A novel method for the optimal band selection for vibration signal demodulation and comparison with the Kurtogram, Mech. Syst. & Signal Process., 2011, 25(1):431-451.
[95] H. Liu, W. Huang, S. Wang. Adaptive spectral kurtosis filtering based on Morlet wavelet and its application for signal transients detection, Signal Processing, 2014, 96(5):118-124.
[96] Y. Xu, W. Tian, K. Zhang. Application of an enhanced fast kurtogram based on empirical wavelet transform for bearing fault diagnosis, Meas. Sci. Technol., 2019, 30: 035001.
[97] Y. Xu, K. Zhang, C. Ma. Adaptive kurtogram and its applications in rolling bearing fault diagnosis. Mech. Syst. Signal Process., 2019, 130: 87-107.
[98] J. Feng, Lei Y, Shan H. Early fault diagnosis of bearings using an improved spectral kurtosis by maximum correlated kurtosis deconvolution[J]. Sensors, 2015, 15(11): 29363-29377.
[99] Y. Wang, H. Xiang. Spectral kurtosis for fault detection, diagnosis and prognostics of rotating machines: A review with applications[J]. Mech. Syst. & Signal Process., 2016, s 66-67:679-698.
[100] Adam Glowacz, Acoustic based fault diagnosis of three-phase induction motor, Applied Acoustics, 2018, 137: 82-89.

[101] Adam Glowacz, Zygfryd Glowacz, Diagnosis of stator faults of the single-phase induction motor using acoustic signals, Applied Acoustics, 2017, 117: 20-27.
[102] W. Lu, W. Jiang, H. Wu, J. Hou, A fault diagnosis scheme of rolling element bearing based on near-field acoustic holography and gray level co-occurrence matrix, Journal of Sound and Vibration, 2012, 331(15): 3663-3674.
[103] A. Kumar, C.P. Gandhi, Y. Zhou, R. Kumar, J. Xiang, Variational mode decomposition based symmetric single valued neutrosophic cross entropy measure for the identification of bearing defects in a centrifugal pump, Applied Acoustics, 2020, 165: 107294.
[104] Y. Zhao, J. Zhang, Q. Zhao, Online Monitoring of Low-Frequency Oscillation Based on the Improved Analytical Modal Decomposition Method, IEEE Access, 2020, 8: 215256-215266.
[105] L. Rikam, L. Bitjoka, A. Nketsa, Quaternion Fourier Transform spectral analysis of electrical currents for bearing faults detection and diagnosis, Mechanical Systems and Signal Processing, 2022, 168: 108656.
[106] R. Bendoumia, M. Djendi, Acoustic noise reduction by new two-channel proportionate forward symmetric adaptive decorrelating algorithms in sparse systems, Applied Acoustics, 2018, 137: 69-81.
[107] O. Jeon, H. Ryu, H. Kim, S. Wang, Vibration localization prediction and optimal exciter placement for improving the sound field optimization performance of multi-channel distributed mode loudspeakers, J. Sound Vib., 2020, 481: 115424.
[108] C. Eric, Hamdan, F. Fazi, A modal analysis of multichannel crosstalk cancellation systems and their relationship to amplitude panning, J. Sound Vib., 2021, 490: 115743.
[109] E. Salah, K. Amine, K. Redouane, K. Fares, A Fourier transform based audio watermarking algorithm, Applied Acoustics, 2021, 172: 107652.
[110] Paulo V.R. Martins, O. Silva, A. Lenzi, Insertion loss analysis of slender beams with periodic curvatures using quaternion-based parametrization, FE method and wave propagation approach, Applied Acoustics, 2019, 455: 82-95.
[111] C. Yi, Y. Lv, Z. Dang, H. Xiao, X. Yu, Quaternion singular spectrum analysis using convex optimization and its application to fault diagnosis of rolling bearing, Measurement, 2017, 103: 321-332.
[112] Y. Ma, J. Cheng, N. Hu, Z. Cheng, Y. Yang, Symplectic quaternion singular mode decomposition with application in gear fault diagnosis, Mechanism and Machine Theory, 2021, 160: 104266.
[113] K. Zhang, Y. Deng, P. Chen, C. Ma, Y. Xu, Quaternion empirical wavelet transform and its applications in rolling bearing fault diagnosis, Measurement, 2022, 195: 111179.
[114] C. Haley, M. Anitescu, Optimal bandwidth for multitaper spectrum estimation, IEEE Signal Processing Letters, 2017, 24(11): 1696-1700.
[115] X. Wang, J. Xiong, L. Geng, J. Zheng, S. Zhu, Parameter identification of doubly-fed induction generator by the Levenberg-Marquardt-Fletcher method, 2013 IEEE Power & Energy Society General Meeting, DOI: 10.1109/PESMG.2013.6672535.
[116] G. Moody, R. Mark, The impact of the MIT-BIH Arrhythmia Database, IEEE Eng in Med and Biol, 2001, 20(3): 45-50.
[117] A. Goldberger, L. Amaral, L. Glass, J. Hausdorff, P. Ivanov, ... & H. Stanley, PhysioBank, PhysioToolkit, and PhysioNet: Components of a new research resource for complex physiologic signals, Circulation, 2000, 101(23): e215–e220.
[118] W.R. Hamilton, II. On quaternions; or on a new system of imaginaries in algebra, Lond. Edin. Dublin Philos. Mag. J. Sci., 1844, 25(163): 10–13.
[119] F. Ortolani, D. Comminiello, M. Scarpiniti, Frequency domain quaternion adaptive filters: Algorithms and convergence performance, Signal Processing., 2017, 136: 69–80.
[120] T. Ell, N. Le Bihan, S. Sangwine, Quaternion Fourier Transforms for Signal and Image Processing, Wiley, London, UK. 2014.
[121] S.J. Sangwine, The Discrete Quaternion Fourier Transform, 1997 Sixth International Conference on Image Processing and Its Applications, 1997, 2: 790-793.
[122] T.A. Ell, S.J. Sangwine, Decomposition of 2D hypercomplex Fourier transforms into pairs of complex Fourier transforms, in: Proceedings of the 10th European Signal Processing Conference, 2000.